

**Universität
Rostock**



Traditio et Innovatio

Thermal Evolution Models for Uranus and Neptune

Dissertation

zur

Erlangung des akademischen Grades

doctor rerum naturalium (Dr. rer. nat.)

der Mathematisch-Naturwissenschaftlichen Fakultät

der Universität Rostock

vorgelegt von

Ludwig Scheibe, geb. am 04. August 1992 in Magdeburg
aus Rostock

Rostock, den 04.10.2021

eingereicht am 04.10.2021

verteidigt am 28.01.2021

1. Gutachter : Prof. Dr. R. Redmer,
Universität Rostock,
Institut für Physik

2. Gutachterin: Prof. Dr. Doris Breuer,
Deutsches Zentrum für Luft- und Raumfahrt,
Institut für Planetenforschung

Abstract

The outer planets Uranus and Neptune have long challenged the planetary science community with their highly different measured intrinsic heat fluxes. I have developed a new planetary modelling and evolution computer program in order to investigate the thermal evolution of these planets more closely. Here, I present the principles by which this code works, as well as study the influences different parameters have on Uranus' and Neptune's possible evolution. Standard adiabatic evolution calculations using state-of-the-art equation of state data are shown and the influence of different assumptions regarding the energy balance of the planet with the solar irradiation, as well as that of equation of state data, on the cooling behaviour is discussed. I confirm the previous findings of a large difference in Uranus' and Neptune's calculated cooling times using the adiabatic assumption, but find generally lower cooling times for both Uranus and Neptune. Furthermore, Uranus and Neptune evolution models under the assumption of a thermal boundary layer are shown. This boundary separates an ice- and rock-rich inner envelope and a hydrogen- and helium-rich outer envelope and traps primordial heat inside the planet for a portion of the planet's evolution. I have investigated a wide range of parameters for this thermal barrier and was able to show that this mechanism can influence the planet's evolution drastically, making it appear either fainter or brighter than the adiabatic case. Thus, the possibility of a thermal boundary layer allows for an explanation of both Uranus' and Neptune's luminosities within the same framework.

Zusammenfassung

Die beiden äußersten Planeten des Sonnensystems, Uranus und Neptun, haben die Planetenwissenschaft seit langem mit ihren hochgradig verschiedenen gemessenen intrinsischen Wärmeflüssen vor Herausforderungen gestellt. Ich habe ein neues Computerprogramm zur Berechnung von Struktur- und Evolutionsmodellen von Planeten erstellt, um die thermische Entwicklung dieser beiden Planeten näher zu untersuchen. In dieser Arbeit präsentiere ich die Prinzipien, nach denen das Programm arbeitet, und studiere die Einflüsse verschiedener Faktoren auf die mögliche Entwicklung von Uranus und Neptun. Evolutionsrechnungen mit der Standardannahme eines adiabatischen Inneren, die aktuelle Zustandsgleichungen verwenden, werden vorgestellt und der Einfluss verschiedener Annahmen bezüglich Zustandsgleichung und Energiebilanz mit der Sonne wird diskutiert. Damit bestätige ich die früheren Ergebnisse eines deutlich unterschiedlichen Abkühlungsverhaltens für Uranus und Neptun mit diesen Annahmen, aber erhalte insgesamt niedrigere Kühlzeiten für beide Planeten. Darüber hinaus werden Evolutionsmodelle für Uranus und Neptun unter der Annahme einer thermischen Grenzschicht vorgestellt. Diese Grenze trennt den eis- und gesteinsreichen inneren Mantel vom wasserstoff- und heliumreichen äußeren Mantel des Planeten und hält für einen Teil der Planetenevolution die Wärme aus dem Entstehungsprozess im Inneren fest. Ich habe eine Reihe von Parametern bezüglich dieser thermischen Barriere untersucht und konnte zeigen, dass dieser Mechanismus die Abkühlung des Planeten drastisch beeinflussen kann und diesen zum heutigen Zeitpunkt entweder heller oder dunkler als den adiabatischen Fall erscheinen lassen kann. Daher erlaubt die Annahme einer solchen thermischen Grenzschicht die Erklärung der Wärmeflüsse sowohl von Uranus als auch Neptun in einem gemeinsamen Rahmen.

Contents

1. Introduction	1
2. Fundamentals of planet modelling	7
2.1. Equations of planetary structure	7
2.2. Heat transport within planets	9
2.2.1. The luminosity equation	9
2.2.2. Radiative and conductive heat transport	13
2.2.3. Convective energy transport	15
2.3. Summary of basic equations	20
3. Numerical procedure	21
3.1. Boundary Conditions	21
3.2. The Henyey method	23
3.3. The OTTER Code	27
3.4. Benchmarking the evolution calculations	30
3.4.1. Convergence with respect to time steps and mass points	30
3.4.2. Comparison with an established code	31
4. Materials and their properties in planetary modeling	33
4.1. The composition of Uranus and Neptune	33
4.2. Equations of state	35
4.2.1. Hydrogen and helium	36
4.2.2. Heavy elements	38
4.2.3. Linear mixing	39
4.3. Thermal conductivity	40
5. Adiabatic evolution of Uranus and Neptune	43
5.1. Parameters and model assumptions	44
5.2. Influence of solar irradiation	45

5.3. Influence of different equations of state	46
5.4. Discussion of adiabatic models	50
6. Ice giant evolution in the presence of a deep internal thermal boundary layer	53
6.1. Model assumptions	54
6.2. TBL stability considerations	57
6.3. Influence of a conductive interface on the cooling behaviour	59
6.4. Parameters influencing the TBL cooling behaviour	62
6.4.1. TBL thickness	62
6.4.2. Thermal conductivity	64
6.4.3. TBL onset time	66
6.5. Range of present-day effective temperatures	69
6.6. Interior Profiles	71
6.7. Discussion of TBL models	75
7. Summary and outlook	79
A. Parameters and Observables	83
B. Derivations & Proofs	87
B.1. Approximating the effect of rotation in spherical symmetry	87
B.2. Formulating δq in Terms of T and P	88
B.3. The adiabatic temperature gradient	91
B.4. Calculating the composition gradient ∇_X	93
C. Functions and derivatives for the H-matrix	97
D. Effect of radioactive decay on the thermal evolution	105
E. Effect of rotational term on the conductive gradient	109

Chapter 1.

Introduction

Uranus and Neptune are two neighbouring planets in the outer reaches of the Solar System. Their masses of $M_U = 14.5 M_E$ and $M_N = 17.2 M_E$ (with the Earth mass $1 M_E = 5.97 \times 10^{24}$ kg) lie between those of Mercury, Venus, Earth, and Mars ($0.06 - 1 M_E$) and those of Saturn and Jupiter ($95 - 318 M_E$); the same is true for their radii. For this reason, they have been put in their own category between the rock-dominated inner planets, and the hydrogen- and helium-dominated gas giants Jupiter and Saturn, and have been dubbed “ice giants”, in reference to the supposition that they are primarily composed from so-called ice-forming volatile compounds such as water, methane, and ammonia.

In contrast to the other planets out to Saturn, which had already been observed and studied by ancient human civilisations, both Uranus and Neptune were only discovered in the modern period, as they are considerably farther from Earth and therefore appear fainter in the sky. Specifically, Uranus was discovered in 1781 by William Herschel [55], who first thought he had observed a new comet. Neptune’s existence and orbit was theoretically predicted by Urbain Le Verrier [78] as an explanation for per-

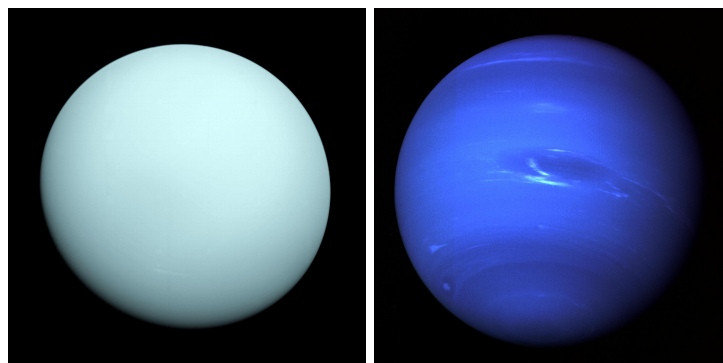


Fig. 1.1.: Images of Uranus (left) and Neptune (right), taken by the Voyager 2 probe during flyby. Image courtesy of NASA/JPL-Caltech.

turbations in Uranus' orbit, and then observed for the first time later the same year by Johann Gottfried Galle and Heinrich Louis d'Arrest [21]. Until the late 20th century, obtaining physical characteristics was limited to Earth-based observations. Then, our knowledge of empirical information about Uranus and Neptune took a leap forward when the Voyager II probe performed flybys of Uranus in 1986 and of Neptune in 1989. To date, it is the only spacecraft to have reached and explored these planets. It provided more accurate information on, among other things, shape, luminosity, Albedo, atmospheric composition, and motion of the satellites, which is important in determining the gravitational field. After Voyager had passed, further measurements were only by ground-based facilities and the Hubble Space Telescope, launched in 1990. Recently, in light of the upcoming NASA Planetary Science Decadal Survey 2023, there has been a growing renewed interest in exploring Uranus, Neptune and their satellites further with a dedicated spacecraft mission [23, 57, 123], following the highly successful missions Cassini, exploring Saturn and its satellites, and Juno, directed at Jupiter.

Uranus and Neptune feature a number of similarities beyond their mass and radius range. Both planets exhibit a strongly hydrogen- and helium-dominated atmosphere with a high carbon abundance of 85 (Uranus) and 89 (Neptune) times the solar value [50]. Furthermore, both planets' magnetic fields were measured to be highly non-dipolar and non-axial-symmetric, which is different from the other planets in the Solar System [18], and their rotation periods of ca. 17.2 h (Uranus) and 16.1 h (Neptune) are relatively close to each other. However, there are also some key differences. For example, Uranus' bulk density of 1.27 g cm^{-3} is smaller than Neptune's (1.64 g cm^{-3}) [45], suggesting that it has a smaller amount of heavy elements. Also, interior models based on the gravitational moments suggest that Uranus has its heavy-element content more concentrated to the centre. Furthermore, while Neptune's obliquity – the angle between equatorial plane and orbital plane – is relatively low with 28.3° , Uranus is heavily tilted with an obliquity of 97.8° [145]. Moreover, Neptune's atmosphere shows stronger signs of activity in form of vortices and storms than Uranus' [50]. And finally, there is the difference I will focus on in this work, which is their highly different intrinsic heat fluxes.

Already in the late 1970s, brightness measurements in the infrared spectrum revealed that Uranus' total luminosity was only slightly higher than the irradiation it received from the sun [22], while Neptune was found to radiate almost twice as much as it received [86]. Early numerical evolution models by Hubbard & MacFarlane (1980) [62] could only produce a cooling time close to the age of the Solar System if both plan-

ets started their evolution less than 20 K above their measured effective temperatures, which was considered highly unlikely. Following advances both in observations – thanks in no small part to the Voyager mission – and in equation of state data – particularly in the high-temperature, high-pressure regime – newer models were calculated. Those were still found to overestimate Uranus’ present-day luminosity, which is equivalent to saying that the models require too long to cool from a hot initial state right after the planet formation to the observed state. On the other hand, Neptune’s luminosity was usually in line with the measurements [24, 85, 105]. While this simple framing as “Neptune is consistent with standard evolution models, while Uranus is too faint to be explained” might not be entirely correct, as will be the subject of a portion of this work, the fact remains that there is this fundamental difference in the internal heat fluxes of these otherwise quite similar planets.

A number of theories to explain this behaviour have been put forth, though most of them focus on Uranus. One explanation could lie in atmospheric dynamics. Kurosaki & Ikoma (2017) [77] find that the latent heat released from condensation of initially enriched ice species H_2O , NH_3 , and CH_4 lead to an acceleration in the cooling of Uranus, bringing its cooling time in line with the observations. However, in their models, reproducing both the correct radius and luminosity would require an atmosphere more enriched in heavy elements than the underlying envelope, which they note would be hydrodynamically unstable [77]. Conversely, Leconte *et al.* (2017) [81] report that the inhibition of convection due to water condensation actually slows down cooling of the interior significantly [81]. Markham & Stevenson (2021) [92] find that the condensation of methane in the atmosphere can speed up cooling, although not to a sufficient degree to completely account for Uranus’ faintness, while the water condensation at deeper levels works in the other direction and causes a slowdown [92]. With both of these effects working against each other, this might help account for differences between the two ice giants, with the accelerating effect of methane dominating for Uranus and the decelerating effect of water dominating for Neptune.

Another theory is that there might be some mechanism in the deep interior inhibiting convection, as argued, for example, by Podolak *et al.* (1991) [112] or Hubbard *et al.* (1995) [64], most likely in the form of a gradient in the composition. Since convection is a highly effective way of transporting energy, such a stably stratified region would act as a thermal barrier, effectively trapping part of the planet’s heat inside and therefore speeding up the outside cooling. Nettelmann *et al.* (2016) [102] showed that assuming a thermal barrier in the interior, represented by a forced temperature gradient in the planet that grows with time, was sufficient to explain Uranus’ low intrinsic

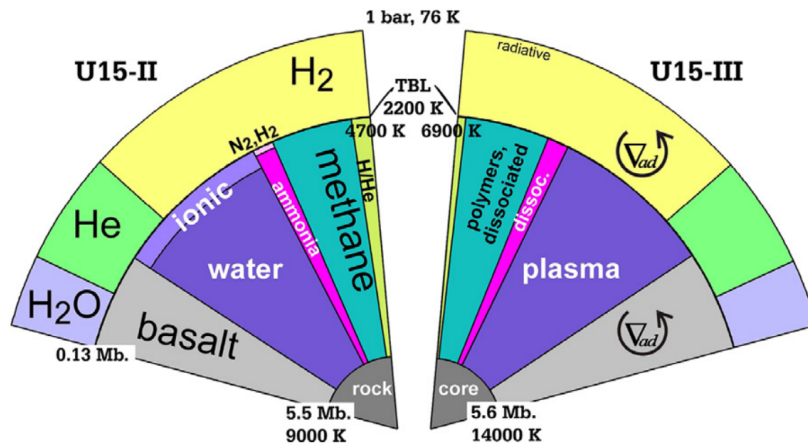


Fig. 1.2.: Illustration of the model structure employed by Nettelmann *et al.* (2016) for explaining Uranus' unusually low intrinsic luminosity. A hydrogen and helium dominated, convective outer envelope is located on top of a convective inner envelope composed of water, methane, ammonia, basalt, and small amounts of hydrogen and helium. Separating the envelopes is a thermal boundary layer (TBL) at approximately 13 GPa, that is rendered as a jump in temperature of several thousand Kelvin. Figure was taken from Ref. [102].

heat flow. An illustration of their model structure is shown in Fig. 1.2. More recently, Vazan & Helled (2020) [138] performed planetary evolution calculations based on a range of primordial composition gradients and found that such stably stratified regions could indeed survive over the planet's lifetimes and reproduce Uranus' observed luminosities. There is also the factor that an electrically conducting, non-convecting area in the planet's deep interior was found to be able to contribute to generating a magnetic field similar to those observed in Uranus and Neptune in models by Stanley & Bloxham [131, 132], although models by Soderlund *et al.* (2013) [130] have also produced similar magnetic fields using a very thick convective dynamo zone and a comparatively large solid core. There has been considerably less attention devoted to Neptune, probably because in the past, its luminosity was usually found to be in line with a convective interior. As to why the above composition gradients would affect only Uranus but not Neptune, it was argued, e.g. by Stevenson (1986) [133] or Reinhardt *et al.* (2020) [122], that this difference can be traced back to giant impact events that hit and subsequently affected the planets differently, and could also be responsible for Uranus' high axial tilt. On the other hand, Helled & Fortney (2020) [50] remind us that the similarity between Uranus and Neptune might only be superficial and not due to similar formation and interior structure at all. The question of Uranus' and Neptune's evolution is far from settled.

Constraining the thermal evolution is important because it is intimately linked to the

interior structure and to formation models. The temperature profile depends strongly on the energy transfer mechanism and therefore the evolution, and can have impact on the composition inferred from the observations [114]. The inferred composition can then serve as a constraint on planet formation models, which in turn influence valid evolution scenarios. Thus, planet evolution is an important part of planetary science, a field that has been ever-expanding since the discovery of extrasolar planets began. A large number of these have radii in the range between 2 and 4 Earth radii, and therefore are of similar size to Uranus/Neptune or intermediate between the Solar System ice giants and Earth-like rocky planets, which are often called ‘sub-Neptunes’ [38, 61, 140]. While that does not necessarily mean that they share the same composition, it does underline that Uranus and Neptune represent a type of planet that can reasonably be expected to be common in our galaxy.

Thus, in this work I want to examine Uranus’ and Neptune’s thermal evolution and their luminosity problem in detail. In Chapter 2, I will lay out the theoretical principles of planet modelling, in Chapter 3 how they are applied in the computer code developed for this research, as well as how this code is constructed. Chapter 4 deals with the constituents Uranus and Neptune are assumed to be composed of and their material properties. Then, in Chapter 5, I will re-examine adiabatic evolution calculations using modern equation of state data and gauging the effect of solar irradiation parameters. In Chapter 6, I turn to a non-adiabatic evolution model under the assumption of a conductive thermal boundary layer in the planet’s interior, building on the previously mentioned work of Nettelmann *et al.* (2016) [102]. Finally, in Chapter 7, I summarise my results and give an outlook on possible future work. The main results have already been published in References [127] and [128] and are now expanded upon here.

Certainly, further work will be needed to solve the riddle of Uranus’ and Neptune’s luminosities or to give a definitive detailed model of the highly complex interiors of the ice giants. The goal of this work is rather to study the systematic effect of different factors - equation of state, solar irradiation, a deep thermal barrier - on the planetary evolution and assess their individual effects, regardless of whatever additional processes may act upon the planet in reality. The real answer will probably lie in a combination of a number of different factors contributing to the overall planetary evolution and causing Uranus’ and Neptune’s unique characteristics in conjunction with each other.

Chapter 2.

Fundamentals of planet modelling

2.1. Equations of planetary structure

There are a number of fundamental equations that describe planetary models. Let us start with mass conservation:

It is useful to assume the planet to be spherically symmetric and made up of concentric infinitesimal spherical shells with a mass of dm , a thickness of dr , and a Volume of dV . Thus, the variable m denotes the total mass contained inside a given shell at a given time. For a fixed time, the mass of one of the shells - under the assumption that its local density ρ stays constant within the shell - is:

$$\begin{aligned} dm &= \rho dV = \rho \left(\frac{4\pi}{3} (r + dr)^3 - \frac{4\pi}{3} r^3 \right) \\ &= \rho \frac{4\pi}{3} (r^3 + 3r^2 dr + 3r dr^2 + dr^3 - r^3) \approx 4\pi \rho r^2 dr. \end{aligned} \quad (2.1)$$

Since the mass contained in sphere r can change with time, e.g. due to contraction or mass transport, this leads to the partial derivative

$$\frac{\partial m(r, t)}{\partial r} = 4\pi \rho r^2. \quad (2.2)$$

Since the planet's total mass M_p is considered constant in time, while the radius changes during its lifetime, it is convenient to take m as the independent variable instead of r , and Eq. (2.2) is transformed to

$$\boxed{\frac{\partial r(m, t)}{\partial m} = \frac{1}{4\pi \rho r^2}}, \quad (2.3)$$

which will be the first basic equation.

Let us now consider the forces acting on an infinitesimal mass element dm at radius r . The gravitational force acting upon it is

$$dF_{\text{grav}} = -\frac{Gm}{r^2} dm, \quad (2.4)$$

where G is the gravitational constant and m , as defined above, is the mass contained in the sphere of radius r . The gravitational force on the mass element are counter-balanced by the gradient of the pressure increasing inwards, which generates a force directed outward. If we take the mass element to be cylindrical, with a base area A , height dr , volume $dV = A dr$, and density $\rho = \frac{dm}{dV}$, and the main axis parallel to r , this force is

$$dF_P = P(r, t)A - P(r + dr, t)A = -\frac{dV}{dr}(P(r + dr, t) - P(r, t)) = -\frac{dm}{\rho} \frac{\partial P(r, t)}{\partial r}, \quad (2.5)$$

where P is the local pressure. Under the assumption of hydrostatic equilibrium, for a non-rotating spherical planet, the forces of gravity and the pressure gradient cancel each other out and we get

$$0 = dF_{\text{grav}} + dF_P = -\frac{Gm}{r^2} dm - \frac{dm}{\rho} \frac{\partial P(r, t)}{\partial r},$$

$$\frac{\partial P(r, t)}{\partial r} = -\frac{Gm\rho}{r^2}, \quad (2.6)$$

which is called the equation of hydrostatic equilibrium.

If rotation is taken into account, in addition to dF_{grav} and dF_P a centrifugal force $d\vec{F}_c$ acts on the mass element as

$$d\vec{F}_c = -dm \vec{\omega} \times (\vec{\omega} \times \vec{r}), \quad (2.7)$$

where $\vec{\omega}$ is the planet's angular velocity. Since this force acts perpendicular to the rotation axis, the problem is no longer spherically symmetric. However, following the procedure laid out by Ref. [103], we can obtain an approximate term for F_c :

$$dF_c \approx dm \frac{2}{3} \omega^2 r. \quad (2.8)$$

A derivation of this term can be found in Appendix B.1. Combining Eqs. (2.6) and (2.8), we obtain

$$0 = -\frac{Gm}{r^2} dm - \frac{dm}{\rho} \frac{\partial P(r, t)}{\partial r} + dm \frac{2}{3} \omega^2 r, \quad (2.9)$$

$$\frac{\partial P(r, t)}{\partial r} = -\frac{Gm\rho}{r^2} + \frac{2}{3} \omega^2 r \rho.$$

and, using Eq. (2.3) to write the equation in terms of m ,

$$\boxed{\frac{\partial P(m, t)}{\partial m} = -\frac{Gm}{4\pi r^4} + \frac{\omega^2}{6\pi r}}, \quad (2.10)$$

which is the second basic equation of the models.

Now, we define a quantity for the dimensionless gradient of the temperature T with pressure [70]

$$\nabla_T := \frac{d \ln T}{d \ln P} = \frac{P}{T} \frac{dT}{dP}. \quad (2.11)$$

With the use of Eqs. (2.10) and (2.11), we can formulate the temperature profile in the planet with respect to m

$$\boxed{\frac{\partial T(m, t)}{\partial m} = \left(-\frac{Gm}{4\pi r^4} + \frac{\omega^2}{6\pi r} \right) \frac{T}{P} \nabla_T}, \quad (2.12)$$

the third fundamental equation. Obviously, ∇_T is the key quantity here. It depends strongly on the conditions in the planet and the process by which energy is transported. This will be discussed in the following section.

2.2. Heat transport within planets

2.2.1. The luminosity equation

In accordance with Ref. [70], let us define the local luminosity $l(m, t)$ as the heat per time transported through the surface of the sphere of mass m within the planet. It is defined such that positive l means heat is transported outward. The total luminosity

at the planet's outer boundary is called L , with

$$L = \int_0^{M_p} \frac{\partial l}{\partial m} dm, \quad (2.13)$$

where M_p is the planet's total mass. There are several processes contributing to the luminosity, a few of which are:

$$dl = dl_{\text{sec}} + dl_{\text{radio}} + dl_{\text{tide}} + \dots \quad (2.14)$$

The centrepiece of the luminosity for giant planets is the *secular cooling* dl_{sec} , describing change in heat content over time. There can be further processes contributing to the luminosity. For example, dl_{radio} represents heat produced through nuclear reactions, in planets most notable through radioactive decay. Another term is dl_{tide} , the heating through tidal interactions between the planet and its satellite, or, in case of exoplanets with very small orbital distances to their host stars, between planet and star. Another influence of significance can be Ohmic dissipation, a process where fast winds in a hot and irradiated atmosphere of a planet with a strong magnetic field can induce currents in the deep interior, where they deposit heat through resistive heating [6, 125]. This process is potentially very relevant for close-in, highly irradiated exoplanets [6, 25, 76, 125].

Secular cooling is defined as [70]

$$\frac{\partial l_{\text{sec}}}{\partial m} = -\frac{\partial q}{\partial t}, \quad (2.15)$$

with q the heat per unit mass. Let us assume a composition that does not change with time. Then, we can use the first law of thermodynamics for constant particle number

$$\delta q = du + P dv = du - \frac{P}{\rho^2} d\rho, \quad (2.16)$$

with the specific internal energy u and specific volume v . Inserting this into Eq. (2.15) gives

$$\frac{\partial l_{\text{sec}}}{\partial m} = -\frac{\partial u}{\partial t} + \frac{P}{\rho^2} \frac{\partial \rho}{\partial t}. \quad (2.17)$$

The two terms on the right represent change of internal energy and mechanical work through expansion/contraction, which also represents the change in gravitational energy.

In this work, I neglect explicit treatment for the other terms in Eq. (2.14). To gain an approximation of the error made due to not regarding the heat from nuclear reactions, I use the approximation of Guillot *et al.* (1995) for the total radioactive luminosity [44]

$$\frac{L_{\text{radio}}}{m_{\text{rocks}}} = 2 \times 10^{13} \frac{\text{W}}{M_{\text{E}}}, \quad (2.18)$$

where m_{rocks} is the mass of rocky material in the model in question and M_{E} denotes the Earth mass. For an ice-rich Uranus model with a rock core of about $0.8 M_{\text{E}}$ – e.g. model “Uranus 2” in Chap. 5 – this is about $L_{\text{radio}} \approx 1.6 \times 10^{13} \text{ W}$, which is about 5 % of Uranus’ total intrinsic luminosity of about $3.4 \times 10^{14} \text{ W}$ [45]. On the other hand, some of the models calculated for this work have a higher rock content of about $2.5 M_{\text{E}}$ in the case of the hot superadiabatic Uranus model examined in Sect. 6.6. In that example, the heating contribution from nuclear reactions in the rocky material is closer to 15 % of the intrinsic luminosity of Uranus. For Neptune, with its similar rock content to Uranus but much higher intrinsic luminosity of $3.3 \times 10^{15} \text{ W}$, the relative contributions are smaller. This means that my models will somewhat underestimate the time it takes to cool to today’s observed state, or, equivalently, underestimate the present-day total luminosity. For more information on the influence of l_{radio} , see App. D.

The tidal heating for Neptune l_{tid} primarily results from the obliquity of its largest moon Triton, i.e. the angle of inclination between Triton’s orbit and Neptune’s equator. Based on the formula for obliquity heating presented by Millholland (2019) [99], and using the parameters for Triton from the NASA Neptunian Satellite Fact Sheet [145], the total obliquity heating term for Neptune can be estimated as

$$L_{\text{obl,N}} \approx \frac{1}{Q_{\text{N}}} \times 5.3 \times 10^{15} \text{ W}, \quad (2.19)$$

where Q_{N} is the tidal quality factor of Neptune. Using the value of Zhang & Hamilton (2018) of $Q_{\text{N}} > 9000$, we can estimate $L_{\text{tidal}} < 6 \times 10^{11} \text{ W}$, which is only 2×10^{-4} times Neptune’s intrinsic luminosity of about $3.3 \times 10^{15} \text{ W}$ [45], and thus safely negligible. Even the much lower tidal quality factor of $Q_{\text{N}} = 100$ estimated by Goldreich *et al.* (1989) [40] leads to $L_{\text{tidal}} \approx 5.3 \times 10^{13} \text{ W}$, which is still only about 1.6 % of L_{int} . For Uranus this contribution is even less, because tidal heating scales with the mass of the satellite, and Uranus’ largest satellite Titania is smaller than Triton by a factor of about 6, and it additionally has a much smaller obliquity [145]. A second contribution to tidal heating arises from the satellites’ orbital eccentricity, i.e. how much the orbit deviates from a circle. This contribution can be estimated using Eq. (4) of Miller *et al.*

(2009) [98] to about

$$L_{\text{ecc, N}} \approx \frac{1}{Q_{\text{N}}} \times 1 \times 10^5 \text{ W}, \quad L_{\text{ecc, U}} \approx \frac{1}{Q_{\text{U}}} \times 1 \times 10^6 \text{ W}, \quad (2.20)$$

for Neptune and Uranus, respectively, which is even lower than the obliquity contribution. Therefore, tidal heating can be safely ignored.

Consequently, because my models only take into account l_{sec} explicitly, the luminosity equation as relevant for this work is simply Eq. (2.17):

$$\frac{\partial l}{\partial m} = \frac{\partial l_{\text{sec}}}{\partial m} = -\frac{\partial u}{\partial t} + \frac{P}{\rho^2} \frac{\partial \rho}{\partial t}. \quad (2.21)$$

In order to formulate the equation in terms of the thermodynamic quantities P, T , we introduce the isobaric specific heat capacity c_p and coefficient of expansion δ_ρ as

$$c_p = \left(\frac{\partial q}{\partial T} \right)_P = \left(\frac{\partial u}{\partial T} \right)_P + P \left(\frac{\partial v}{\partial T} \right)_P = \left(\frac{\partial u}{\partial T} \right)_P - \frac{P}{\rho^2} \left(\frac{\partial \rho}{\partial T} \right)_P, \quad (2.22)$$

$$\delta_\rho = - \left(\frac{\partial \ln \rho}{\partial \ln T} \right)_P = - \frac{T}{\rho} \left(\frac{\partial \rho}{\partial T} \right)_P. \quad (2.23)$$

One can show that [70]

$$dq = c_p dT - \frac{\delta_\rho}{\rho} dP. \quad (2.24)$$

The proof for this can be found in Appendix B.2. With this, we can then write Eq. (2.21) as

$$\boxed{\frac{\partial l}{\partial m} = c_p \frac{\partial T}{\partial t} + \frac{\delta_\rho}{\rho} \frac{\partial P}{\partial t}}. \quad (2.25)$$

The quantities in this relation all depend on T and P via the equations of state $u(P, T)$ and $\rho(P, T)$, which will be discussed in Chap. 4. It relates the planetary profile in P and T to the heat flow and, thus, the planet's structure to its thermal evolution, i.e. how its temperature, pressure and radius profiles change over time. The heat is transported via three major processes - radiation, conduction, and convection - which shall be discussed in the following sections.

2.2.2. Radiative and conductive heat transport

Both heat transport by radiation and conduction can be described in a shared framework, following the procedure laid out by Kippenhahn *et al.* [70].

Heat conduction describes transfer of energy via collisions between particles in the material. The conductive heat flux, $\vec{j}_{Q,cd}$, i.e. the heat transported per unit area and time, is proportional to the gradient in temperature according to Fourier's law of thermal conduction [70, 129]:

$$\vec{j}_{Q,cd} = -\lambda_{cd} \text{grad}T, \quad (2.26)$$

where λ_{cd} is the coefficient of thermal conduction, or thermal conductivity. In spherical symmetry, $\vec{j}_{Q,cd}$ can be replaced by its radial component, and the gradient of the temperature by its radius derivative, giving

$$j_{Q,cd} = -\lambda_{cd} \frac{\partial T}{\partial r}. \quad (2.27)$$

Radiation, on the other hand, is the energy transport via electromagnetic waves, e.g. visible or infrared light, which can be quantised as photons. If the mean free path of the photons is shorter than the radius length scale, this process can be described by a diffusion equation [70]

$$\vec{j}_{Q,rd} = -D \text{grad}U \quad (2.28)$$

where U is the energy density of radiation

$$U = aT^4, \quad (2.29)$$

a the radiation density constant, and D is the coefficient of diffusion. The latter one can be written as [20, 70]

$$D = \frac{v\ell_p}{3}. \quad (2.30)$$

Here, v denotes the mean velocity of the particles in the diffusive process – in this case photons – and ℓ_p their mean free path. The velocity is simply the speed of light c and

ℓ_p is [70]

$$\ell_p = \frac{1}{\kappa\rho}, \quad (2.31)$$

with the Rosseland mean opacity κ . Inserting Eq. (2.31) into (2.30), and inserting that and Eq.(2.29) into Eq. (2.28), we arrive at

$$\vec{j}_{Q,\text{rd}} = -\frac{4acT^3}{3\kappa\rho} \text{grad}T. \quad (2.32)$$

This has the same structure as Eq. (2.26), and therefore we can formally define the radiative conductivity λ_{rd} as

$$\lambda_{\text{rd}} = \frac{4acT^3}{3\kappa\rho}, \quad (2.33)$$

and, as in the conductive case, make use of spherical symmetry to obtain

$$j_{Q,\text{rd}} = -\lambda_{\text{rd}} \frac{\partial T}{\partial r}. \quad (2.34)$$

The combined heat flux via conduction and radiation can then be written as

$$j_Q = j_{Q,\text{rd}} + j_{Q,\text{cd}} = -\underbrace{(\lambda_{\text{rd}} + \lambda_{\text{cd}})}_{\lambda} \frac{\partial T}{\partial r}. \quad (2.35)$$

Replacing j_Q via $l = 4\pi r^2 j_Q$, and making use of Eq. (2.3), this can be transformed to

$$l = -4\pi r^2 \lambda 4\pi \rho r^2 \frac{\partial T}{\partial m} = -16\pi^2 r^4 \lambda \rho \frac{\partial T}{\partial m}. \quad (2.36)$$

Using Eq. (2.12) for the temperature derivative, this becomes

$$\begin{aligned} l &= -16\pi^2 r^4 \lambda \rho \left(-\frac{Gm}{4\pi r^4} + \frac{\omega^2}{6\pi r} \right) \frac{T}{P} \nabla_T \\ &= 8\pi r^3 \lambda \rho \left(\frac{Gm}{2r^3} - \frac{\omega^2}{3} \right) \frac{T}{P} \nabla_T, \end{aligned} \quad (2.37)$$

as the conductive and radiative luminosity in a region with a particular temperature gradient ∇_T . If we now solve Eq. (2.37) for ∇_T , we obtain the temperature gradient necessary to support a given luminosity l purely by conduction and radiation, a

quantity we shall call ∇_{cond} ,

$$\begin{aligned}\nabla_{\text{cond}} &= \frac{l}{8\pi r^3 \lambda \rho T} \frac{P}{T} \left(\frac{Gm}{2r^3} - \frac{\omega^2}{3} \right)^{-1} \\ &= \frac{lP}{4\pi Gm\lambda\rho T} \left(1 - \frac{2\omega^2 r^3}{3Gm} \right)^{-1}.\end{aligned}\quad (2.38)$$

This differs from the corresponding term in Kippenhahn *et al.* [70] mainly in the second term in parentheses, which describes the influence of rotation on ∇_{cond} , while Kippenhahn *et al.* do not take rotation into account there. Since this rotational term is proportional to r^3 and inversely proportional to m , it is largest on the planet's outer boundary. For present-day Neptune ($M_{\text{p}} = 1.02 \times 10^{26}$ kg, $R_{\text{p}} = 2.46 \times 10^7$ m, rotational period $\mathcal{P}_{\omega} = 5.8 \times 10^4$ s), it contributes to ∇_{cond} by about 1.7%, while for the more quickly rotating Jupiter ($M_{\text{p}} = 1.90 \times 10^{27}$ kg, $R_{\text{p}} = 6.90 \times 10^7$ m, $\mathcal{P}_{\omega} = 3.57 \times 10^4$ s) [45], it is about 5.6%. In the ice giant models presented in Chap. 6, a simplified temperature gradient of

$$\nabla_{\text{cond}} \approx \frac{lP}{4\pi Gm\lambda\rho T} \quad (2.39)$$

was used since the additional term was small in all cases. This is discussed in more detail in Chap. E.

2.2.3. Convective energy transport

In convection, energy is transported via the movement of mass elements. A mass package that is, through some fluctuation, slightly hotter than the surrounding, will rise due to buoyancy, until its density is equilibrated with the surrounding, where it dissolves and deposits its heat. Thus, convection cannot occur if density in the surrounding changes more quickly with depth than in the fluid element.

If we assume, following the procedure in Ref. [70], that the element is in pressure equilibrium with the environment throughout its rise, but has no energy exchange during it, that means that it behaves adiabatically. Then, convection is suppressed if

$$\frac{d\rho}{dP} \geq \left(\frac{\partial\rho}{\partial P} \right)_{s, \{X_j\}}, \quad (2.40)$$

where the left-hand side is the derivative taken along the planetary profile, representing the surroundings, and the right-hand side is evaluated for constant composition and specific entropy s , representing the adiabatically expanding fluid element.

The stability condition Eq. (2.40) can be used to derive a more easily accessible criterion, for which we will follow the approach outlined in the work of Vazan *et al.* (2015) [137]. In this description, all thermodynamic quantities depend on pressure P , temperature T , and the material's composition, represented by the mass fractions X_j of the different components. Therefore, the total differential of ρ can be written as

$$d\rho = \left(\frac{\partial\rho}{\partial P}\right)_{T,\{X_j\}} dP + \left(\frac{\partial\rho}{\partial T}\right)_{P,\{X_j\}} dT + \sum_i \left(\frac{\partial\rho}{\partial X_j}\right)_{P,T,\{X_{k\neq i}\}} dX_i, \quad (2.41)$$

$$\frac{d\rho}{dP} = \left(\frac{\partial\rho}{\partial P}\right)_{T,\{X_j\}} + \left(\frac{\partial\rho}{\partial T}\right)_{P,\{X_j\}} \frac{dT}{dP} + \sum_i \left(\frac{\partial\rho}{\partial X_i}\right)_{P,T,\{X_{k\neq i}\}} \frac{dX_i}{dP}. \quad (2.42)$$

Using the cyclic chain rule $\left(\frac{\partial x}{\partial y}\right)_z \left(\frac{\partial y}{\partial z}\right)_x \left(\frac{\partial z}{\partial x}\right)_y = -1$, we can rewrite

$$\left(\frac{\partial\rho}{\partial X_i}\right)_{P,T,\{X_{k\neq i}\}} = - \left(\frac{\partial T}{\partial X_i}\right)_{P,\rho,\{X_{k\neq i}\}} \left(\frac{\partial\rho}{\partial T}\right)_{P,\{X_j\}}, \quad (2.43)$$

and therefore, the left-hand side of Eq. (2.40) becomes

$$\frac{d\rho}{dP} = \left(\frac{\partial\rho}{\partial P}\right)_{T,\{X_j\}} + \left(\frac{\partial\rho}{\partial T}\right)_{P,\{X_j\}} \frac{dT}{dP} - \left(\frac{\partial\rho}{\partial T}\right)_{P,\{X_j\}} \sum_i \frac{dX_i}{dP} \left(\frac{\partial T}{\partial X_i}\right)_{P,\rho,\{X_{k\neq i}\}}. \quad (2.44)$$

Here, we introduce the quantity, again following the nomenclature in Ref. [137],

$$\nabla_X = \sum_i \frac{dX_i}{d\ln P} \left(\frac{\partial \ln T}{\partial X_i}\right)_{P,\rho,\{X_{k\neq i}\}} = \frac{P}{T} \sum_i \frac{dX_i}{dP} \left(\frac{\partial T}{\partial X_i}\right)_{P,\rho,\{X_{k\neq i}\}}. \quad (2.45)$$

Here, $\frac{dX_i}{dP}$ is the change of composition with increasing pressure along the given planetary profile. The partial derivative $\left(\frac{\partial T}{\partial X_i}\right)_{P,\rho,\{X_{k\neq i}\}}$ represents the change in temperature due to changing composition locally. For that latter derivative and how it is calculated in practice, see App. B.4.

We also make use of the quantity already established in Eq. (2.11)

$$\nabla_T = \frac{d\ln T}{d\ln P} = \frac{P}{T} \frac{dT}{dP}, \quad (2.46)$$

which is the temperature gradient that is actually realised in the planetary profile and along which s and $\{X_i\}$ may vary. With Eq. (2.45) and Eq. (2.46), Eq. (2.44) becomes

$$\begin{aligned} \frac{d\rho}{dP} &= \left(\frac{\partial\rho}{\partial P}\right)_{T,\{X_j\}} + \frac{T}{P} \left(\frac{\partial\rho}{\partial T}\right)_{P,\{X_j\}} \nabla_T - \frac{T}{P} \left(\frac{\partial\rho}{\partial T}\right)_{P,\{X_j\}} \nabla_X \\ &= \left(\frac{\partial\rho}{\partial P}\right)_{T,\{X_j\}} + \frac{T}{P} \left(\frac{\partial\rho}{\partial T}\right)_{P,\{X_j\}} [\nabla_T - \nabla_X]. \end{aligned} \quad (2.47)$$

Now, for the right-hand side of Eq. (2.40), we can use a multi-variable chain rule, which in general for two independent variables reads [11]:

$$\frac{\partial w(u, v)}{\partial u} = \frac{\partial w(y, z)}{\partial y} \frac{\partial y(u, v)}{\partial u} + \frac{\partial w(y, z)}{\partial z} \frac{\partial z(u, v)}{\partial u}. \quad (2.48)$$

In our case, we take $w = \rho$, $u = y = P$, $v = s$, and $z = T(P, s)$. Thus, we can switch from $\rho(P, s, X)$ to $\rho(P, T, X)$ via:

$$\left(\frac{\partial\rho}{\partial P}\right)_{s,\{X_j\}} = \left(\frac{\partial\rho}{\partial P}\right)_{T,\{X_j\}} + \left(\frac{\partial\rho}{\partial T}\right)_{P,\{X_j\}} \left(\frac{\partial T}{\partial P}\right)_{s,\{X_j\}}. \quad (2.49)$$

Similar to Eq. (2.46), one can introduce

$$\nabla_{\text{ad}} = \left(\frac{\partial \ln T}{\partial \ln P}\right)_{s,\{X_j\}} = \frac{P}{T} \left(\frac{\partial T}{\partial P}\right)_{s,\{X_j\}}, \quad (2.50)$$

which is the change in temperature with pressure for constant entropy, or, in short, the *adiabatic temperature gradient*. With this, Eq. (2.49) becomes

$$\left(\frac{\partial\rho}{\partial P}\right)_{s,\{X_j\}} = \left(\frac{\partial\rho}{\partial P}\right)_{T,\{X_j\}} + \frac{T}{P} \left(\frac{\partial\rho}{\partial T}\right)_{P,\{X_j\}} \nabla_{\text{ad}}. \quad (2.51)$$

Now combining Eqs. (2.47) and (2.51), Eq. (2.40) becomes

$$\left(\frac{\partial\rho}{\partial T}\right)_{P,\{X_j\}} [\nabla_T - \nabla_X] \geq \left(\frac{\partial\rho}{\partial T}\right)_{P,\{X_j\}} \nabla_{\text{ad}}, \quad (2.52)$$

and, assuming a material with positive thermal expansion coefficient, i. e. where $\left(\frac{\partial\rho}{\partial T}\right)_{P,\{X_j\}} < 0$ holds, we arrive at:

$$\boxed{\nabla_T \leq \nabla_X + \nabla_{\text{ad}}}, \quad (2.53)$$

as a criterion for dynamical stability, which we shall call the generalised Ledoux criterion, as in Ref. [137]. This shows that convection can be inhibited by a sufficiently large compositional gradient. In a homogenous medium absent of any changes in composition, $\nabla_X = 0$ and the condition (2.53) becomes the Schwarzschild criterion

$$\nabla_T \leq \nabla_{\text{ad}}. \quad (2.54)$$

Thus in a convective, homogeneous region of the planet, the medium adopts a temperature gradient ∇_T with

$$\nabla_{\text{ad}} < \nabla_T < \nabla_{\text{rad}}. \quad (2.55)$$

To calculate ∇_T accurately, a detailed description of the hydrodynamics of convection is needed. For this, the Navier-Stokes equations of fluid dynamics have to be calculated, including a detailed description of local particle fluxes [108, 135]. This is beyond the scope of stellar and planetary structure and evolution codes due to the high computational cost involved. There is, however, a way of approximating it using mixing-length theory [70]. It is based on the assumption that convecting fluid elements travel an average distance, the mixing length l_m , before dissolving in their surroundings, and that the heat flux and local temperature gradient can be calculated based on that. The mixing length is usually expressed in terms of the pressure scale height $l_m = \alpha H_P$, where α is called the mixing length parameter, which is not known and for which an assumption has to be made [46, 70]. Using mixing length theory, one can derive an expression for the superadiabaticity, i.e. the amount the local ∇_T exceeds the adiabatic gradient, which reads [46]:

$$\nabla_T - \nabla_{\text{ad}} = \left(\frac{4\sqrt{2}j_{Q,\text{conv}}}{\alpha^2 c_p T \sqrt{\delta \rho P}} \right)^{\frac{2}{3}}, \quad (2.56)$$

where $j_{Q,\text{conv}}$ is the heat flux transported by convection. Using the assumption of $\alpha = 1$, as well as the total observed heat flux $j_{Q,\text{surface}}$ as an upper bound for $j_{Q,\text{conv}}$, Guillot *et al.* (2004) [46] estimate the superadiabaticity inside Jupiter to be about 1×10^{-5} in the atmosphere and smaller than 1×10^{-8} in the deep interior. Using the same approximations for $j_{Q,\text{conv}}$ and α as Ref. [46], and taking the material properties along adiabatic Uranus and Neptune profiles Uranus 2 and Neptune 2 from Sect. 5, yields values for $\nabla_T - \nabla_{\text{ad}} < 7 \times 10^{-6}$ at the outer edge of the planets and $\nabla_T - \nabla_{\text{ad}} < 1 \times 10^{-8}$ in the deep interior. It is thus a reasonable approximation to assume the

temperature gradient in convective zones as adiabatic for our ice giant models as well as for Jupiter-like planets. Using the thermodynamic quantities P , T , and ρ , as well as the material properties c_p and δ_ρ , the adiabatic temperature gradient can be calculated as

$$\nabla_{\text{ad}} = \frac{P\delta_\rho}{T\rho c_p}, \quad (2.57)$$

which is derived in App. B.3.

The real situation of energy transport is not quite as clear-cut as implied by the description here. Apart from strong, overturning convection and complete stable stratification with heat transported by pure conduction and radiation, there are intermediate regimes which can occur. In the event of a stabilising compositional gradient and a destabilising thermal gradient – i.e. if a region is stable according to the Ledoux criterion (2.53), but would be unstable under the Schwarzschild criterion (2.54) – a family of processes called “double diffusive convection” can occur [135]. This takes the form of either *oscillatory convection*, where mass elements oscillate around an equilibrium position, resulting in heat transport without particle transport [39, 136], or *layered convection*, where a number of small convective layers are separated by conductive interfaces, which are prone to frequent turbulence [79, 101].

Whether such a region is stably stratified or in one of these double-diffusive regimes depends on a large number of material properties, among them the viscosity, thermal conductivity, heat capacity, and diffusion coefficients of the different materials in the mixture. For a more in-depth explanation of double diffusive processes, see Chap. 11 in Turner (1973) [135]. Regarding the applications in planetary physics, see e.g. Leconte & Chabrier (2012) [79] or Nettelmann *et al.* (2015) [101], both relating to Jupiter, and references therein. For Uranus and Neptune, French & Nettelmann (2019) [34] estimate, using viscosity and conductivity values for pure water, that there is only a rather narrow window of parameters for double diffusive convection to occur, without it turning into full overturning convection or being stably stratified. Because of this, as well as the fact that an explicit treatment of double-diffusive convection is quite complex and beyond the scope of this work, it is not directly included in the models of this work. Nevertheless, since there are still uncertainties surrounding this topic, double diffusive convection might very well play an important role and cannot be wholly dismissed.

2.3. Summary of basic equations

To summarise, the four basic equations, as derived previously and presented in Eqs. (2.3), (2.10), (2.12), and (2.25), are:

$$\frac{\partial r}{\partial m} = \frac{1}{4\pi r^2 \rho}, \quad (2.58a)$$

$$\frac{\partial P}{\partial m} = -\frac{Gm}{4\pi r^4} + \frac{\omega^2}{6\pi r}, \quad (2.58b)$$

$$\frac{\partial T}{\partial m} = \left(-\frac{Gm}{4\pi r^4} + \frac{\omega^2}{6\pi r} \right) \frac{T}{P} \nabla_T, \quad (2.58c)$$

$$\frac{\partial l}{\partial m} = -\frac{\partial u}{\partial t} + \frac{P}{\rho^2} \frac{\partial \rho}{\partial t} = -c_p \frac{\partial T}{\partial t} + \frac{\delta_\rho}{\rho} \frac{\partial P}{\partial t}, \quad (2.58d)$$

where ∇_T in Eq. (2.58c) changes depending on which regime of energy transport the material adopts, for which we have presented methods of calculating under various conditions. Solving these equations will yield a series of profiles representing the planet's evolution. The procedure to do so will be detailed in the next Chap. 3.

Chapter 3.

Numerical procedure

After deriving the basic equations of planet modelling and evolution in Chap. 2, let us now turn to the question of how to solve them. First, I will present at the boundary conditions of these planetary models, followed by a discussion of the theoretical method used for the models presented in this work, which is an adaptation of the Henyey-method for stellar structure and evolution calculations. Then I will present information regarding the practical implementation of that method in the computer program I have developed for this work.

3.1. Boundary Conditions

In the planet's centre at $m = 0$, it is evident that $r(m = 0) = 0$ must hold. Based on the assumption that ρ does not vary near the centre for sufficiently small values of m and r , Eq. (2.58a) can be approximately integrated near the centre for constant ρ_c [70]:

$$r_c = \left(\frac{3m_c}{4\pi\rho_c} \right)^{\frac{1}{3}}. \quad (3.1)$$

Similarly, since there are no energy sources in the centre, it must also hold that $l(m = 0) = 0$ and therefore, that the luminosity at the innermost point in our model is

$$l_c = \left(-c_p \frac{\partial T}{\partial t} + \frac{\delta_\rho}{\rho} \frac{\partial P}{\partial t} \right) m_c, \quad (3.2)$$

where m_c is the innermost mass shell.

A comprehensive treatment of the outer boundary conditions would involve model-

ling atmospheric processes where, due to the low density and low opacity, radiative transport becomes increasingly important. Since this work is more interested in the structure and processes of the deep interior, we will instead adopt an approximation inspired by, e.g., Ref. [105]. First, we define the surface of our models to be at a pressure of

$$P(m = M_p) := 1 \text{ bar}, \quad (3.3)$$

which is standard practice in many interior models of Uranus and Neptune, cf., e.g., Refs. [4, 46, 105], and evolution models, e.g. [24, 102, 105], due to the fact that the atmospheric P - T -profile inferred from Voyager measurements for Uranus [83] and Neptune [84] are close to an adiabat below that pressure. Eq. (3.3) will serve as the first outer boundary condition. For the second, we turn to the observed luminosity of the planet, which is

$$L_{\text{obs}} = L_{\text{int}} + L_{\text{sol}}, \quad (3.4)$$

where L_{int} is the total intrinsic luminosity of the planet, and thus $L_{\text{int}} = l(m = M_p)$, and L_{sol} the solar irradiation absorbed and then re-emitted by the planet. Using the Stefan-Boltzmann law [70], we can express L_{int} and L_{sol} as functions of the planet's effective and equilibrium temperatures respectively:

$$L = 4\pi R_p^2 \sigma_B T_{\text{eff}}^4, \quad (3.5)$$

$$L_{\text{sol}} = 4\pi R_p^2 \sigma_B T_{\text{eq}}^4. \quad (3.6)$$

The effective temperature T_{eff} of the planet is the temperature at which a black body sphere of the same radius as the planet would have to radiate heat with the same total luminosity. The equilibrium temperature T_{eq} is the effective temperature the planet would have, if it was in complete thermal equilibrium with its star. Thus, our second boundary condition is

$$l(m = M_p) := 4\pi R_p^2 \sigma_B T_{\text{eff}}^4 - 4\pi R_p^2 \sigma_B T_{\text{eq}}^4. \quad (3.7)$$

The equilibrium temperature T_{eq} can be calculated from the stellar and orbital parameters [102]

$$T_{\text{eq}}^4 = \frac{1}{4} T_*^4 (1 - A) \left(\frac{R_*}{a} \right)^2, \quad (3.8)$$

where T_* and R_* are the stellar temperature and radius, respectively, and a is the planet's mean orbital distance. A is its Bond albedo, that is, the share of irradiation that is outright reflected instead of absorbed and re-emitted. On the other hand, T_{eff} has to somehow be linked to a temperature inside the planet, where the P - T -profile follows an adiabat, in our case the 1-bar level, see Eq. (3.3). To this end, we will use a relation from Guillot *et al.* (1995) [44],

$$T_{1\text{bar}} = K g^{-1/6} T_{\text{eff}}^{3.73/3}. \quad (3.9)$$

This is based on a formula by Hubbard (1977) [63], interpolating model atmospheres for Jupiter calculated by Graboske *et al.* (1975) [41]. Here, $g = GM_{\text{p}}/R_{\text{p}}^2$ is the gravitational acceleration at the planet's surface, and K is an empirical parameter chosen so that the observed 1-bar-temperature emerges from Eq. (3.9). Using Uranus' and Neptune's accepted values for T_{eff} and $T_{1\text{bar}}$ – see App. A – gives values of $K_{\text{U}} = 1.481$ for Uranus and $K_{\text{N}} = 1.451$ for Neptune.

This description of the atmosphere is a simplification, as the model it is based on was developed for Jupiter which has a hotter and less heavy-element rich atmosphere than Neptune. Fortney *et al.* (2011) [24] calculated adiabatic Uranus and Neptune models both with the description used here and with a more detailed atmosphere model developed for the ice giants. They found that their own atmosphere model produced longer cooling times. For Neptune, this effect is on the order of ~ 0.2 Gyr. For Uranus, due to its very slow present-day cooling, it was found to be several Gyr, but the effect was shown to be no greater than that of the observational uncertainties of the intrinsic luminosity, and even their fastest-cooling Uranus model still strongly predicts an age that is too high [24]. Therefore, due to its ease of use, I will utilise Eq. (3.9), while noting that this probably produces too short cooling times for Uranus.

Having taken care of the boundary conditions, let us turn to the actual solution strategy.

3.2. The Henyey method

The approach used in this thesis to solve the structure equations is based on the description of the Henyey method of calculating stellar structure and evolution [54] in Chap. 12 of Kippenhahn *et al.* (2012) [70], with additional details for the implementation taken from Hofmeister *et al.* (1964) [56] and Kippenhahn *et al.* (1967) [69].

Equations (2.58) can be recast to the form

$$f_0 = \frac{\partial y_0}{\partial \xi} = -\frac{M_x}{4\pi \rho} \exp[\xi - 3y_0], \quad (3.10a)$$

$$f_1 = \frac{\partial y_1}{\partial \xi} = \frac{G M_x^2}{4\pi} (1 - e^\xi) \exp[\xi - 4y_0 - y_1] - \frac{\omega^2 M_x}{6\pi} \exp[\xi - y_0 - y_1], \quad (3.10b)$$

$$f_2 = \frac{\partial y_2}{\partial \xi} = \frac{G M_x^2}{4\pi} \nabla_T (1 - e^\xi) \exp[\xi - 4y_0 - y_1] - \frac{\omega^2 M_x}{6\pi} \nabla_T \exp[\xi - y_0 - y_1], \quad (3.10c)$$

$$f_3 = \frac{\partial y_3}{\partial \xi} = -M_x \left(-c_p \frac{\partial}{\partial t} e^{y_2} + \frac{\delta_\rho}{\rho} \frac{\partial}{\partial t} e^{y_1} \right) \exp[\xi - y_3]. \quad (3.10d)$$

Here y_i are the logarithmic main variables $y_0 = \ln(r)$, $y_1 = \ln(P)$, $y_2 = \ln(T)$, and $y_3 = \ln(l + L_c)$, where L_c is a constant added to the luminosity in cases where we have to allow for $l < 0$. The mass coordinate of the models is $\xi = \ln\left(1 - \frac{m}{M_x}\right)$, with $M_x = 1.05 M_p$, following Ref. [69].

To solve this system of differential equations, a variant of the Henyey method of calculating stellar structure and evolution [54] is used, as presented in Kippenhahn *et al.* (2012) [70]. The model is calculated on a discretised 1-dimensional grid of N mass points, numbered $j = 0 \dots N - 1$, where $j = 0$ denotes the outer boundary and $j = N - 1$ the innermost grid point. Instead of integrating the differential equations along the mass coordinate, as is the practice in the commonly used Runge-Kutta method, in this approach, the values of the dependent variables are solved for simultaneously, by solving a grid of difference equations using the Newton-Raphson method. The derivatives in Eqs. (3.10) are approximated as the corresponding difference quotients between the j -th and $(j + 1)$ -st grid point

$$\frac{\partial y_i}{\partial \xi} \approx \frac{y_i^{j+1} - y_i^j}{\xi^{j+1} - \xi^j} = \frac{y_i^{j+1} - y_i^j}{\Delta \xi^{j+1}}$$

For a profile of quantities y_i to fulfil the equations (3.10) in this approximation, the following equations must hold at every point:

$$G_i^j := \frac{y_i^{j+1} - y_i^j}{\Delta \xi^{j+1}} - f_i \left(y_0^{j+\frac{1}{2}}, y_1^{j+\frac{1}{2}}, y_2^{j+\frac{1}{2}}, y_3^{j+\frac{1}{2}} \right) = 0, \text{ with } i = 0, \dots, 3 \quad (3.11)$$

where the values $y_i^{j+1/2}$ are obtained as the arithmetic mean of the values at the j th and $(j + 1)$ st point and f_i are the functions defined by Eqs. (3.10). Similarly, the two outer boundary conditions (3.3) and (3.7) can be written as the two functions (with

$P_0 = 1$ bar:

$$B_0 := e^{y_1^0} - P_0 = 0, \quad (3.12)$$

$$B_1 := \ln(l^0) - \ln(4\pi\sigma_B) - 2y_0^0 - \ln(T_{\text{eff}}^4 - T_{\text{eq}}^4) = 0. \quad (3.13)$$

Between the last and the second-to-last grid point ξ^{N-1} and ξ^{N-2} , another set of equations is employed based on one of the central boundary conditions Eq. (3.1), following [56]. First, we take Eq. (3.1) to be true at ξ^{N-2} as well,

$$r(m) \approx \left(\frac{3m}{4\pi\rho_c} \right)^{\frac{1}{3}}. \quad (3.14)$$

Converted into our logarithmic units and discretised similarly to Eqs. (3.11), this becomes

$$C_0 := 3y_0^{N-2} - \ln\left(\frac{3}{4\pi}\right) + \ln(\rho_c) - \ln\left(M_x(1 - e^{\xi^{N-2}})\right) = 0. \quad (3.15)$$

Next, inserting Eq. (3.1) into Eq. (3.10b) gives a similar approximation for the pressure difference near the centre

$$\frac{\partial \ln y_1}{\partial \xi} \approx \frac{1}{6\pi} \left(\frac{4\pi}{3} \right)^{\frac{1}{3}} M_x^{\frac{2}{3}} (1 - e^\xi)^{-\frac{1}{3}} \exp[\xi - y_1] \left(2\pi G \rho_c^{\frac{4}{3}} - \omega^2 \rho_c^{\frac{1}{3}} \right), \quad (3.16)$$

which leads to the relation

$$C_1 := \frac{y_1^{N-1} - y_1^{N-2}}{\xi^{N-1} - \xi^{N-2}} - \frac{1}{6\pi} \left(\frac{4\pi}{3} \right)^{\frac{1}{3}} M_x^{\frac{2}{3}} (1 - e^{\xi^{N-2}})^{-\frac{1}{3}} \times \\ \times \exp[\xi^{N-2} - y_1^{N-2}] \left(2\pi G \rho_c^{\frac{4}{3}} - \omega^2 \rho_c^{\frac{1}{3}} \right) = 0. \quad (3.17)$$

For the third function near the centre the definition of ∇_T , Eq. (2.11), is used and we arrive at

$$C_2 := \frac{y_2^{N-1} - y_2^{N-2}}{y_1^{N-1} - y_1^{N-2}} - \nabla_T = 0. \quad (3.18)$$

No simplification is used for the fourth equation, and we use Eq. (3.10d) directly to arrive at

$$C_3 := \frac{y_3^{N-2} - y_3^{N-1}}{\xi^{N-1} - \xi^{N-2}} - f_3 \left(y_0^{N-\frac{3}{2}}, y_1^{N-\frac{3}{2}}, y_2^{N-\frac{3}{2}}, y_3^{N-\frac{3}{2}} \right) = 0. \quad (3.19)$$

Note that these functions differ somewhat from those presented in, e.g., Hofmeister *et al.* [56], because these forms turned out to be numerically more stable, and this work includes a description of rotation, which Hofmeister *et al.* neglect.

Thus, for N grid points in the model, this gives a system of $4N - 2$ equations. The unknown variables are y_i^j for $j = 0 \dots N - 1$. The variables y_0^{N-1} and y_3^{N-1} directly at the innermost point can be excluded, as their values are known via the central boundary conditions (3.1) and (3.2), leading to $4N - 2$ variables which the above $4N - 2$ equations have to be solved for.

To solve this system, a multi-dimensional Newton-Raphson method can be applied [70]. Let us assume that an approximate profile $(y_k^n)_0$; $k = 0, \dots, 3$; $n = 0, \dots, N - 1$ is available that does not fulfil Eqs. (3.11). Ideally, corrections δy_k^n have to be found so that

$$y_k^n = (y_k^n)_0 + \delta y_k^n, \quad (3.20)$$

$$G_i^j(y_k^n) = G_i^j((y_k^n)_0 + \delta y_k^n) = (G_i^j)_0 + \delta G_i^j = 0, \quad (3.21)$$

$$k = 0, \dots, 3; n = 0, \dots, N - 1.$$

We can Taylor-expand the functions G_i^j with respect to the variables y_k^n around the initial estimate solution $(y_k^n)_0$ [11]:

$$G_i^j = (G_i^j)_0 + \sum_{k=0}^3 \sum_{n=0}^{N-1} \frac{\partial G_i^j}{\partial y_k^n} \underbrace{(y_k^n - (y_k^n)_0)}_{\delta y_k^n} + \left(\sum_{k=0}^3 \sum_{n=0}^{N-1} \frac{\partial}{\partial y_k^n} \underbrace{(y_k^n - (y_k^n)_0)}_{\delta y_k^n} \right)^2 G_i^j + \dots, \quad (3.22)$$

and then, as a linear approximation, take only into account the terms linear in δy_k^n . Additionally, we can see from the definitions of G_i^j that they only depend on the values of y_n^j and y_n^{j+1} at the neighbouring points ξ_j and ξ_{j+1} , so that we arrive at [70]

$$0 = G_i^j \approx (G_i^j)_0 + \sum_{k=0}^3 \frac{\partial G_i^j}{\partial y_k^j} \delta y_k^j + \frac{\partial G_i^j}{\partial y_k^{j+1}} \delta y_k^{j+1}. \quad (3.23)$$

Combining this with similar treatments for the boundary conditions B_i , a system of equations can be formulated that has to be solved for the δy_n^k :

$$\frac{\partial B_i}{\partial y_0^0} \delta y_0^0 + \frac{\partial B_i}{\partial y_1^0} \delta y_1^0 + \frac{\partial B_i}{\partial y_2^0} \delta y_2^0 + \frac{\partial B_i}{\partial y_3^0} \delta y_3^0 = -(B_i)_0, \quad (3.24)$$

$$i = 0, 1,$$

$$\frac{\partial G_i^j}{\partial y_0^j} \delta y_0^j + \dots + \frac{\partial G_i^j}{\partial y_3^j} \delta y_3^j + \frac{\partial G_i^j}{\partial y_0^{j+1}} \delta y_0^{j+1} + \dots + \frac{\partial G_i^j}{\partial y_3^{j+1}} \delta y_3^{j+1} = -(G_i^j)_0, \quad (3.25)$$

$$i = 0, \dots, 3, \quad j = 0, \dots, N - 2.$$

This can be recast as the following matrix equation:

$$\underbrace{\begin{pmatrix} \frac{\partial B_0}{\partial y_0^0} & \frac{\partial B_0}{\partial y_1^0} & \dots & 0 \\ \frac{\partial B_1}{\partial y_0^0} & \frac{\partial B_1}{\partial y_1^0} & \dots & 0 \\ \frac{\partial G_0^0}{\partial y_0^0} & \frac{\partial G_0^0}{\partial y_1^0} & \dots & 0 \\ \vdots & \vdots & \ddots & \vdots \\ 0 & 0 & \dots & \frac{\partial C_3}{\partial y_2^{N-1}} \end{pmatrix}}_H \cdot \underbrace{\begin{pmatrix} \delta y_0^0 \\ \delta y_1^0 \\ \delta y_2^0 \\ \vdots \\ \delta y_2^{N-1} \end{pmatrix}}_{\vec{\delta y}} = - \underbrace{\begin{pmatrix} (B_0)_0 \\ (B_1)_0 \\ (G_0^0)_0 \\ \vdots \\ (C_3)_0 \end{pmatrix}}_{\vec{G}}. \quad (3.26)$$

The vector \vec{G} and matrix H are calculated for the estimated starting solution \vec{y}_0 , and then equation (3.26) is solved for $\vec{\delta y}$ and with this, a new solution \vec{y}_1 is constructed. Now, because we used a linearisation in Eq. (3.23), the new profile is also unlikely to actually fulfil $G_i^j = 0$, and is instead used to calculate updated \vec{G} and H . This is repeated until an intended level of convergence is found, see Sect. 3.3 for more on the convergence criterion.

As an example, consider a model with 4 points, $j = 0, \dots, 3$. The structure of the H -matrix for this case is shown in Fig. 3.1. As was already mentioned in the derivation of the method, because the functions G_i^j only depend on y_n^k at two neighbouring points each, the H -matrix is non-zero only in overlapping 8×4 blocks around the main diagonal, and zero everywhere else.

3.3. The OTTER Code

For this thesis, a computer program based on the principles outlined in Sect. 3.2 has been developed. It is called *OTHer Thermal Evolution Realisation* or OTTER for short

$$\begin{array}{c}
\begin{array}{cccc}
\overbrace{\hspace{2cm}}^{j=0} & & \overbrace{\hspace{2cm}}^{j=1} & & \overbrace{\hspace{2cm}}^{j=2} & & \overbrace{\hspace{2cm}}^{j=3} \\
y_0^0 & y_1^0 & y_2^0 & y_3^0 & y_0^1 & y_1^1 & y_2^1 & y_3^1 & y_0^2 & y_1^2 & y_2^2 & y_3^2 & y_1^3 & y_2^3
\end{array} \\
\left(\begin{array}{l}
B_1 \\
B_2 \\
G_0^0 \\
G_1^0 \\
G_2^0 \\
G_3^0 \\
G_0^1 \\
G_1^1 \\
G_2^1 \\
G_3^1 \\
C_0 \\
C_1 \\
C_2 \\
C_3
\end{array} \right.
\begin{array}{cccccccccccccc}
* & * & * & * & 0 & 0 & 0 & 0 & 0 & 0 & 0 & 0 & 0 & 0 \\
* & * & * & * & 0 & 0 & 0 & 0 & 0 & 0 & 0 & 0 & 0 & 0 \\
* & * & * & * & * & * & * & * & 0 & 0 & 0 & 0 & 0 & 0 \\
* & * & * & * & * & * & * & * & 0 & 0 & 0 & 0 & 0 & 0 \\
* & * & * & * & * & * & * & * & 0 & 0 & 0 & 0 & 0 & 0 \\
0 & 0 & 0 & 0 & * & * & * & * & * & * & * & * & 0 & 0 \\
0 & 0 & 0 & 0 & * & * & * & * & * & * & * & * & 0 & 0 \\
0 & 0 & 0 & 0 & * & * & * & * & * & * & * & * & 0 & 0 \\
0 & 0 & 0 & 0 & 0 & 0 & 0 & 0 & * & * & * & * & * & * \\
0 & 0 & 0 & 0 & 0 & 0 & 0 & 0 & * & * & * & * & * & * \\
0 & 0 & 0 & 0 & 0 & 0 & 0 & 0 & * & * & * & * & * & *
\end{array} \right)
\end{array}$$

Fig. 3.1.: The layout of the H matrix for an example model with 4 points. On the left are the 14 equations of the model, at the top we have the 14 independent variables. Non-zero entries are represented by an *. As an example, the entry in the third row (G_0^0), second column (y_1^0) represents the derivative $\partial G_0^0 / \partial y_1^0$. The figure is based on an analogous illustration in Ref. [70].

and is written in C++. To solve the matrix equation (3.26), the code makes use of the vector and sparse matrix functions from the *Eigen* library [43].

To obtain a planetary evolution track, a succession of profiles at different time steps is calculated. For a given point in time, an approximate solution is iteratively improved until a converged profile is found. This profile and the one from the previous time step are then used to estimate a solution for the next step, for which the whole process is then repeated. This series of profiles is linked via the time-derivatives in Eq. (2.58d), and from these, evolution curves of $R(t)$, $T_{\text{eff}}(t)$, etc. can be constructed.

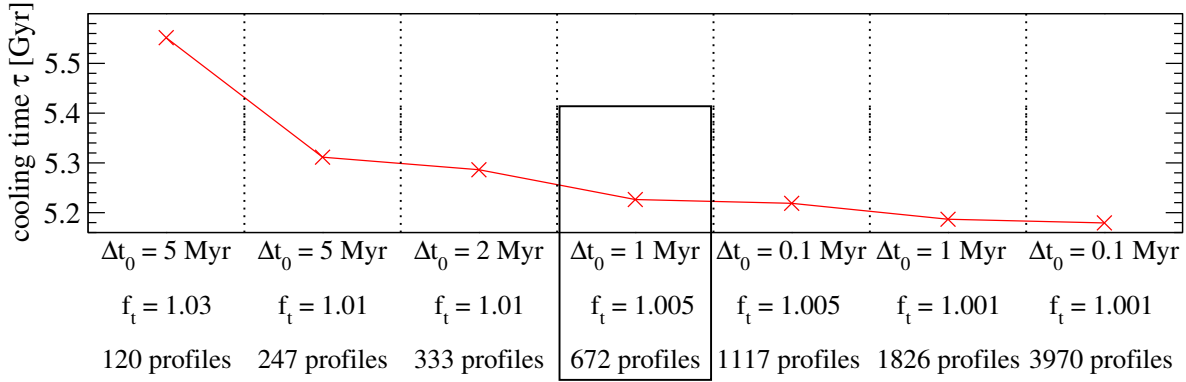
For the beginning of an evolution track, a profile with a predefined outer temperature $T_{1\text{bar}}$ is calculated as a starting point. The initial estimate that serves as starting solution for that profile, as well as the starting solution for the profile after the first time step, are usually taken from previous evolution calculations, or, for the first trial runs

with a new planet, were calculated with Nadine Nettelmann's planetary modelling tool MOGROP [103, 104].

The convergence criterion for the iterative solving of Eq. (3.26) at a certain time is $\delta y_i^j < 5 \times 10^{-8}$ for all i, j . For an arbitrarily chosen Neptune profile, this usually leads to $G_i^j \lesssim 2 \times 10^{-4}$, except for G_3^{N-1} - the luminosity equation at the innermost point - which is on the order of ~ 0.1 . For an evolution calculation for an adiabatic Neptune model over ca. 3.7 Gyr, the difference in effective cooling time between using this convergence criterion and using $\delta y_i^j < 1 \times 10^{-10}$ is on the order of $\sim 1 \times 10^{-9}$ Gyr. Usually, convergence is found within 10 iterations. Occasionally, a particular profile in an evolution calculation fails to converge in 80 steps, as the luminosity profile does not settle into a stable state. In these cases, if the changes in the profile over an iteration are within $\delta y_i^j < 1 \times 10^{-4}$, the evolution is continued with the last iteration of the current profile.

The length of the first time step is manually chosen. Then, with each time step, the length of the step is multiplied by a certain factor f_t , because planets usually change more quickly and strongly at the beginning of their lifetime than later. For the models presented in Chaps. 5 and 6, a starting time step of 1 Myr and a factor of $f_t = 1.005$ was chosen, leading to an evolution run of about 650 profiles for a time of $t = 5$ Gyr. The total number of points N in a model is not fixed. For the earlier models presented in Chap. 5, a constant number of about 1000 mass points was used for each model, based on the original guess solution calculated with MOGROP. For the more recent models in Chap. 6, an adaptive scheme is used. Whenever one of the main quantities y_i changes by more than $\Delta y_{\max} = 10^{-3}$ between neighbouring mass points ξ_j and ξ_{j+1} , an additional mass point is inserted in between the two. Conversely, if *all* y_i differ by less than 1×10^{-8} between two neighbouring points, one of the points is removed. This leads to mass grids of $N = 1500 \dots 2000$ for individual profiles.

In addition to the Henyey formalism described extensively in this section, OTTER also features a reduced version of that formalism that only solves Eqs. (3.10a) – (3.10c) for r , P , and T , while ignoring l . This is used for calculating the first profile in any evolution calculation, which has a defined temperature at the 1-bar-level $T_{1\text{bar}}$. Additionally, particular structure models with a defined outer temperature that are not part of a planetary evolution are also calculated with this formalism. This reduced version operates according to the same algorithm and equations as the full version, just with 3 instead of 4 equations and unknowns.



1

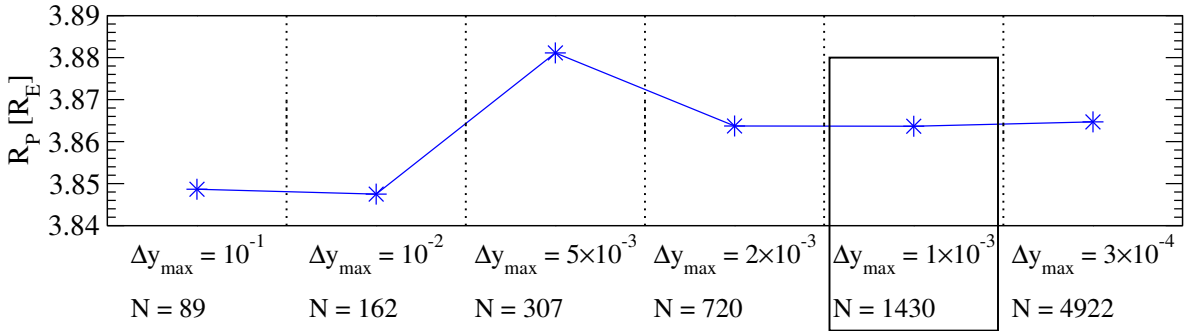


Fig. 3.3.: Radius of a Neptune model with a fixed $T_{1\text{bar}} = 72 \text{ K}$ for an adaptive mass grid with different values of Δy_{\max} and thus N . The model is the one designated "Neptune 2" in Sect. 5.1. Calculations were performed using the reduced Henyey formalism for r, P, T . The boxed conditions are used for the models in this work. See Sect. 3.3 for explanation.

3.4. Benchmarking the evolution calculations

3.4.1. Convergence with respect to time steps and mass points

To ensure that the evolution model is converged with regards to the length of the time steps, the evolution of an adiabatic Uranus model was calculated for different values of initial time step Δt and factor f_t . See section 5.1, specifically the model "Uranus 2", for more information on how the evolution was set up. The resulting cooling times τ , i.e. the time required to reach the observed effective temperature $T_{\text{eff}} = 59.1 \text{ K}$, are shown in Fig. 3.2. With a set of $\Delta t = 1 \text{ Myr}$ and $f_t = 1.005$, τ is converged to within 50 Myr compared to the most accurate test case, which is less than 1% of the cooling time.

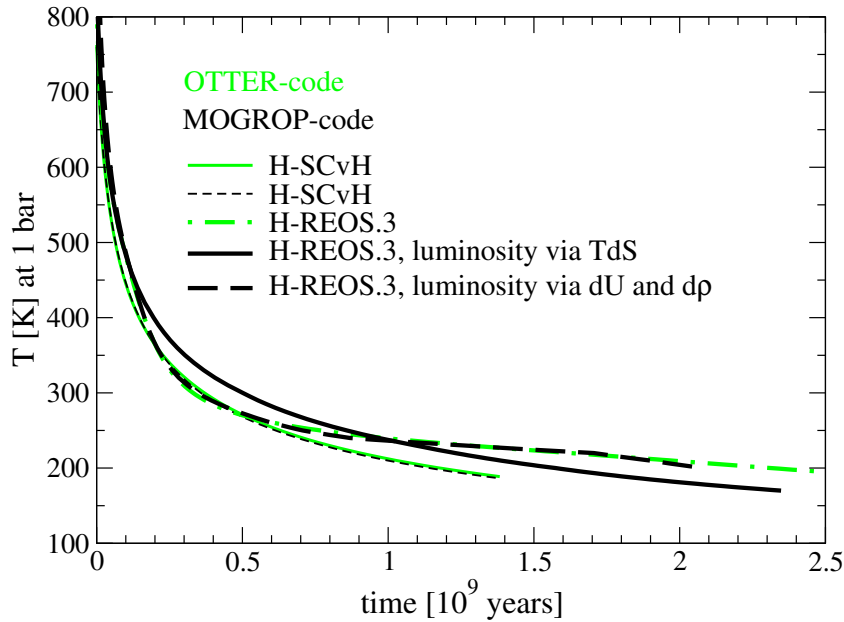


Fig. 3.4.: Evolution of a $300M_E$ planet with a $2M_E$ rock core and an adiabatic hydrogen envelope. Shown are comparisons between the OTTER code (green, this work) and the MOGROP code (black) based on Nettelmann *et al.* (2012) [104] for two different hydrogen equations of state –thin: SCvH-EOS [126]; thick: REOS.3 [7]– as well as different ways of calculating luminosity in case of MOGROP. Figure taken from [127], MOGROP curves courtesy of N. Nettelmann.

With regards to mass point number N , a Neptune model was calculated for different values of Δy_{\max} – see previous section for details – and the resulting radii are compared in Fig. 3.3. As can be seen, our chosen value of $\Delta y_{\max} = 1 \times 10^{-3}$ is well converged. The outer radius R_p differs from a model with more than 4 times the points by less than 0.5%.

3.4.2. Comparison with an established code

In order to verify the results given by the OTTER code, the evolution of a test planet with $M_p = 300M_E$ is calculated. A small rock core of $2 M_E$ is surrounded by a single, uniform, adiabatic hydrogen envelope. Planetary evolution tracks for this planet were calculated with OTTER as well as with MOGROP [103, 104]. These calculations were done with both the SCvH-EOS [126] and H-REOS.3 [7] (cf. Sect. 4.2.1) for hydrogen. The resulting evolutionary tracks can be seen in Fig. 3.4.

The evolution curves of both methods are very similar for the calculations using SCvH-EOS, showing the same curve shape and differing by only $\sim 1.2\%$ after 1.3 Gyr. However, for models using the H-REOS.3, the agreement is dependent on the method by

which the heat loss or luminosity profile is calculated. With MOGROP, the standard way of calculating an evolution is slightly different than presented here: a planet's adiabat is found by seeking out a (T, ρ) -path of constant entropy, where s is calculated via thermodynamic integrations from internal energy and density. Then, utilising the explicit entropy profiles, the heat loss from one profile to the next can be calculated with a variation of Eq. (2.15) directly. In our example case, this gives a strongly different evolution curve from the OTTER results, as shown by the dot-dashed green and solid black curves in Fig. 3.4. On the other hand, MOGROP also features the option to use partial derivatives of the EOS quantities for calculating the adiabat, as described e.g. by Ref. [97], and using Eq. (2.21) to calculate the time evolution. In this case, MOGROP produces results much closer to the OTTER curve, as seen with the black dashed curve. With this method, both curves show the same progression and their 1-bar-temperatures differ by only $\sim 2.4\%$ after 2 Gyr.

As described in Sect. 4.2.1, the SCvH-EOS is constructed from a thermodynamically consistent Helmholtz free energy model, and provides the adiabatic temperature gradient and the entropy directly. H-REOS.3, on the other hand, is constructed using data from several sources and not perfectly thermodynamically consistent over its whole range. This leads to uncertainties in the entropy in MOGROP, and therefore uncertainties in evolution models calculated with this method. Judging from the example shown here, it seems that the uncertainties in the heat loss might be much smaller when calculated from local derivatives of u and ρ directly, instead of utilising the entropy, which necessitates integrating over a large range of EOS-data.

To summarise, OTTER is able to reproduce results of the established code MOGROP, if in both cases the cooling equation is solved using local derivatives of the EOS data. It has also become clear that explicit knowledge of the entropy is not required to calculate homogeneous planetary evolution models. However, since the derivation of Eqs. (2.21) and (2.25) require a composition that is constant in time, these evolution calculations preclude models that include particle transport, e.g. by diffusion or convective mixing.

Chapter 4.

Materials and their properties in planetary modeling

4.1. The composition of Uranus and Neptune

Both Uranus and Neptune are located in the Solar System's outer reaches. Their orbital distance is beyond the boundary where water, methane, and ammonia – all thought to have been present in the protosolar cloud from which the Solar System formed – would have existed in solid form. Thus, these materials would have been able to form ice-rich pebbles or planetesimals, which could be easily accreted by the planets as they were forming. For this reason, both Uranus and Neptune are thought to contain significant amounts of oxygen, carbon, and nitrogen, usually in the form of planetary ices H_2O , CH_4 and NH_3 . These are collectively called *ice* – which should not be taken as a comment on their phase but simply material composition – whereas the heavier compound materials such as silicates or MgO are called *rocks*. Both of these groups are collectively referred to as *metals* or *heavy elements* in astrophysics, as are any materials with a molecular weight above that of helium.

In the absence of direct measurements of the planets' material composition, especially in the interior, the composition has to be inferred from secondary constraints, most notably structure models constructed to reproduce the available observables, such as mass, radius, and gravitational field. This can be done in one of two ways: one is to make assumptions on the components, take physical equations of state (EOSs) of the relevant materials and calculate models based on those by adjusting the composition to fit the observables, as was done by Podolak *et al.* (1995) [113] or Nettelmann *et al.* (2013) [105], for example. The other is to construct density profiles that result in the right gravitational field without assuming a composition first, and then to interpret

these profiles based on EOSs and the assumed thermal profile, see for example Marley *et al.* (1995) [93], Helled *et al.* (2011) [48], or Podolak *et al.* (2019) [114].

Models from both approaches have one characteristic in common: it seems to be impossible to satisfy the measured gravity field without any kind of increase in heavy-element content from the planet's outside to the interior, with the works of the first method generally focusing on models with sharp layer boundaries, while the second method models usually feature a more gradual composition increase. Beyond that commonality, there are a wide variety of possible structures found in the literature. For example, models have been calculated that consist of a mixture of rocks with H and He, without any ices [48, 52], as well as models with a high ice:rock ratio of 19 by mass [9]. It is also possible that one of the planets is rock-rich and the other ice-rich [50]. As explained by Helled & Fortney (2020) [50], even if we had perfect knowledge of a planet's mass, radius, shape, and gravity field, the solution space that fulfils these characteristics in terms of density profiles is non-unique. Additionally, assumptions about the planet's energy transfer mechanisms, and thus the model's temperature profile, influence the inferred compositions. If, as is quite possible, the temperature gradient within part of the planet is significantly higher than the adiabatic gradient, resulting in a comparatively hot interior, a higher amount of heavy elements as well as a lower ice:rock ratio is generally required to fulfil the observables [9, 102, 138]. Furthermore, there are uncertainties about material properties (discussed below) and mixing behaviour under planetary conditions. As an example, there is experimental evidence by Kraus *et al.* (2017) [74] and Kadobayashi *et al.* (2021) [67] of hydrocarbons under conditions typically predicted for adiabatic Uranus models separating into hydrogen and carbon, when the latter forms nano-diamonds. In a planet, the carbon would sink downward and might form an additional layer of deep carbon on top of the core.

The "traditional" structure assumed in many works (cf. Refs. [102, 105, 113]), which is also the simplest composition assumption to be consistent with the available gravity data, consists of a small rock core, surrounded by an inner envelope primarily composed of ice, surrounded by an outer envelope dominated by H and He. The composition is taken to be uniform in the layers with discontinuities at the boundaries. The reason for such a distinct layering might be de-mixing between H₂ and H₂O, as recently explored by Bailey & Stevenson [4], or a remnant of planet formation. This is the type of structure used in models calculated in this work. Heavy elements outside the core are represented either by pure water, or, if that is not sufficient to reproduce the observed bulk density, by a mixture of water and basalt. This is certainly a simpli-

fication, since former work showed that using $\text{NH}_3\text{-H}_2\text{O-CH}_4$ mixtures leads to a higher mass fraction of ice and thus to lower central temperatures than for pure water [9]. However, in light of the uncertainties in the planets' material composition, and given the fact that the purpose of this work is to examine trends rather than developing a definitive model for the ice giants, this should not heavily impact the conclusions of this work. The details of how this general structure is implemented in the different models can be found in Chaps. 5 and 6.

4.2. Equations of state

In general, theoretical equations of state for the warm dense matter found in planetary interiors fall into one of two broad categories:

In the *chemical picture* [73, 75], selected states of the material, such as H_2 , H , H^+ and e^- in the case of hydrogen, are considered as separate quasi-particle species. Their relative abundances are determined via chemical equilibria of the corresponding ionisation and dissociation reactions. Quasi-particle interactions are treated via effective pair potential functions that are based either on experiments or on *ab initio* methods (see below). However, this approximate treatment of many-body interactions breaks down for the higher densities found in the interior of planets, and thus chemical picture EOSs are usually inaccurate there [51].

On the other hand, in the *physical picture* [73, 75], electrons and nuclei are treated with quantum mechanical methods, and all bound or ionised states of the material are instead just long-lasting correlations between those. Because, ideally, these calculations are based only on physical laws and do not rely on a-priori assumptions about e.g. the bound states found in the system, they are referred to as *ab initio*. A prominent example of this approach is a combination of density functional theory (DFT) [58, 71, 96] for the electrons, and molecular dynamics (MD) [1] for the nuclei. In this framework, the Born-Oppenheimer approximation [10] is used to separate electronic and ionic motion. The electronic structure is solved self-consistently for a given ionic configuration, and then the ions are moved according to the forces exerted by the electrons and by other ions. This procedure is repeated for a given T and ρ until the equilibrium in the configuration of the nuclei is reached, and then the equilibrium state is simulated for several thousand time steps, which are the basis for extracting thermodynamic quantities via averaging over the time steps. In the DFT description of the electrons, the approach is not to solve the many-particle Schrodinger equation for

the electron wave functions directly. Instead, the electron density is used, and the system of interacting particles in an external potential is instead described as a reference system of non-interacting particles in a modified external potential that includes all the interaction effects between electrons. This approach is based on the work by Hohenberg & Kohn (1964) [58] and Kohn & Sham (1965) [71] for the zero-temperature case, modified by Mermin (1965) [96] for finite temperatures. It is, in principle, an exact description. However, the recast equations contain a term describing the exchange and correlation effects between the electrons, which is not known exactly and thus requires assumptions. Several approximations exist for this term, which is called the exchange-correlation (XC-) functional, and their choice can impact the results of DFT-MD simulations strongly [51]. There is not one best choice for all simulation scenarios, and their use has to be benchmarked with regards to what high-pressure experiments are available. Nevertheless, this approach is a potent tool to gain insight into material properties of warm dense matter and is more accurate for high pressures and temperatures than calculations using the chemical picture.

Another emerging form of *ab initio* EOS calculations is called Quantum Monte Carlo (QMC) [26]. In this approach, instead of formulating the many-particle-problem in terms of the electron density, as is done in DFT, the electron wave functions are calculated via a stochastic random sampling approach. This includes a direct description of the electron correlations, which makes it, in principle, more accurate than DFT. However, QMC is computationally highly expensive compared to DFT-MD calculations and can usually only be performed for smaller electron numbers, although it is well suited for multi-processor parallelisation. This makes it ideal for benchmarking DFT-MD calculations (e.g. Ref. [17]), but not (yet) well suited for wide-range calculation of EOS data [51, 95]. In the following, I will give an overview over the equations of state (EOS) used in models in this work. A more in-depth insight into the different data sets can be found in the original references cited there, as well as review articles such as by Helled *et al.* [51] for hydrogen and helium.

4.2.1. Hydrogen and helium

One of the most widely used equations of state for H and He is the one by Saumon *et al.* (1995) [126], called **SCvH-EOS** hereafter. It covers a space of $2.1 < \lg(T/\text{K}) < 7.06$ and $-6 < \lg(P/\text{GPa}) < 9$ and gives values for density ρ , specific entropy s , specific internal energy u , mass fractions of molecular and atomic hydrogen X_{H_2} , X_{H} – or

of atomic and ionised helium X_{He} , X_{He^+} for the He-EOS – as well as the derivatives $\left(\frac{\partial \rho}{\partial T}\right)_P$, $\left(\frac{\partial \rho}{\partial P}\right)_T$, $\left(\frac{\partial s}{\partial T}\right)_P$, $\left(\frac{\partial s}{\partial P}\right)_T$, and the adiabatic temperature gradient ∇_{ad} , each as a function of P, T . The data are calculated using the chemical picture, where interparticle effects are included via effective pair potential functions that are benchmarked against experimental results, where available. The state of chemical equilibrium is obtained by minimising the Helmholtz free energy $F(V, T, \{N_i\})$, and then P and s are calculated via differentiation of F and all other quantities from there. The resulting data set has the advantage of not only being thermodynamically consistent, but also providing the important quantities of s and ∇_{ad} directly. On the other hand, as mentioned in the preceding section, chemical picture EOSs are somewhat inaccurate under the conditions in the deep interior of planets compared to *ab initio* EOSs.

A set of EOS used in most of the models presented in this work is version 3 of the Rostock Equation of State for hydrogen and helium, referred to as **REOS.3** hereafter. That version was published by Becker *et al.* (2014) [7] and covers a range of $60 \text{ K} < T < 10^7 \text{ K}$ and $10^{-10} \text{ g cm}^{-3} < \rho < 10^3 \text{ g cm}^{-3}$. The data sets are composed of different sources of EOS data for different thermodynamic conditions. The area of $\rho > 10^{-1} \text{ g cm}^{-3}$ and $T \lesssim 10^6 \text{ K}$ in for He, and $10^{-1} \text{ g cm}^{-3} \rho < 10^2 \text{ g cm}^{-3}$ and $T < 10^5 \text{ K}$ for H, is made up of data calculated via DFT-MD directly for that publication. In the case of hydrogen, the low-density, low-temperature data is supplied by the generalised fluid variational theory EOS (FVT-EOS) published by Holst *et al.* (2007) [60], which is a chemical model, and for $1000 \text{ K} < T < 10\,000 \text{ K}$, the aforementioned SCvH-EOS. In the high-temperature and high-density range, where hydrogen can be expected to be fully ionised, a plasma-EOS by Chabrier & Potekhin (1998) [15] is used. In the case of helium, the *ab initio* data is supplemented by SCvH-EOS for high temperatures, as well as a virial expansion EOS for the low- ρ , low- T -regime. The resulting data cover a wide range of temperatures and densities encountered in planetary models. While they lack the inherent thermodynamic consistency found in the SCvH-EOS, the *ab initio* calculations ensure that it is more accurate in the deep interior of the planets.

Recently, another wide-range H/He-EOS was released by Chabrier *et al.* (2019) [14]. This new table, which will be called **CMS19-EOS** hereafter, features the Chabrier-Potekhin EOS for high temperatures and high densities, and SCvH data in the low- T , low- ρ limit, where H and He are either molecular or atomic. For conditions of $5 \times 10^{-2} \text{ g cm}^{-3} < \rho < 10^1 \text{ g cm}^{-3}$ and $T < 10^5 \text{ K}$ for hydrogen, or $10^{-1} \text{ g cm}^{-3} < \rho < 10^1 \text{ g cm}^{-3}$ and $T < 10^6 \text{ K}$ for helium, various *ab initio* data sets were utilised. Like the SCvH data, this EOS provides the entropy and adiabatic temperature gradient explicitly.

4.2.2. Heavy elements

Water

In this work, two particular EOS data sets are used for water:

The SESAME 7150 EOS for water, hereafter called **Ses7150-EOS**, from the SESAME database 1992 [90], was constructed by Ree (1976) [121]. It covers the range of $2 \times 10^{-6} \text{ g cm}^{-3} < \rho < 400 \text{ g cm}^{-3}$ and $290 \text{ K} < T < 1.74 \times 10^8 \text{ K}$. It combines experimental results in the area of $\rho < 1 \text{ g cm}^{-3}$ and $T \lesssim 1000 \text{ K}$ with various theoretical chemical picture calculations in the high- T and high- ρ regions.

A more up-to-date EOS for water is the one by Mazevet *et al.* (2019) [94], hereafter called **MLCP19-EOS**. It comprises data from several sources in different ρ - T regions and fits a parameterisation of the Helmholtz free energy on this, resulting in a thermodynamically consistent EOS over a wide range of conditions, up to about $5 \times 10^4 \text{ K}$ and 100 g cm^{-3} . The EOS is primarily based on *ab initio* calculations obtained via DFT-MD, supplemented with further *ab initio* data from French *et al.* (2009) [32]. For $\rho > 50 \text{ g cm}^{-3}$, a simplified calculations using Thomas-Fermi Molecular Dynamics is employed, and for $\rho < 1 \text{ g cm}^{-3}$ and $T < 1000 \text{ K}$, the EOS by Wagner & Pruß (2002) [139] is used, which is a Helmholtz free energy fit to experimental data in this region.

Both the Ses7150-EOS and the MLCP19-EOS feature the liquid-vapour phase transition in the low- T region, which manifests as a region of constant pressure over a range of densities. In the Ses7150-EOS, this is part of the original data, while for the MLCP19-EOS, this was the result of a Maxwell construction performed by Martin French, which he kindly provided to me. However, because typical planetary adiabats for Uranus and Neptune pass right through this region and the rather abrupt isobaric region caused an overshooting in the spline interpolation employed in my program, I use an ideal gas EOS for water calculated by Nadine Nettelmann for temperatures $T < 800 \text{ K}$ for both of these EOSs, where the internal energy contains contributions from vibrational and rotational energy states of H_2O , based on rigid rotor and harmonic oscillator models from Ref. [36].

Rocks

For both the small central core of these models as well as the inner envelope in some of the models presented in Chap. 6 that are particularly hot in the deep interior, a ma-

terial of higher density than water is needed for the metals to reproduce the observed planetary radius. One example of an EOS for this kind of rock material is the one by Cebulla & Redmer (2014) [13] for MgO. It was calculated via DFT-MD simulations and agrees with data from compression experiments, where such are available. However, for high temperatures it covers only pressures of more than ca. 50 GPa, which makes its $P - T$ range smaller than the one needed for the inner envelope regions of the models in this work.

Therefore, in an effort to use a consistent rock EOS in all planetary regions, the models calculated here use the SESAME 7530 EOS (basalt) [90] for all rocky material. This EOS, from the report by Barnes & Lyon (1988) [5], represents a mixture of various oxides. The three most abundant by mass of these are SiO_2 , Al_2O_3 , and CaO , and is based on experimental shock data for the materials, which were then weighted according to their abundances. This EOS was used here because it provides a description of rocky material over a wide range of temperatures and densities. This use follows the example of Nettelmann *et al.* (2016) [102], who also used this description of basalt to obtain a rock-ice mixture in the inner envelope of Uranus. Recently, Kim *et al.* (2021) [68] found experimental evidence for the solubility of MgO and H_2O at conditions similar to the beginning of the metal-rich deep envelope in three-layer ice giant models, lending credence to using a mixtures of water and rocks in this region.

4.2.3. Linear mixing

The EOSs for the different materials are combined using the additive volume law. For a system of N components, the specific internal energy and density of the mixture are calculated as

$$u(P, T) = \sum_{i=1}^N X_i u_i(P, T), \quad (4.1)$$

$$\frac{1}{\rho(P, T)} = \sum_{i=1}^N \frac{X_i}{\rho_i(P, T)}, \quad (4.2)$$

where X_i are the mass fractions of the individual components. Using this treatment for planetary models goes back to early Jupiter and Saturn models calculated by DeMarcus (1958) [19] and Peebles (1964) [111], and has become standard practice in planet modelling. In 2013, Wang *et al.* [141] compared QMD simulations of H-He-mixtures

with results obtained via different mixing rules and found overall good agreement with linear mixing at constant pressure, as discussed here. Similarly, Bethkenhagen *et al.* (2017) [9] performed DFT-MD simulations mixtures of water, methane, and ammonia and found that the linear mixing rule differed by less than 4% in ρ and 4 kJ g^{-1} in u for binary mixtures, with lower deviations for the ternary mixtures of all three materials in solar proportions. These rather good agreements as well as the convenience of using the linear mixing rule justify the use of this procedure in our models, especially considering the alternative would be to use full mixture EOSs for a variety of relative abundances, which, barring some specific cases, do not exist and would be prohibitively computationally costly to calculate.

4.3. Thermal conductivity

A key quantity for modelling the interior of the planets is the thermal conductivity λ , particularly in regions that are not vigorously convecting and are therefore not adiabatic. However, finding widely applicable and reliable values for λ under the conditions in the interior of ice giants is very difficult, because there have not been many experiments or *ab initio* calculations supplying λ there.

For pure water, thermal conductivity values have been calculated via DFT-MD simulations in a wide range of conditions, covering densities of $0.1 - 10 \text{ g cm}^{-3}$ and temperatures of $1000 - 50\,000 \text{ K}$. The contributions of the electrons were presented by French & Redmer (2017) [35], and the ionic part by French (2019) [29]. It is shown there that the values produced by this method are consistent with measurements for 385 K and 1.1 g cm^{-3} as well as experiments for the ice VII phase in the high-pressure, room-temperature regime. These combined λ values from Refs. [35] and [29] will be referred to as $\lambda_{\text{H}_2\text{O}}$ from now on. Grasselli *et al.* (2020) [42] also calculated λ for H_2O from *ab initio* methods for five (ρ, T) -points in total. They are of the same order as the French-data [29, 35], but consistently larger for reasons not readily known. According to French [29], ionic heat conduction is stronger in water for $T \lesssim 6 \times 10^3 \text{ K}$, while for $T \gtrsim 10^4 \text{ K}$ and $\rho \gtrsim 2 \text{ g cm}^{-3}$ the electronic part becomes dominant. These are conditions routinely found in models of Uranus and Neptune, especially at a young age or in the presence of a strong superadiabatic temperature gradient, indicating that a model focusing purely on the ions would not be valid for modelling the ice giants.

The electronic contribution to the thermal and electrical conductivities of hydrogen were calculated by Holst *et al.* (2011) in a wide range of densities ($0.1 - 5 \text{ g cm}^{-3}$) and

temperatures (1000 - 50 000 K) using DFT-MD calculations [59]. Additionally, French *et al.* (2012) [30] calculated both of these quantities, including the ionic contribution for λ , for a mixture of hydrogen and helium in solar proportions of $X_{\text{He}} = 0.275$ along an adiabatic Jupiter profile. They found the ionic contribution to be relevant for temperatures less than about 5000 K for λ . For larger temperatures, where hydrogen is ionised, λ_{H} according to Ref. [59] is larger than $\lambda_{\text{H}_2\text{O}}$ by Refs. [29, 35]. The addition of helium to a mixture under these conditions would probably lower the overall λ somewhat because He is not ionised for $T \lesssim 20 \times 10^3$ K even at $P = 1000$ GPa [116], but the λ values calculated by French *et al.* (2012) [30] for a H-He mixture along a Jupiter adiabat are still larger than those of pure water for the same (ρ, T) conditions. Unfortunately, for planetary ices other than water, there are, to the best of my knowledge, no values for λ in the warm dense conditions of the deep interior of planets available. Thus, the best we can do for these is to estimate how the conductivities of an ice mixture might behave in relation to pure water, based on the *Wiedemann-Franz law*. This relation states that in a highly degenerate electron gas, λ is proportionate to the electrical DC conductivity σ for constant temperature [87, 144] with

$$\frac{\lambda}{\sigma} = \frac{k_{\text{B}}^2}{e^2} \Lambda_{\text{L}} T, \quad (4.3)$$

where k_{B} is the Boltzmann constant, e the elementary charge, and Λ_{L} the *Lorenz number*. Such highly degenerate conditions are not to be expected in the warm dense matter regime of planetary interiors [28], but the Wiedemann-Franz law might give a rough idea how λ might change due to the addition of planetary ices other than water. For ammonia, Ravasio *et al.* (2021) [119] have calculated σ along the Hugoniot curve using DFT-MD. They find for pressures larger than about 50 GPa – corresponding to about 1.7 g cm^{-3} according to their shock wave experiments – that the ammonia conductivities are substantially larger than the water values by French *et al.* (2010) [33] along the water Hugoniot. This could indicate that a $\text{H}_2\text{O-NH}_3$ mixture would have a higher λ than pure water for high pressures and temperatures.

Chau *et al.* (2011) [16] have measured σ for a *synthetic Uranus mixture* – a H-C-N-O mixture in roughly solar proportions – at pressures between 74 and 190 GPa and temperatures between 4300 and 8400 K and found them to be about half of the water values at similar pressures measured by Chau *et al.* (2001). This might mean that λ of an ice mixture is lower than $\lambda_{\text{H}_2\text{O}}$ by about the same factor for these high pressures and temperatures, if the Wiedemann-Franz law can be applied.

Again, these are only rough estimates of the trends, especially because in the most im-

portant region for λ in our models, around the transition from the outer to the inner envelope at $P \approx 10 \dots 30$ GPa and $T \approx 2000 \dots 10\,000$ K (with $\rho \approx 0.3 \dots 1.4$ g cm⁻³), various materials are only partially ionised, and therefore Eq. (4.3) is not valid there. So, we have seen that there are considerable uncertainties, not both in the conductivity data discussed here and in the material composition of Uranus and Neptune, as discussed in Sect. 4.1. Given that, as well as the fact that the models in this work use an EOS of water as a proxy for the unknown complex mixture of H-C-N-O materials expected in the deep interior of these planets, this work will also use the $\lambda_{\text{H}_2\text{O}}$ values of French [29] and French & Redmer [35] for the conductive regions of the models presented here. Because our estimates point towards the thermal conductivity of the real mixture being higher than for pure water, $\lambda_{\text{H}_2\text{O}}$ be treated as an approximate lower bound to the real λ . When presenting non-adiabatic models in Chap. 6, there will be a discussion on the influence a higher λ has on the models.

It becomes clear that even though our understanding of heat transport properties of planetary ices under warm dense matter conditions has improved considerably in recent years, there is still a need for further wide-range material data at extreme conditions as provided for water by DFT-MD calculations, and experimental verification thereof.

Chapter 5.

Adiabatic evolution of Uranus and Neptune

As a first application of the OTTER code, let us calculate a number of what might be called “traditional” evolution models for Uranus and Neptune, which are assumed to be convective and therefore fully adiabatic in the interior. This will allow us to systematically test the influence of solar energy influx and different EOS data on the resulting cooling times. The majority of the work in this chapter has been published in Scheibe *et al.* (2019) [127], hereafter referred to as Paper I.

Model name	H/He-EOS	H ₂ O-EOS	Z_1	Z_2	m_{12} [M_E]	m_{core} [M_E]	$m_{\text{H/He}}$ [M_E]	J_2 $\times 10^2$	J_4 $\times 10^4$
Uranus 1	REOS.3	Ses7150	0.261	0.941	12.5	0.25	2.2	0.28424	-0.2560
Uranus 2	REOS.3	MLCP19	0.273	0.96	12.44	0.79	2.0	0.29157	-0.2711
Neptune 1	REOS.3	Ses7150	0.42	0.91	15.0	1.06	2.4	0.33192	-0.3175
Neptune 2	REOS.3	MLCP19	0.42	0.929	15.17	1.04	2.2	0.35212	-0.3466
Neptune 3	CMS19	MLCP19	0.424	0.92	15.17	1.05	2.3	0.35312	-0.3480

Tab. 5.1.: Parameters for the adiabatic Uranus and Neptune models. Shown are H/He-EOS and water-EOS (see Sect. 4.2 for details), outer envelope water content Z_1 , inner envelope water content Z_2 , mass coordinate for transition between outer and inner fluid envelope m_{12} , and core mass m_{core} . Additionally, there are resulting model properties: combined mass of H and He $m_{\text{H/He}}$ and gravitational moments J_2, J_4 calculated using MOGROP [104] according to the 1 bar surface level. Reference values for the latter can be found in App. A.

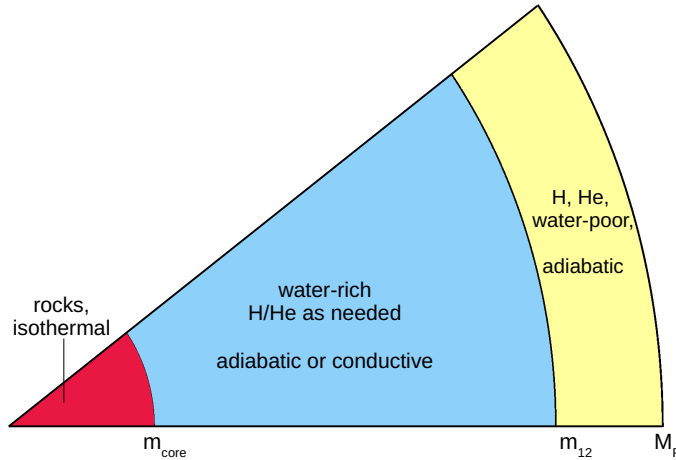


Fig. 5.1.: Outline of the assumed structure for the adiabatic models considered in this chapter and Paper I: isothermal rock core of mass m_{core} , surrounded by a water-rich inner envelope, surrounded by a H/He-rich outer envelope. Both envelopes are convecting and therefore adiabatic, with an isothermal core. m_{12} marks the transition between the envelopes.

5.1. Parameters and model assumptions

The models calculated here follow the standard 3-layer approach (see Sect. 4.1). The envelope is separated into a H/He-rich outer envelope with water representing heavy elements, and a water-rich inner envelope with only a small amount of H/He. The centre is made up of a small rocky core. Both envelopes are assumed to be strongly convecting, which, as was discussed in Sect. 2.2.3, can reasonably be described with an adiabatic temperature gradient. The core is assumed to be isothermal. Note that these models have a discontinuity in composition at the layer boundaries. Both Uranus and Neptune models were calculated with water described by the Ses7150-EOS and by the MLCP19-EOS (see Sect. 4.2.2 for details). An overview of the models and the parameters used for them can be found in Tab. 5.1. They were chosen roughly based on previously published models [105] in order to reproduce the present-day radius. The models featuring Ses7150-EOS for water (Uranus 1, Neptune 1) will be referred to as Ses7150-models collectively, the models with MLCP19-EOS (Uranus 2, Neptune 2, Neptune 3) as MLCP19-models.

The total mass of H and He for these models, which is presented in Tab. 5.1, falls into the range of published models able to reproduce the gravitational moments [52]. However, 3-layer models by Nettelmann *et al.* (2013) [105] feature a layer transition further outside than in these models, especially for Uranus, so that those are less cent-

rally condensed. As a consequence, the gravitational moments J_2 , J_4 of the models, which are also given in Tab. 5.1, are lower than the measured values by about 20% for Uranus and 5% for Neptune, except for the model Neptune 3. Uranus is especially sensitive to small changes in the parameters, due to it being so close to solar equilibrium – a point discussed in more detail in Sect. 5.2 – and therefore this deviation could mean that the cooling times presented here for Uranus might be shifted by up to 1 Gyr. However, as the main purpose of this chapter is to study systematic trends with various parameters, those overall conclusions are likely not affected.

To study the influence of solar irradiation, three different methods are used, based on Eq. (3.7) in Sect. 3: in the first, solar irradiation is treated as non-existent, by setting $T_{\text{eq}} = 0$. In the second, T_{eq} is calculated according to today's solar parameters and kept constant on this value for the entire evolution. In the third, T_{eq} changes with time. Here, the solar luminosity L_* is assumed to be linearly growing with time, from a value of $0.7 L_{*,\text{present}}$ at $t = 0$, based on a solar evolution model by Sackmann *et al.* (1993) [124]. In this last instance, Uranus' cooling times proved to be longer than the age of the solar system. To ensure that the planet was able to reach its observed temperature despite the rising T_{eq} , the evolution tracks for the Uranus models were set to begin at $t = -1.1$ Gyr instead of $t = 0$. This means that they usually reach their observed T_{eff} at times $t < 4.56$ Gyr, where $T_{\text{eq}} < T_{\text{eq,observed}}$. Thus, the cooling is slightly accelerated and the resulting adiabatic ages for Uranus should be taken as a lower bound.

Regardless of the model used, all the evolution curves presented in the figures of this chapter were shifted to match their planet's observed T_{eff} at $t = 4.56$ Gyr after the calculation was finished. This allows for a quick comparison of resulting cooling times at first glance.

5.2. Influence of solar irradiation

This work considers three cases of $T_{\text{eq}} = 0$, $T_{\text{eq}} = \text{const.}$, and $T_{\text{eq}} = T_{\text{eq}}(t)$ for each evolution model, which are shown in Fig. 5.2. Despite the fact that Uranus and Neptune orbit far out in the solar system, at 19 AU and 30 AU, respectively, we see a noticeable impact from solar irradiation on the evolution behaviour. Entirely neglecting it gives much shorter cooling times than the other cases. Interestingly, in this case Uranus actually cools more quickly than Neptune. On the other hand, when fixing the irradiation over the whole lifetime, we get much longer cooling times than in the more

nuanced third case of $T_{\text{eq}}(t)$. The surface luminosity acts as a cap on how quickly the planet can cool, and if the difference between intrinsic luminosity and solar irradiation is smaller, this slows down cooling considerably.

This also explains why we see a much more pronounced effect of these three treatments on Uranus than on Neptune. While having the irradiation change with time shortens Neptune's cooling times by about 0.1 Gyr, it does so for Uranus by several Gyr. The reason is that Uranus' $T_{\text{eff}} = 59.1$ K is very close to its $T_{\text{eq}} = 58.1$ K, compared to Neptune ($T_{\text{eff}} = 59.3$ K, $T_{\text{eq}} = 46.4$ K). Since cooling speed depends on the difference between those two, the slope of the evolution curve becomes very shallow as equilibrium is approached. This means that small changes in how that equilibrium is handled affect Uranus more strongly than Neptune. The same is true for small differences in other assumptions, such as the radial distribution of heavy elements.

This can also be seen when varying the planetary Bond albedo. Fig. 5.3 shows cooling times for Neptune and Uranus models for different values of A . Higher albedo means less energy absorbed by the planet and thus a lower T_{eq} as per Eq. (3.8), and therefore leads to lower cooling times. As has already been discussed for Fig. 5.2, the influence on Uranus' evolution is more conspicuous than on Neptune's and an albedo of ~ 0.4 could bring Uranus' cooling time down to the age of the solar system. For Neptune, however, all considered values of A lead to a cooling time that is too short.

5.3. Influence of different equations of state

Let us now consider the influence of different EOSs on these adiabatic evolution models. Fig. 5.4 shows evolution curves for different Neptune models calculated with hydrogen and helium described by either REOS version 1, REOS version 3, or CMS19-EOS, as well as with different planetary evolution codes (see Sect. 4.2.1 for details). It becomes clear that the models using REOS.3 data produce a quicker cooling than the reference model using REOS.1; the cooling time shortens by at least 0.7 Gyr. While the cooling time clearly also varies depending on the code used and on the water EOS, the shorter age is visible with both MOGROP and OTTER and thus seems to be caused by the different H/He-EOS. A further shortening occurs when using the CMS19-EOS for H/He, which again serves as a reminder not to underestimate the importance of H and He for the cooling behaviour despite its low overall mass abundance.

The other main material of interest in these models is water. The models were cal-

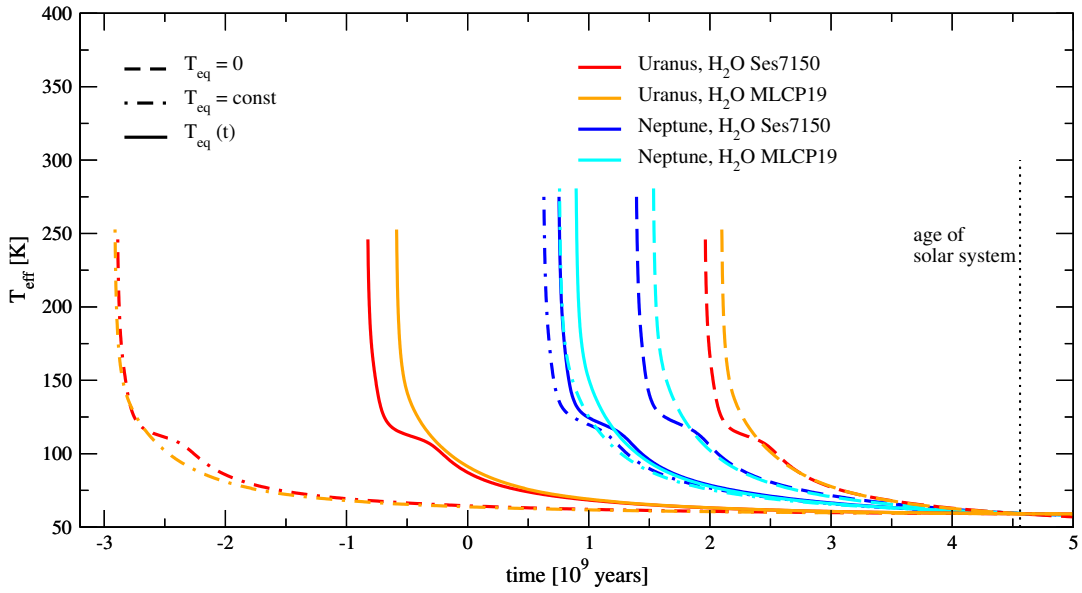


Fig. 5.2.: Thermal evolution of Uranus (red and orange) and Neptune (blue and cyan) for $A = 0.3$ and for different assumed incident flux descriptions. Dashed lines represent no solar influx, dot-dashed constant solar irradiation and solid lines linearly changing solar luminosity (see Sect. 5.2). Cooling curves are shown for two different equations of state for the water in the envelope. Ses7150-EOS and MLCP19-EOS. Figure adapted from Paper I.

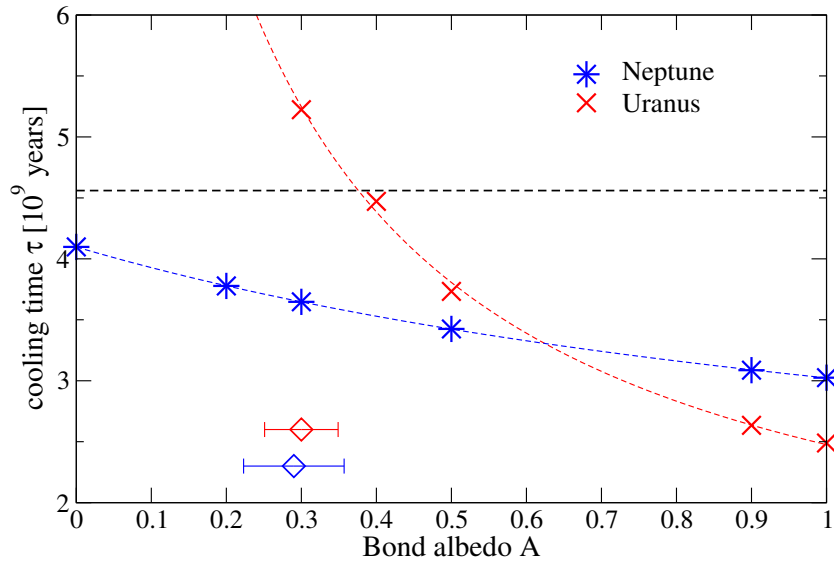


Fig. 5.3.: Cooling times of Uranus and Neptune for different Bond albedo values. Models use the composition of Uranus 2 and Neptune 2 models, respectively, in Tab. 5.1 and solar irradiation is treated as $T_{\text{eq}}(t)$. Diamonds show observed Voyager values of A and their uncertainties [109, 110]. The thin dashed lines are hyperbolic curve fits and serve as a guide to the eye. The figure shows that the albedo has a strong influence on the cooling time of Uranus specifically, but that its 1σ -uncertainty is insufficient to explain the luminosity of both planets. Figure adapted from Paper I.

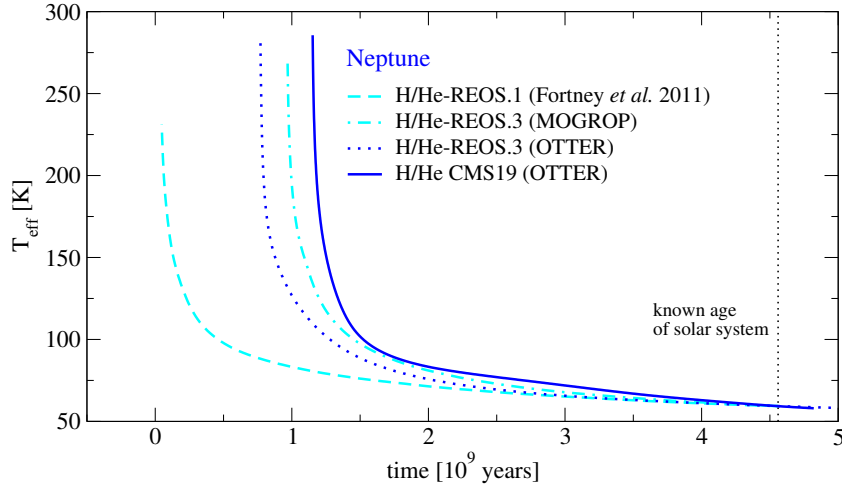


Fig. 5.4.: Evolution calculations for Neptune using different H/He EOS data and codes. Dashed: H/He-REOS.1, MOGROP adapted from [24], dash-dotted: H/He-REOS.3, MOGROP, dotted: H/He-REOS.3, OTTER, solid: H/He-CMS19, OTTER. All curves use $T_{\text{eq}} = \text{const.}$ (see sect. 5.2). MOGROP models use H_2O -REOS (cf. [106]), OTTER models use MLCP19-EOS. Figure adapted from Paper I.

culated with both Ses7150-EOS and MLCP19-EOS. The resulting deep interior $P - T$ profiles are shown in Fig. 5.5. While the MLCP19-profiles are colder in most of the inner envelope, as is usual for models with higher ice content [9], the core temperature is only weakly affected by the choice of water EOS, about 5700 K for Uranus and 5500 K for Neptune. In Fig. 5.2, we can see the effect of the difference in H_2O -EOS on the cooling times for different irradiation scenarios. In all cases, MLCP19-models produce about 5% shorter cooling times than Ses7150-models. The latter also feature an edge at $T_{\text{eff}} \sim 120$ K where cooling is temporarily slowed. This behaviour can possibly be traced to the deep interior at about 100 GPa and 5000 – 7000 K, see Fig. 5.6. While the MLCP19-profiles run roughly parallel for pressures over ca. 50 GPa, the Ses7150-profiles begin to develop a bend in their curve shape at about 100 GPa, meaning an accelerated cooling of the deep interior, leading to a stronger release of energy and thus slowdown of surface cooling. However, the impact of the water-EOS on the cooling curve, while noticeable, is smaller than the other influences explored in this chapter.

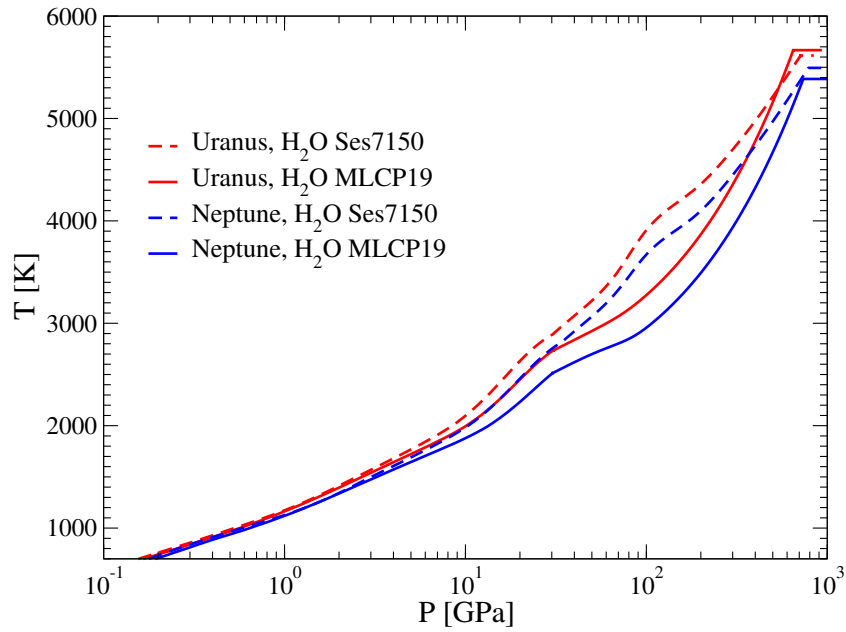


Fig. 5.5.: Deep interior of Uranus (red) and Neptune (blue) with the heavy elements in the envelope treated via the Ses7150-EOS (dashed) or the MLCP19-EOS (solid), respectively. Figure adapted from Paper I.

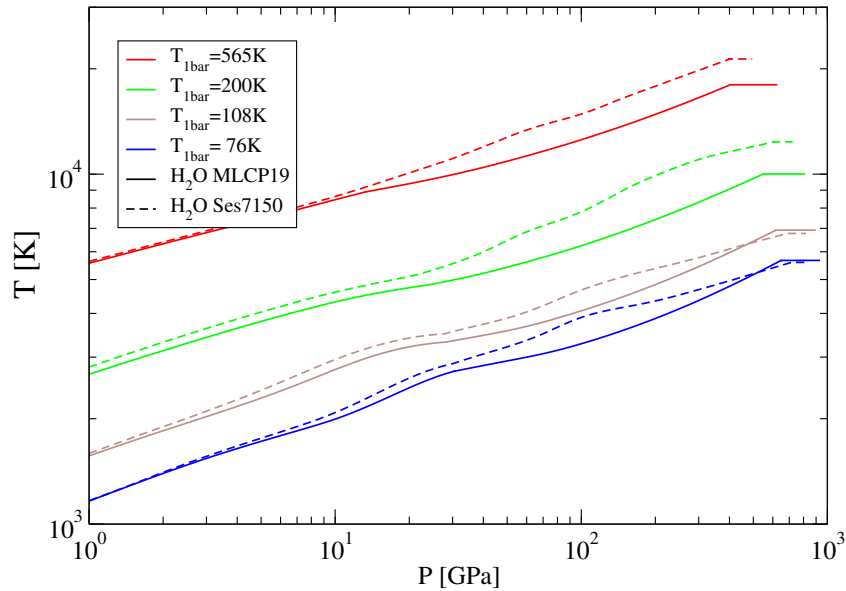


Fig. 5.6.: Planetary adiabats for Uranus models with different outer temperatures, representing different stages in the evolution. Dashed are models using Ses7150-EOS, solid models with MLCP19-EOS for water. Notably, Ses7150-models exhibit a flattening at ca. 100 GPa for $T \lesssim 6000$ K not seen in MLCP19-models.

5.4. Discussion of adiabatic models

The preferred models here for Uranus and Neptune, using H/He-REOS.3 and MLCP19-EOS for water as well as a linearly rising solar luminosity, result in cooling times of about $\tau_U = 5.1$ Gyr for Uranus and $\tau_N = 3.7$ Gyr for Neptune. These, as well as the other cooling times from models in this section, are noticeably shorter than previous calculations, e.g. by Fortney *et al.* (2011) [24] or Nettelmann *et al.* (2013) [105], who find ages of 9 – 10 Gyr for Uranus and 4.3 – 4.8 Gyr for Neptune. Several factors contribute to this discrepancy: first, let us keep in mind that these publications treat T_{eq} as constant, so the most appropriate comparison would be the second case from Sect. 5.2, which gives the longest cooling times, albeit still shorter than the literature. Second, the models presented here use different EOS data, particularly for H and He. Both Fortney *et al.* [24] and Nettelmann *et al.* [105] use Version 1 of the H/He-REOS, while these models use version 3, which can lead to a significant shortening, as shown in Sect. 5.3. Third, as discussed in Sect. 3.4, different methods of calculating the heat loss rate lead to different evolution curves when not using entirely thermodynamically consistent EOS data. And last, as mentioned in Sect. 5.1, there is probably a rather large uncertainty associated with the Uranus cooling times of this chapter because their gravitational moments deviate noticeably from the observed values. Nevertheless, it is clear from these results here that there is a strong difference in adiabatic cooling behaviour for Uranus and Neptune. They cannot both be explained by an adiabatic interior unless different assumptions are made, and the results confirm previous conclusions, that models beyond the pure adiabatic interior are needed to bring the ice giants into agreement with the observations [24, 64, 105, 112]. Additionally, the shorter cooling times for Neptune serve to shed doubt on the usual framing that Neptune’s luminosity is consistent with adiabatic evolution, while attempts to go beyond simple adiabatic models have so far usually focused on Uranus.

Furthermore, solar irradiation has a pronounced influence on the planetary evolution, particularly once the planet nears thermal equilibrium. This effect is larger for Uranus than for Neptune but cannot be discounted for either of them. The observational uncertainties of T_{eff} introduce an error of about 0.5 Gyr for Uranus and 0.3 Gyr for Neptune. Additionally, the measured Bond albedos of Uranus and Neptune, and thus their T_{eq} -values, have relatively large observational uncertainties, which might even be larger than previously thought: in 2018, Li *et al.* [82] re-evaluated Jupiter’s Bond albedo based on more recent measurements from the Cassini mission and found it to be at 0.503, significantly higher than the previously accepted Voyager value of 0.343.

Thus, improving the observational constraints on the existing measurements of A and T_{eff} , while not sufficient on their own, is vital to help constrain interior evolution scenarios.

Chapter 6.

Ice giant evolution in the presence of a deep internal thermal boundary layer

As was shown in Chap. 5, adiabatic evolution models fail to reproduce the measured present-day luminosities of both Uranus and Neptune, and they also give quite different results for both planets. There are several possible explanations for this behaviour, an overview of which was given in the introduction to this work. Here we want to investigate the possibility of a thin, thermally conducting interface between the ice-rich interior and the H/He-rich exterior of the planet, which we shall call a *thermal boundary layer*, or TBL for short.

This idea, presented for the ice giants by e.g. Podolak *et al.* (1991) [112] or Hubbard *et al.* (1995) [64], is based upon the possibility of a compositional gradient stabilising an area of the planet against convection. This would impede heat transfer from the deep interior to the surface and cause a large amount of primordial heat to still be trapped inside, potentially shortening the cooling time of the surface or outer areas. The reason for such a gradient in composition might be a result of the formation process or, alternatively, of a more recent sedimentation process through, e.g., H₂-H₂O demixing. Nettelmann *et al.* (2016) [102] investigated this idea for ice giants by assuming a steep temperature gradient between outer and inner envelope, whose evolution was described by ad-hoc functions designed so that the temperature difference grows with time, which was shown to reproduce Uranus' measured luminosity. Recently, Vazan & Helled (2020) [138] showed that the inhibited heat flow due to stably stratification as a result of primordial composition gradients could indeed survive for timescales of planetary evolution and were sufficient to reproduce Uranus' low luminosity. Leconte & Chabrier (2013) [80] performed evolution calculations for Saturn, whose age had been consistently underestimated by adiabatic models, and found that an area of in-

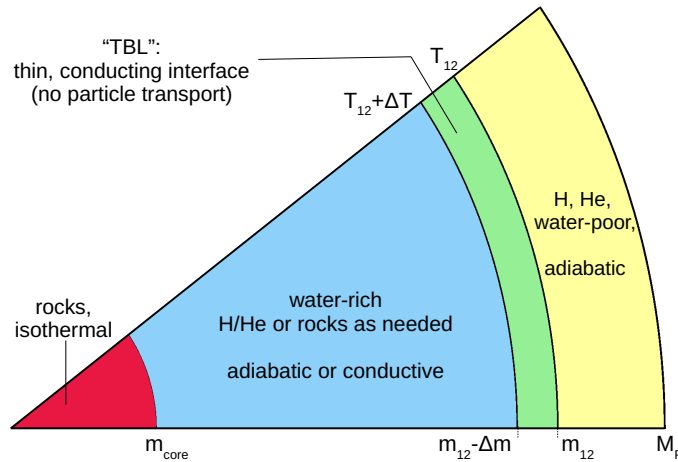


Fig. 6.1.: Outline of the assumed structure for the TBL models: isothermal rock core of mass m_{core} , surrounded by a heavy-element-rich inner envelope, surrounded by a H/He-rich outer envelope. There is a conducting TBL of fixed thickness Δm between inner and outer envelope, leading to a temperature difference of ΔT .

hibited heat transfer due to layered convection – see Sect. 2.2.3 – could actually slow down the cooling time of the planet’s outer layers and thus bring Saturn models in line with the observed luminosity. Likewise, it was shown by Helled *et al.* (2020) [52], that taking the ad-hoc functional description of a TBL from Nettelmann *et al.* [102] but allowing for the temperature difference from outer to inner envelope to decay during the planet’s life, can possibly produce higher present-day luminosities than in the adiabatic case and might thus help explain the brightness of Neptune. Therefore, it is worthwhile to examine the effects of a stably-stratified TBL inhibiting heat transfer in the planet interior for both Uranus, whose age is overestimated by adiabatic models, and Neptune, whose age is underestimated, see Chap. 5.

The results presented here have been published in Ref. [128], hereafter referred to as Paper II.

6.1. Model assumptions

The assumed structure of our models is illustrated in Fig. 6.1. Similarly to Nettelmann *et al.* [102], we assume a three-layer model structure like the one discussed in Chap. 5, with an isothermal rock core surrounded by an inner envelope composed of heavy elements, in turn surrounded by an outer envelope of H, He, and H_2O . Both envelopes are, at least initially, considered to be strongly convecting and therefore adiabatic and

homogeneously mixed. However, in contrast to the setup chosen in Chap. 5, there is a thin interface between the two envelopes - the thermal boundary layer or TBL - where heat transport is inhibited due to the compositional gradient. In the TBL, the temperature gradient follows the conductive description laid out in Sect. 2.2.2, with ∇_T given by Eq. (2.39). Within the TBL, the composition is set to a linear progression of the mass fractions X_i with regard to mass m from the outer envelope values to the inner envelope values. The transition between outer envelope and TBL is set to a specific mass m_{12} . Its thickness in terms of mass is Δm , which is kept constant throughout the evolution, so that the bottom of the TBL lies at $m_{12} - \Delta m$. Because of the linear composition gradient in the TBL, a higher Δm causes a shallower gradient in heavy elements, see Fig. 6.2. Thus, the overall heavy element content of the models decreases slightly with increasing Δm , however, this effect is only relevant for the highest thicknesses considered.

All calculations start with a hot adiabatic profile of $T_{1\text{bar}} = 700$ K. This leads to early luminosities after the first time step on the order of $L_p \sim 5 \times 10^{18}$ W (about 1.3×10^{-8} times the present-day solar luminosity). This is close to the lower limit of initial luminosities extrapolated from results predicted by Mordasini *et al.* (2017) for H/He planets by cold start core accretion models [100]. After the initial profile, the inner envelope locally adopts either the conductive or the adiabatic temperature gradient, whichever is lower, according to Schwarzschild's criterion. The equilibrium temperature T_{eq} increases according to a linearly rising solar luminosity, as presented in Sect. 5.1, between $t = 0$ and the present time $t = 4.56$ Gyr. and T_{eq} is held constant at that level afterwards. The Bond albedo is held constant at $A = 0.3$ for all models, in accordance with the measured values [109, 110]. Tab. 6.1 shows the key model parameters common to all models examined here, while Tab. 6.2 gives the radial extent of the TBL for some example models.

For most models here, the inner envelope is completely composed of heavy elements described by water, so unless noted otherwise, $Z_2 = Z_{2,\text{H}_2\text{O}} = 1$. However, as a lot of these models usually end up a lot hotter in the interior than adiabatic ones, their present-day radii are often larger than the observed values of Uranus and Neptune. So for some models, a mixture of H_2O and basalt was used for the inner envelope, see Sect. 6.5 for details. For simplicity's sake, these models still have a pure rock core, as shown in Fig. 6.1. This might be another simplification, as the existence of such a distinct core is still an open question and models both with and without a rock core separate from an ice-dominated inner envelope can reproduce the observed gravity fields [105].

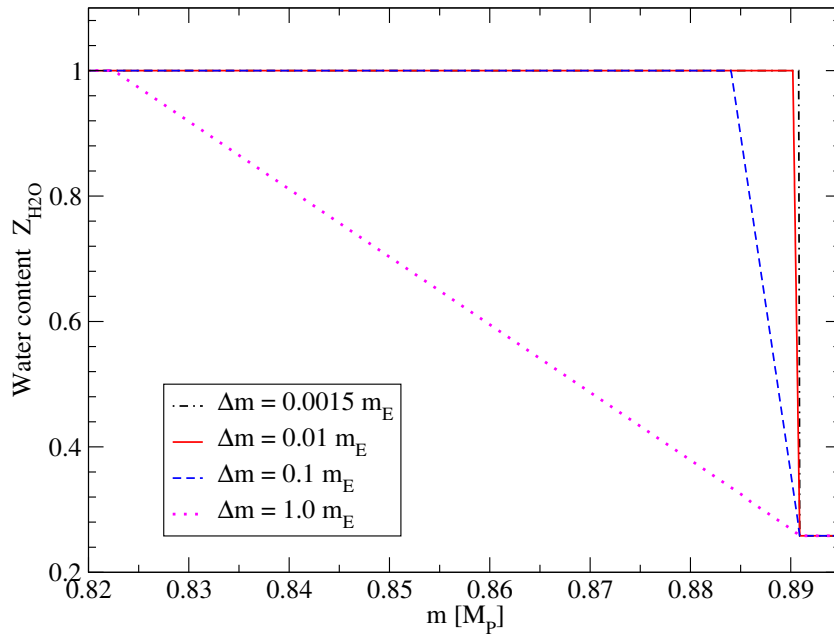


Fig. 6.2.: Water content values $Z_{\text{H}_2\text{O}}$ along Uranus profiles with a conducting TBL of varying thickness Δm . The model makes the Z -gradient for high Δm shallower than for low Δm . Z outside the TBL region is constant. Figure taken from [128].

H and He are described by REOS.3, and the modified MLCP19-EOS is used for H_2O as described in Chap. 4.2. Thermal conductivity values for pure water are used as discussed in Sect. 4.3, however, in Sect. 6.4.2 there will also be an exploration on how a higher thermal conductivity and more efficient energy transport can influence the results. Fig. 6.12 in Sect. 6.6 will give an overview about typical $\lambda_{\text{H}_2\text{O}}$ values along an example model.

These models take a simplified approach and account for only some of the properties of real Uranus and Neptune. While the observed mass, mean radius and luminosity are taken into consideration, and the parameters in Tab. 6.1 are similar to those that do fit the gravitational moments [105], it is not the aim of these models to reproduce the measured gravity field. Likewise, particle transport and interior dynamics such as possible miscibility or immiscibility of materials or convective mixing are not considered here. The purpose is rather to study the effect of an interface in the deep interior that acts as a barrier to efficient energy transport in planets similar to the ice giants. As such, the models will be called 'Uranus' and 'Neptune' despite not being accurate reproductions, because they serve as representations of these planets.

	Uranus	Neptune
Z_1	0.26	0.42
m_{12} / M_E	12.95	15.168
m_{core} / M_E	0.15	1.04

Tab. 6.1.: Parameters used for the TBL models presented here. Quantities are outer envelope heavy-element content Z_1 , mass shell that marks the top of the TBL m_{12} , and core mass m_{core} . Inner envelope heavy-element content $Z_2 = 1$ unless specified otherwise.

$\Delta m [M_E]$	Uranus		Neptune	
	Δr [km]	Z_{total}	Δr [km]	Z_{total}
0.0015	3.0	0.9190	2.2	0.9329
0.005	10.6	0.9189	7.4	0.9328
0.01	21.5	0.9188	15.0	0.9327
0.03	65.2	0.9183	45.6	0.9324
1.0	2320	0.8935	—	—

Tab. 6.2.: Example TBL thicknesses Δm and corresponding radial extent Δr and total heavy element content Z_{total} . Δr is given for $t = 4.56$ Gyr and is about 20 – 45 % smaller than at $t = 0$ due to contraction. All models used in these examples feature $Z_{2,\text{H}_2\text{O}} = 1$ and $\lambda = \lambda_{\text{H}_2\text{O}}$.

6.2. TBL stability considerations

To evaluate whether such a TBL as assumed in these models would remain stable, one can make use of the generalised Ledoux criterion Eq. (2.53), presented in Sect. 2.2.3:

$$\nabla_T \leq \nabla_X + \nabla_{\text{ad}}, \quad (6.1)$$

where ∇_{cond} according to Eq. (2.39) is used for ∇_T in our conductive TBL. This relation has been evaluated as an example for a Uranus and a Neptune model that both end up with a present-day effective temperature and radius close to the observed values for their respective planets. Fig. 6.3 (a) and (b) show the contributions to the Ledoux criterion, ∇_{cond} and $\nabla_{\text{ad}} + \nabla_X$, across the TBL for these models at different points in their evolution. Note that since usually $\nabla_{\text{ad}} \approx 0.2 \dots 0.3$, while $\nabla_X \approx 10^1 \dots 10^3$, ∇_{ad} does not contribute heavily to the relation in these cases. For the Uranus model, which features a comparatively thick TBL and thermal conductivity of $1 \times \lambda$, we see that the conductive temperature gradient exceeds the stabilising compositional gradient at the very outside edge of the TBL for all points in time. That means that this particular part of the planet would be unstable to convection, whereas the majority of the TBL is stably

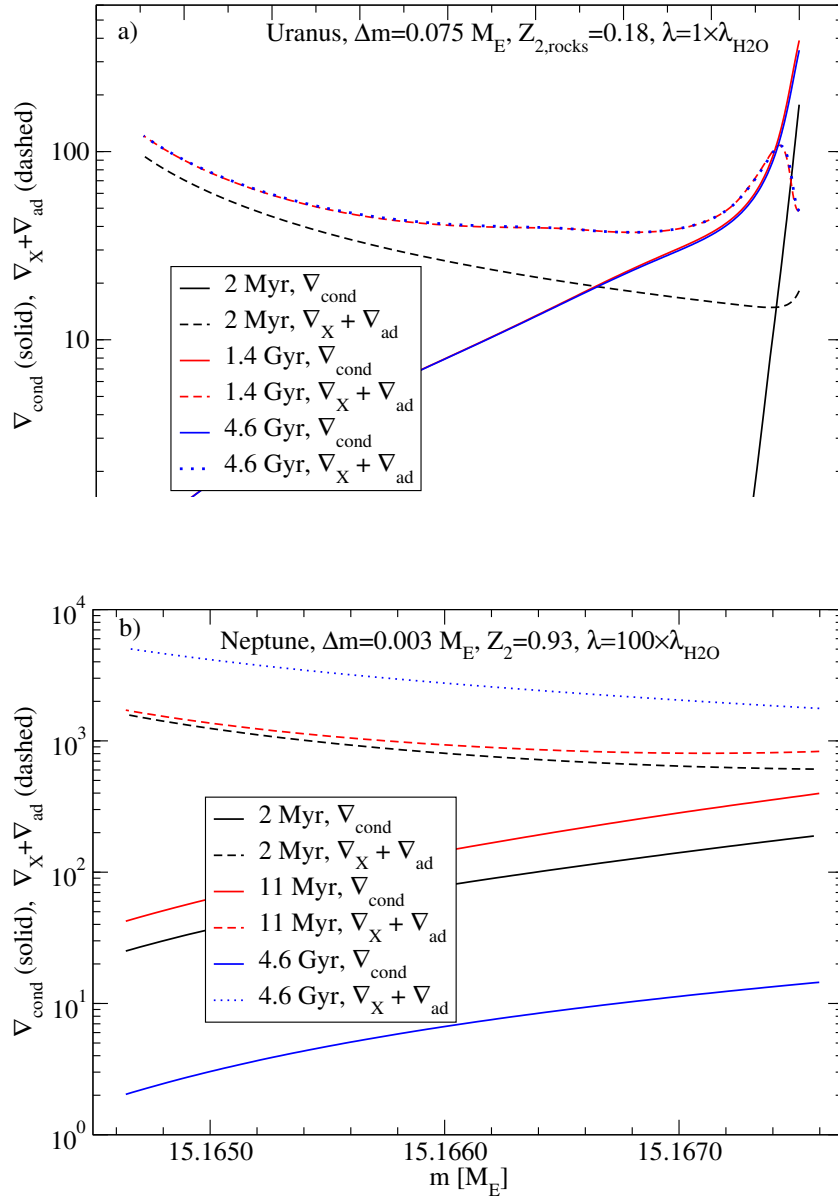


Fig. 6.3.: Gradients in the Ledoux criterion Eq. (2.53) across the TBL for (a) a Uranus model and (b) a Neptune model that both reproduce today's observed T_{eff} and R_p , shown at different times in the evolution: second time step, time of maximum ΔT across the TBL, and present time. Regions where ∇_{cond} exceeds $\nabla_X + \nabla_{\text{ad}}$ would be unstable to convection. Figures taken from Paper II.

stratified. To properly assess how the small region of instability would influence the evolution of the TBL and if it would lead to a partial or even near-complete erosion of the interface, it would be necessary to implement convective mixing and the dynamical growth and shrinking of stable layers into the calculation code, for example via a mixing length approach similar to that presented by Vazan *et al.* (2015) [137] for their giant planet evolution program. Unfortunately, this is beyond the scope of this work.

The Neptune model presented in Fig. 6.3 b) features a considerably smaller TBL of $\Delta m = 0.0003 M_E$ and strongly enhanced conductivity of $\lambda = 100 \times \lambda_{\text{H}_2\text{O}}$. This results in a steeper compositional gradient and a lower ∇_{cond} due to the more potent heat transfer, and that means that the stabilising ∇_X exceeds the temperature gradient for all considered times. Thus, this class of models, which will be further presented in Sect. 6.4.2, exhibits a comfortably stably stratified TBL over the entire evolution.

An interesting note here is that ∇_{cond} can vary over several orders of magnitude within the relatively small extent of the TBL. It is inversely proportional to the temperature T , which rises sharply over several thousand Kelvin within the TBL, as seen in Sect. 6.6, where a closer look at the interior profiles is taken. This is reinforced by the fact that for early times, the local luminosity l – which ∇_{cond} is directly proportional to – decreases from very high values in the outer envelope, where efficient convective energy transport is possible, by several orders of magnitude toward the inner envelope, where almost no energy can flow due to the TBL’s insulation.

6.3. Influence of a conductive interface on the cooling behaviour

In order to investigate the general influence of a thermal barrier on the planetary cooling, let us begin with example models of Uranus and Neptune featuring a TBL of $\Delta m = 0.0015 M_E$. Figure 6.4 shows the evolution of these models, with T_{eff} in panel (a) and temperature difference across the TBL ΔT , local luminosity at the top of the TBL l_1 , and planetary luminosity L in panel (b). Dashed lines in panel (a) show the evolution of a model featuring the same composition but no TBL, called the adiabatic case. There are four characteristic epochs:

(I) the TBL models rapidly become fainter than the adiabatic case even within the first few time steps. Since energy transport across the TBL is a lot less efficient than in

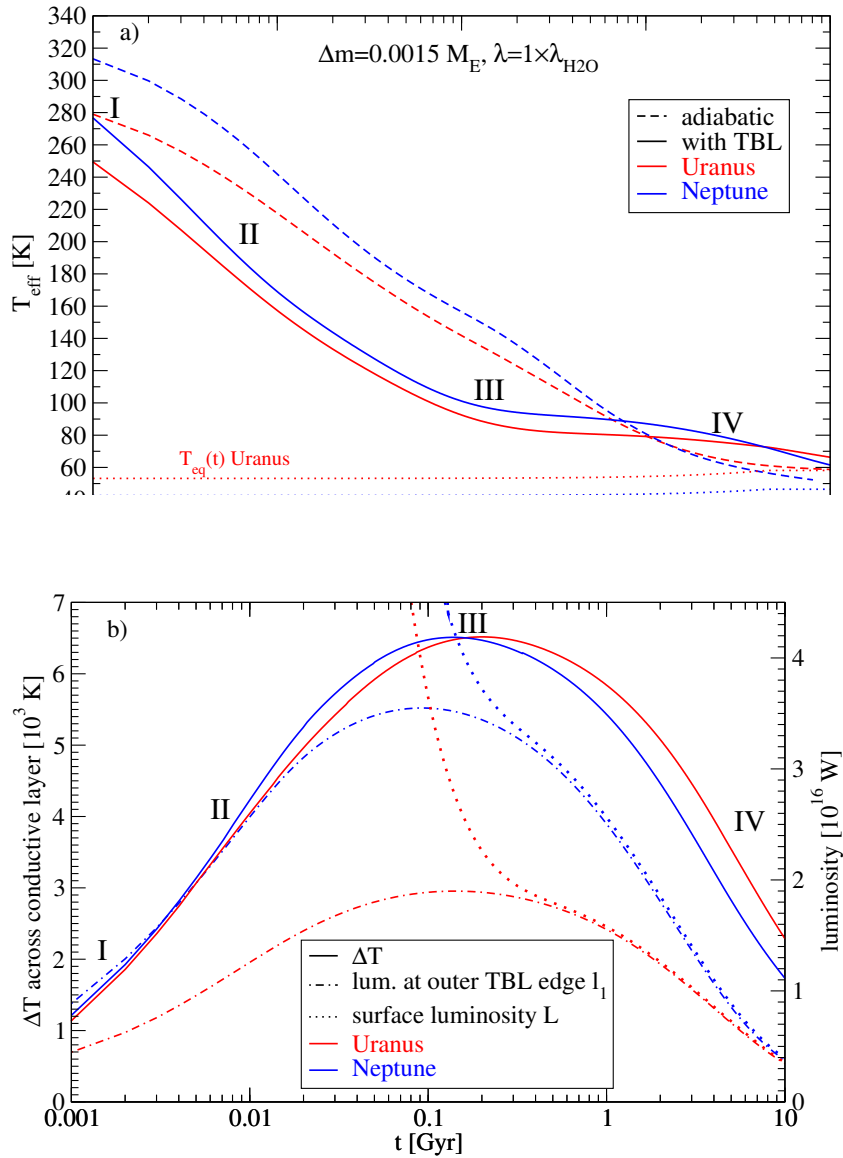


Fig. 6.4.: The four characteristic epochs in the time evolution of a Uranus (red) and a Neptune (blue) model using a TBL of $\Delta m = 0.0015 M_E$. Panel (a) shows the effective temperature T_{eff} and panel (b) shows the temperature difference across TBL ΔT , the luminosity at the outer edge of the TBL l_1 , and the planet surface luminosity L . Dashed lines in (a) are adiabatic models of the same composition and dotted lines show the equilibrium temperatures. Figures taken from Paper II.

convective regions, the inner envelope is almost cut off from cooling, and mainly the outer envelope releases heat. This results in large $\Delta T \sim 1000$ K already after the first time step, although the abrupt, step-like behaviour is probably due to the hot start and the sudden switch from a completely adiabatic initial profile to one with a conductive zone.

(II) After the initial few steps, the outer envelope continues to cool with little energy

contributed by the deep interior, leading to ΔT rising with time. Because a steeper temperature gradient leads to a more efficient conductive heat transport, the luminosity at the outer edge of the TBL l_1 also rises slowly. The outer envelope, meanwhile, continues to radiate heat into space and to contract, meaning the planet's overall luminosity L and T_{eff} decreases. The contraction deposits more gravitational energy in the interior than can be radiated away through the TBL, and so the inner envelope heats up very slightly during the first ~ 100 Myr, as will be seen in Sect. 6.6.

Towards the end of phase II, the temperature at the top of the TBL has significantly fallen (low T_{12}), the cooling of the planet's atmosphere is less efficient – as T_{eff} and L are low – and further contraction of the initially hot and compressible envelope is countered by repulsive particle interaction as the matter becomes denser. As the rising l_1 and the falling L approach each other as shown in Fig. 6.4 b), the decreasing L acts as a cap on l_1 and prevents it from further rising, so that it consequently adopts a maximum.

(III) At this time, the outer envelope is significantly cooler and has contracted more than in the adiabatic model, while the inner envelope still constitutes an enormous energy reservoir for transporting heat outside. This slows the outer envelope's further cooling significantly and T_{eff} adopts an almost plateau-like behaviour. Since the planet is still cooling, albeit slowly, both L and R are still decreasing and l_1 is forced to do the same. Because it is now mainly the inner envelope that cools, ΔT begins to slowly decrease as well.

(IV) After some time has elapsed, which can take billions of years, the bulk of the stored heat from the deep interior has been released. Cooling, and in particular the decrease of T_{eff} , begins to accelerate again.

This general behaviour broadly applies to models with all considered λ values and thin to moderate TBLs, with variations that will be discussed in the next chapter. Notably, the planet can appear fainter (phase II and early phase III) or brighter (late phase III and phase IV) than the adiabatically cooled planet of the same age, providing room to reproduce both Neptune's and Uranus' luminosity depending on the exact assumptions used.

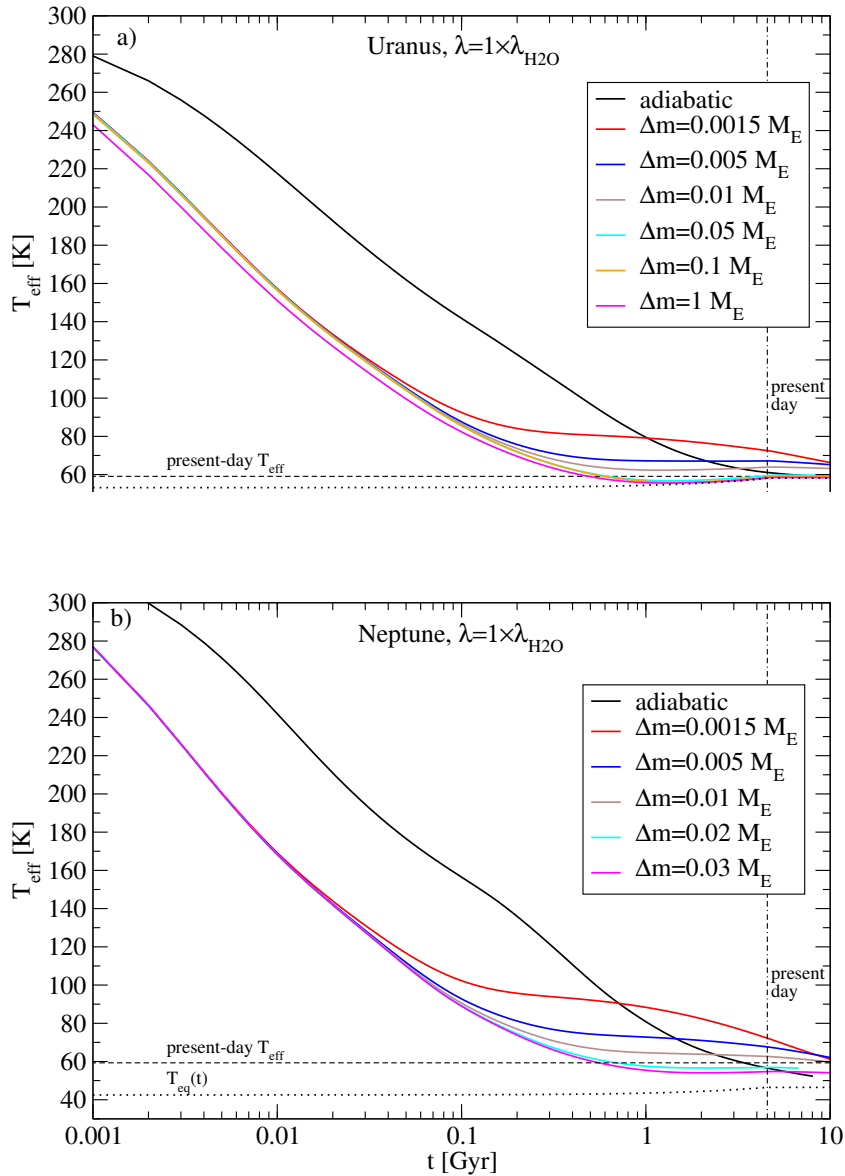


Fig. 6.5.: Evolution of T_{eff} for (a) Uranus and (b) Neptune models of varying TBL thicknesses Δm . In each figure, the black curve shows an adiabatic model of the same composition. Figures adapted from Paper II.

6.4. Parameters influencing the TBL cooling behaviour

6.4.1. TBL thickness

In Fig. 6.5, the evolution of T_{eff} for Uranus and Neptune models with varying TBL thicknesses Δm is presented. Fig. 6.6 shows the evolution of several other key quantities of the TBL for the same Uranus models as in Fig. 6.5 a). The more extended

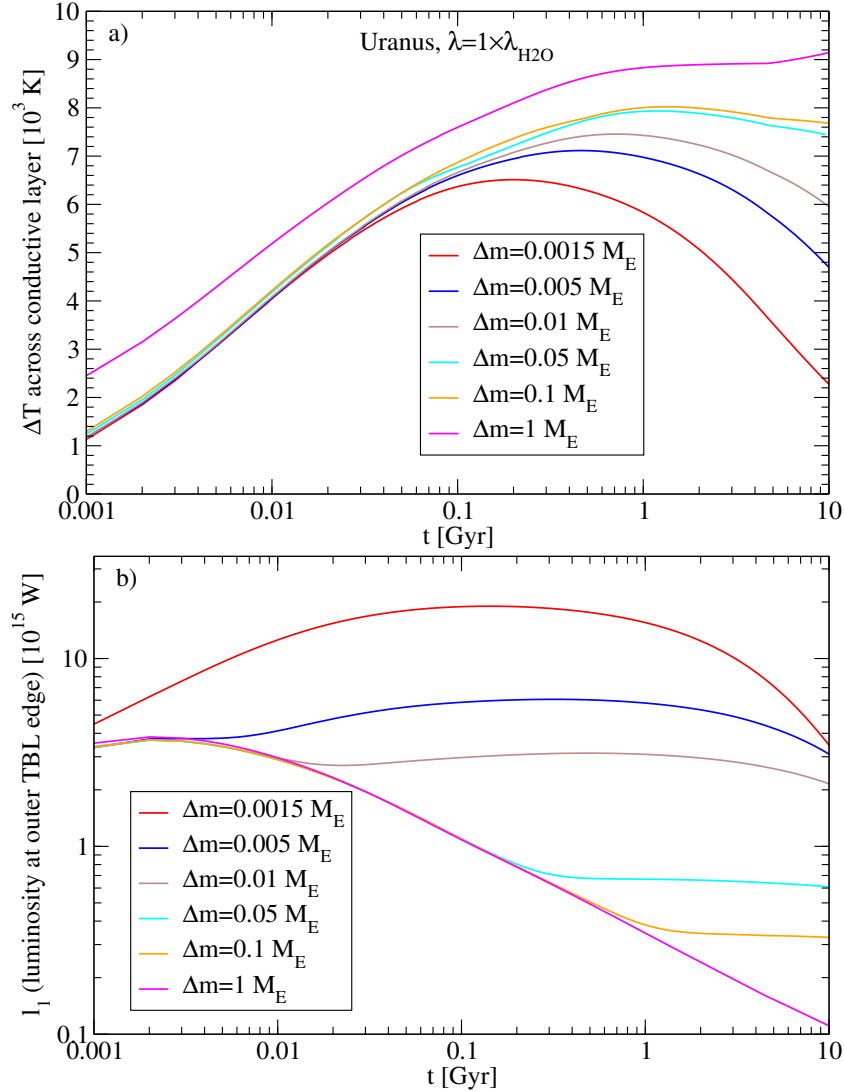


Fig. 6.6.: TBL evolution for Uranus models of varying TBL thickness Δm . (a) temperature difference across TBL ΔT , (b) - luminosity at the outer edge of TBL l_1 , (c) - temperature at the inner edge of TBL. Figures taken from Paper II.

the TBL is, the less efficient the heat transport becomes, leading to a decrease in the luminosity on top of the TBL l_1 with higher Δm , see Fig. 6.6 b). A steeper temperature gradient is required to transport the heat from the deep interior to the outside for thicker TBLs and thus more time elapses before phase III begins, as can be seen in Fig. 6.5. By that later time, the outer envelope has cooled and contracted even more than for smaller Δm , meaning it can now cool even less quickly, which causes phase III to feature a flatter plateau in T_{eff} for higher Δm , as can be seen in Fig. 6.5.

If the transition from phase II to III happens sufficiently late, T_{eff} can be so low that it approaches the equilibrium temperature T_{eq} , though complete thermal equilibrium

is never reached in these models. As can be seen from the outer luminosity boundary condition Eq. (3.7), and was already relevant for the discussion of the influence of T_{eq} on the planetary evolution in Chap. 5, the ability of the surface to radiate heat depends on the difference between T_{eff} and T_{eq} . Therefore it is almost impossible for a planet with T_{eff} near its T_{eq} to cool and its temperature profile stays largely the same over a long period of time (see also Sect. 6.6). In this scenario, T_{eff} can follow the rising T_{eq} and thus even a slight re-heating of the outer envelope can occur, as can be seen in Fig. 6.5. This happens for the Uranus models over a wide range of medium and high Δm , while for Neptune, whose T_{eq} is much lower, the re-heating occurs only very slightly and only for the highest of considered Δm values. This difference is important for the range of viable solutions to reproduce the observed luminosity, as will be discussed in Sect. 6.5.

6.4.2. Thermal conductivity

As discussed in Sect. 4.3, the use of pure H₂O values for λ is a simplification for the mixture of materials likely present in the ice giants' interiors. Here, I take it as an approximate lower bound of the real conductivity. Additionally, the TBL itself might not be a purely conducting region and there might be energy transport mechanisms at work which are more efficient. For example, a region that is stable according to Ledoux' criterion but unstable according to Schwarzschild's criterion is usually thought to develop semi-convection, a relatively slow mixing process that features slower heat transfer than full convection but faster than conduction, see the end of Sect. 2.2.3. Although French & Nettelmann (2019) [34] found, using *ab initio* viscosity values for water, that the range of parameter values that enable semi-convection in Uranus and Neptune is somewhat narrow, it is still quite possible that this occurs in a hypothetical TBL region.

Both of these points suggest that there might be more potent heat transfer across the TBL region than assumed in our models so far. It is therefore prudent to investigate the effect of higher thermal conductivity on the TBL models. This was simply done by multiplying the $\lambda_{\text{H}_2\text{O}}$ values given by [29, 35] by constant factors of up to 1000. Conductivities enhanced by 100 or 1000 are unlikely to be actually encountered in any purely conductive regions in the planets, as even a hydrogen plasma of 20 000 K has $\lambda < 5 \times 10^4 \text{ W K}^{-1} \text{ m}^{-1}$ for conditions similar to our models [59], which is less than 100 times the water values at similar (ρ, T) -conditions. Therefore, these very high λ

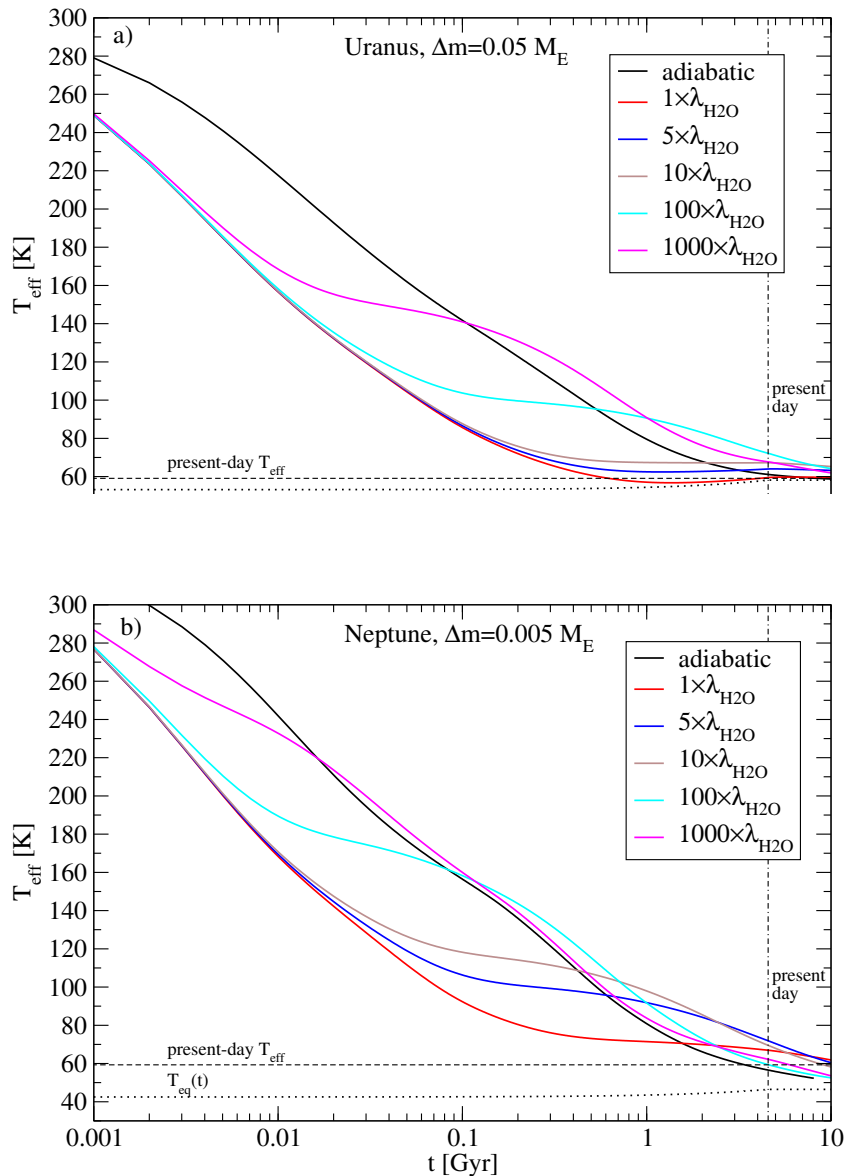


Fig. 6.7.: Evolution of T_{eff} for (a) Uranus models and (b) Neptune models, both with fixed Δm and varying values for the thermal conductivity λ . Figures adapted from Paper II.

enhancements serve primarily as a rough guide to the aforementioned more effective heat transport processes.

Fig. 6.7 shows evolution curves of T_{eff} for Uranus models with a TBL of $\Delta m = 0.05 M_E$ and Neptune models with $\Delta m = 0.005 M_E$ with enhanced λ values. In general, the behaviour seen here is the same as observed in Sect. 6.3 and we clearly see the phases I – IV as described there. However, higher λ values cause the transition from phase II to III to occur at earlier times, and thus at higher T_{eff} . This makes sense because, with the more efficient heat transport, energy from the deep interior can contribute to

the overall evolution more easily. This leads to the outer envelope getting significant contributions from the deep interior already at times when it is more extended than in the $\lambda = 1 \times \lambda_{\text{H}_2\text{O}}$ case, and consequently is still able to radiate away energy faster. This makes the T_{eff} -plateau observed as a feature of phase III less flat than in the $\lambda = 1 \times \lambda_{\text{H}_2\text{O}}$ case, and the slowing down of cooling is less pronounced. This means that a higher λ value acts in the same way as a lower Δm , which will be important when evaluating the resulting present-day T_{eff} values in Sect. 6.5.

Towards the end of the evolution, during phase IV, the evolution curves in Fig. 6.7 a) then converge towards the adiabatic baseline model. This convergence occurs earlier for higher λ . The exception are very high conductivities of $\lambda = 1000 \times \lambda_{\text{H}_2\text{O}}$ where, after a certain time, ∇_{cond} is smaller than ∇_{ad} in the whole of the inner envelope, making it purely stably stratified and conducting, which has a visible effect on the evolution curve.

6.4.3. TBL onset time

In all models presented so far, the conductive TBL is presumed to be present from right after the planet has formed and thus active for the whole evolution. This is not necessarily realistic. For example, if it is compositional differentiation that leads to the stabilising gradient, such as hydrogen and water becoming immiscible and differentiating, as recently explored by Bailey & Stevenson (2021) [4], the TBL could be formed at lower temperatures than in our initial hot profile and therefore later in the planet's lifetime. Thus, for the models presented in this section, which can be called late-onset models, I assume a model of the same composition as so far, but with all layers of the planet being adiabatic until a certain time is reached, which I call the onset time. At that point, the temperature regime in the TBL is switched from adiabatic to conductive and the evolution continues. This is, of course, a simplification again. A TBL formed by H-H₂O demixing, for example, would mean that an initially homogeneous planet would slowly differentiate over time, as a gradient in the heavy-element content Z develops gradually and the water settles deeper in the planet. Such a planet would evolve differently from an already differentiated body where the existing interface is simply switched to a different heat transport scheme partway through the evolution. If the differentiation indeed happened because of H₂-H₂O-immiscibility or a similar sedimentation mechanism, then additional gravitational energy would be released and the planet's outside luminosity would increase. This effect, only for H₂-He demixing,

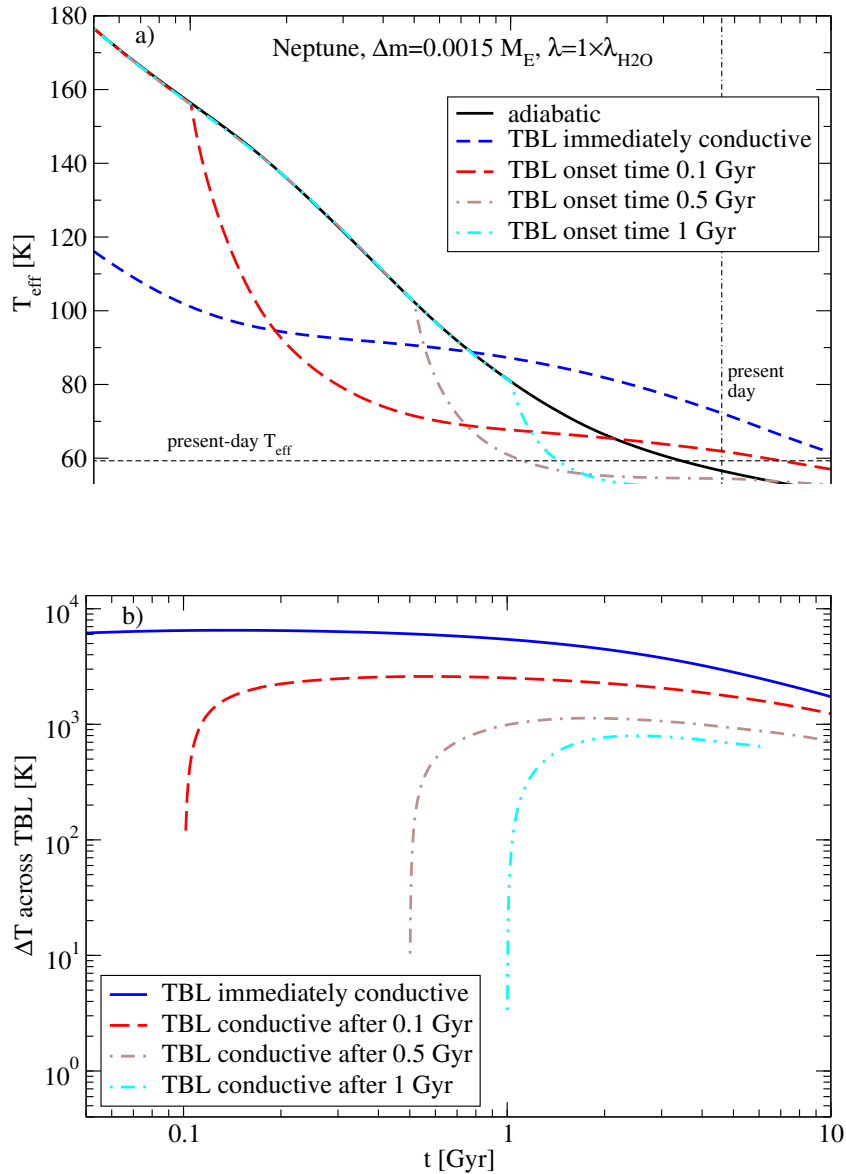


Fig. 6.8.: Evolution of (a) $T_{\text{eff}}(t)$ and (b) $\Delta T(t)$ for a Neptune model with a TBL of $\Delta m = 0.0015 M_E$ featuring different times after which the TBL is set to conductive. Dotted line in (a): equilibrium temperature $T_{\text{eq}}(t)$, thin dashed line: present-day T_{eff} . Figures adapted from Paper II.

is thought to contribute substantially to the evolution of Saturn, for which “standard” adiabatic evolution calculations predict an age that is too low (see e.g. [91, 118, 134]). However, despite these additional contributing factors, the approach taken here is an easy approximation to gauge the influence of a thermal barrier that is formed later in the planet’s lifetime.

In Fig. 6.8, we see the evolution of such a late-onset Neptune model with $\Delta m = 0.0015 M_E$ and $\lambda = 1 \times \lambda_{H_2O}$, with TBL onset after 0.1, 0.5, and 1 Gyr. Once the TBL

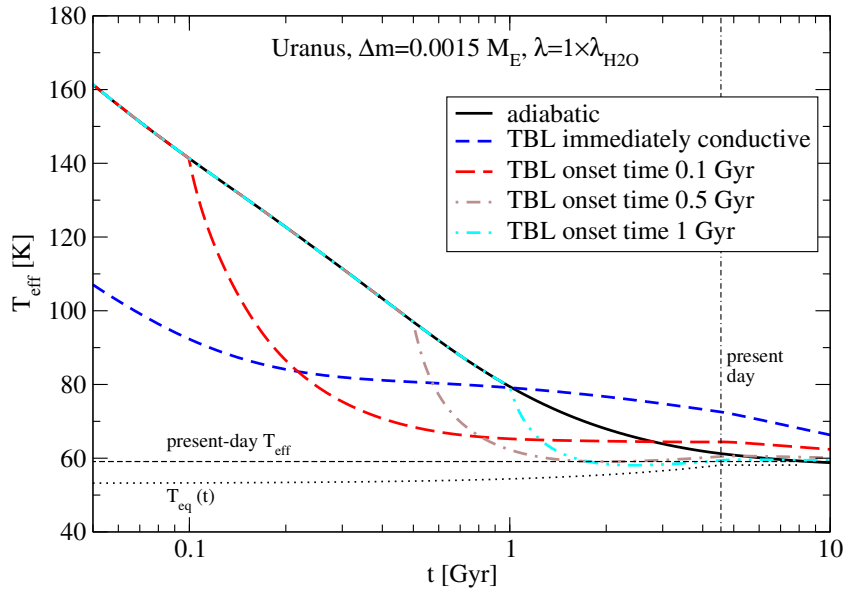


Fig. 6.9.: Same as Fig. 6.8 a), but for Uranus. Figure adapted from Paper II.

is active, a highly accelerated reduction in T_{eff} is seen, similar to phase I and II in the former models. The curve then transitions to a plateau in T_{eff} , corresponding to phase III. In contrast to early-onset models, however, by that point a significant amount of the planet's primordial heat has already left the planet, leaving it with much lower internal heat flow and therefore lower ∇_{cond} in the TBL. Consequently, the initial temperature difference across the interface can be orders of magnitude lower than in previous models, and also the maximum ΔT at the start of phase III is lower. Later onset times lead to lower ΔT .

Late-onset Uranus models presented in Fig. 6.9 show the same general behaviour, with the exception that they, of course, cannot reach T_{eff} substantially below the observed present-day value due to Uranus being so close to equilibrium with the solar irradiation. This also means that Uranus models from this method are less sensitive to the onset time than Neptune models, as long as the TBL onset occurs after about 0.5 Gyr. Neptune, on the other hand, would need an earlier onset to match its observed T_{eff} , because it otherwise cools too quickly. However, taking into consideration the previously discussed additional heat released from the sedimentation, some of this too fast cooling might actually be counteracted. In contrast, for Uranus models this additional energy source requires the presence of a thermal barrier even more, because evolution calculations give already too high luminosities compared to the observations. Ultimately, this can only serve as a basic guide, and the exact effects will have to be

studied in future work where such sedimentation processes have to be specifically and explicitly included.

6.5. Range of present-day effective temperatures

It has already been shown that different parameters can have significant influence on the cooling behaviour of the TBL models. Because one key characteristic to constrain the evolution models is whether they match the measured temperature, let us take a look at the T_{eff} values after $t = 4.6$ Gyr for various values of Δm and λ , as shown in Fig. 6.10. Models that end within 1 K of the observed T_{eff} , which corresponds to about three times the standard uncertainty for Uranus and a little above the standard uncertainty for Neptune, cf. App. A, are shown in white, those that end up too hot in red, and those that are too cold in blue. The resulting colours follow a diagonal pattern from the lower left to the upper right side, owing to the fact that both a higher λ and a lower Δm allow for more efficient heat transfer across the TBL. Therefore, higher λ is able to somewhat compensate a higher Δm , and vice versa (see Sect. 6.4.1 and 6.4.2).

For Uranus, where adiabatic models predict a present-day luminosity higher than the observed value, parameters that result in T_{eff} near the measurement are located towards the lower right corner, featuring low-to medium λ and thicknesses of $\Delta m > 0.05 M_{\text{E}}$. In these models, the deep interior was insulated from the outer envelope sufficiently strongly, so that the outside cooled very rapidly and reached near-equilibrium with solar irradiation, leaving the planet almost incapable of cooling further. Neptune, in contrast, for which adiabatic models predict a luminosity below the observed value, features a smaller band of solutions starting at medium thicknesses of about $\Delta m = 0.015 M_{\text{E}}$, where the planet ends up with T_{eff} close to the observations. Along this slice of solutions, the planet would be in phase III at the present time, and the plateau in T_{eff} would be close to the measured value.

However, Neptune features a second set of solutions that are valid in this sense: for a thin TBL of about $\Delta m = 0.003 M_{\text{E}}$ and strongly enhanced conductivity of about $100 \times \lambda_{\text{H}_2\text{O}}$, the planet would already be in phase IV of the evolution, while the already completed phase III has delayed the outside cooling just long enough to bring the planet into agreement with the measured luminosity. In this case, the delay in heat release caused by the TBL is only on the order of 10 – 100 Myr, which means that even a transient and relatively short-lived period of reduced cooling, maybe caused

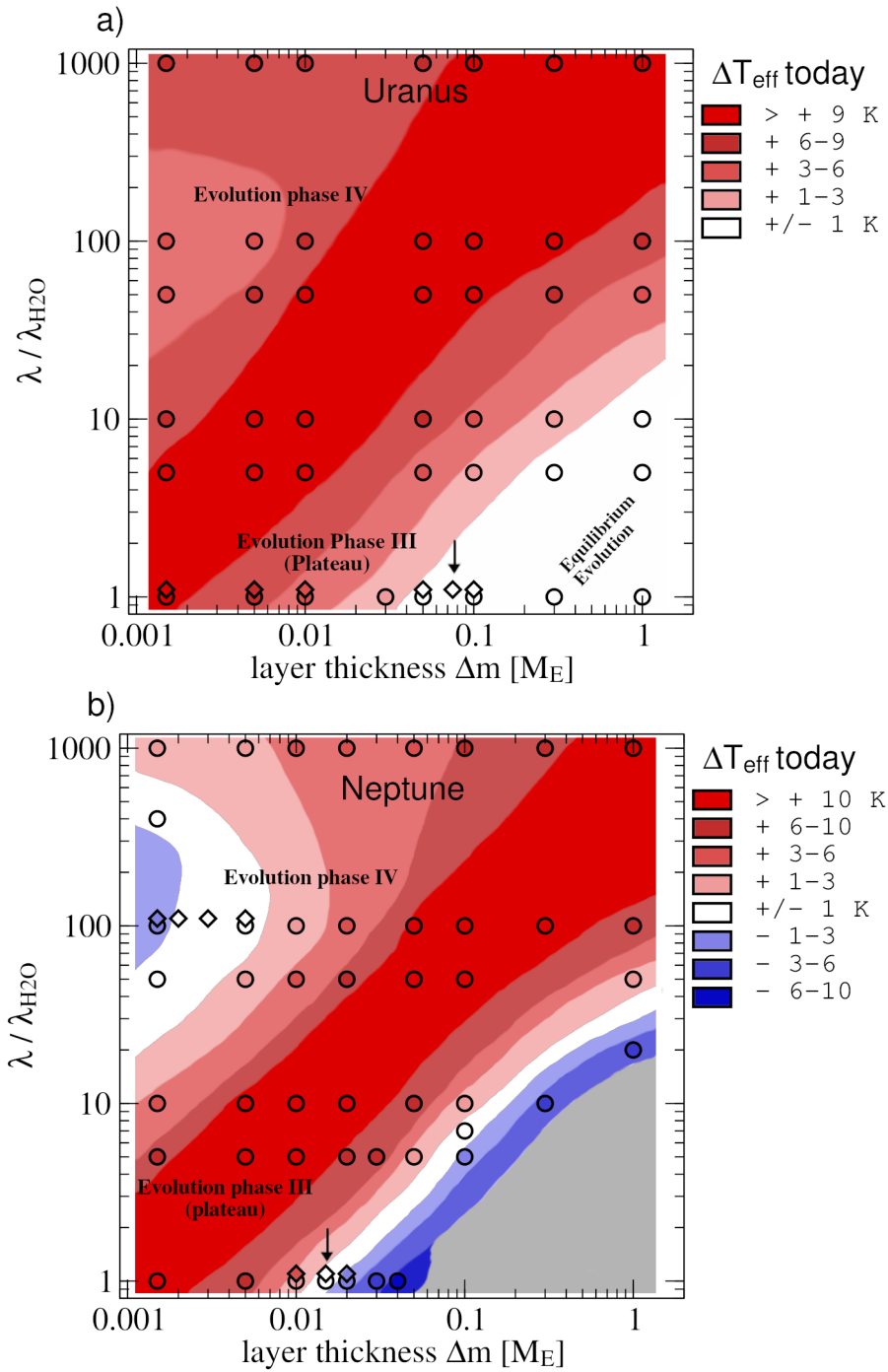


Fig. 6.10.: Effective temperature ranges at $t = 4.6$ Gyr of different planetary evolution models for (a) Uranus and (b) Neptune as a function of TBL thickness Δm and thermal conductivity factor. Models shown as circles have inner envelope water abundances of $Z_{2,\text{H}_2\text{O}} = 1$, those shown as diamonds – near the panel bottoms and in the white halo in (b) – have an inner envelope of either basalt-H₂O-mixture or H-He-H₂O-mixture chosen so that the observed R_p is reproduced at $t = 4.6$ Gyr, see text for details. The Background shading is a rough guide to the eye. Grey area: no data available. Models marked with an arrow are discussed in detail in Sect. 6.6. Figure adapted from Paper II.

by temporary semi-convection, might bring the planet in line with the observed heat flux. This second set of solutions is not observed in Uranus, while, taken at face value, moderate Δm and $1 \times \lambda_{\text{H}_2\text{O}}$ give viable heat fluxes for both ice giants. This will be further discussed in Sect. 6.7.

It should be noted that the majority of models that make up Fig. 6.10 use an inner envelope of pure water $Z_{2,\text{H}_2\text{O}} = 1$. However, the inner envelope temperature profile varies from model to model, and especially all low- λ models are several thousands of Kelvin hotter in the interior – and, consequently, less dense – than adiabatic ones. This leads to variations in the planet’s radius at the present day ($t = 4.6 \text{ Gyr}$). Almost none of the models depicted as circles reproduce the observed mean radius today. Models near the bottom of the plot (lower λ) feature hot interiors with most of the primordial heat still trapped inside, and thus their overall radii at $t = 4.6 \text{ Gyr}$ are too large. Those near the top (high λ) have a rather cool interior and therefore a smaller present-day radius compared to observations. In the first case – hot, low-density interior – it is necessary to use a mixture of water and about 10 – 20 % rocks in the inner envelope, the exact amount depending on the planet and the interface thickness, to have the models reproduce the observed radius at the present. In the second case – cool, dense deep interior – a mixture of water and about 7 % H/He in protosolar proportions is needed. Making these adjustments is a rather time-consuming process as it involves multiple full evolution calculations for each parameter set, and is thus not feasible to do for every model here due to the high computation cost. However, for a subset of models the composition has indeed been fine-tuned such that the planet reproduces the observed radius at $t = 4.6 \text{ Gyr}$ within less than 0.3 %. Those adjusted models are shown as diamonds in Fig. 6.10, and the adjustments produce variation in present-day T_{eff} of up to 2 K. This is substantial, but we also see that this radius adjustment, or rather the lack thereof in the other models, does not seem to shift the resulting trends by much, and, specifically, the parameter ranges identified as producing a valid T_{eff} do not change. Consequently, while most models in Fig. 6.10 produce radii diverging from the observed values, this does not overly affect the discussed behaviour.

6.6. Interior Profiles

In order to examine the effect the TBL has on the interior profiles of the planet, let us take as an example a Uranus_E model with a TBL of $\Delta m = 0.075 M_{\text{E}}$ and an inner envelope rock content of $Z_{2,\text{rocks}} = 0.18$, while the Neptune model features $\Delta m = 0.015 M_{\text{E}}$

72 Ice giant evolution in the presence of a deep internal thermal boundary layer

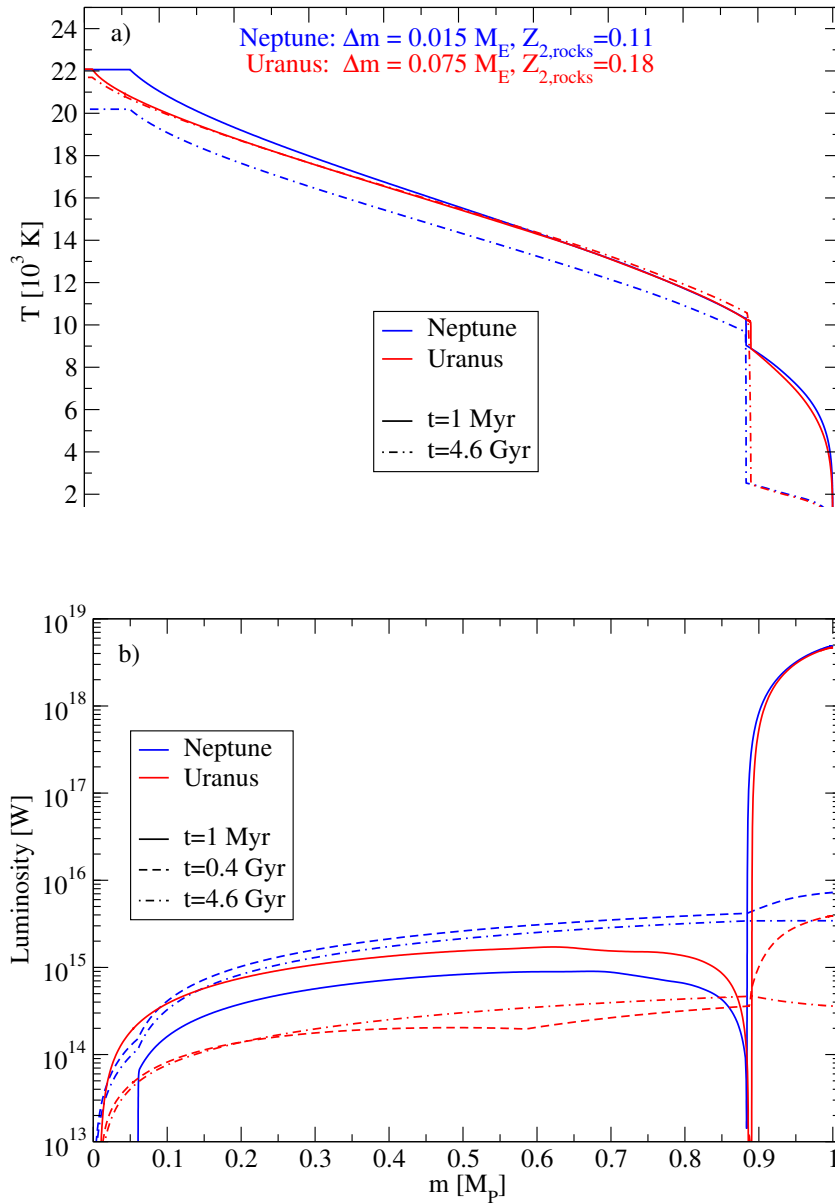


Fig. 6.11.: Interior profiles for Uranus (red) and Neptune (blue) models that reproduce today's radius and effective temperature, at different time steps. (a) Temperature, (b) local luminosity over mass shell. Figures adapted from Paper II.

and $Z_{2,\text{rocks}} = 0.11$, and both use $\lambda = 1 \times \lambda_{\text{H}_2\text{O}}$. These specific models are chosen here because they reasonably reproduce today's measured T_{eff} and R_p . In Fig. 6.11, we see the profiles of temperature T and local luminosity l along the mass coordinate for different points in time during their evolution. In the beginning, the outer luminosity L is high and the outer envelope can cool efficiently, meaning a high local luminosity l in the outer part of the planet. At the TBL, l goes close to zero, indicating almost no net energy transport outside, as the boundary layer inhibits heat transfer. This dip can

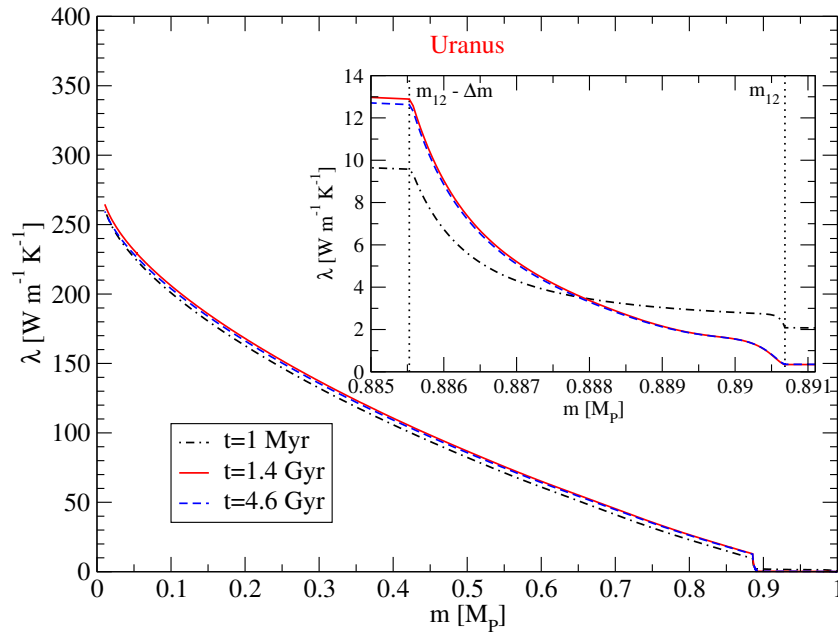


Fig. 6.12.: Thermal conductivity profile for the same Uranus model as in Fig. 6.11 a), shown at different times in the planet's evolution. The inset gives a close-up of the TBL region. Figure adapted from Paper II.

reach even small negative numbers for models with high Δm , where we have a net heat transport inside, due to the cooling and contracting outer envelope compressing the deeper interior. This contraction effect leads to a slight increase in temperature in the inner envelope during evolution phase II.

As time passes and the growing ΔT across the TBL drives a stronger conductive heat transport, the dip in l at the TBL shrinks until it has completely vanished by the start of phase III. At this time, the outer envelope of Uranus is already very close to equilibrium with the solar incidence flux, which means efficient cooling is no longer possible and the inner envelope's temperature profile stays very close to the hot initial model for the entirety of the evolution. In contrast, the Neptune model can still cool even in phase III, and it therefore has a higher present-day luminosity, which matches the observations (Fig. 6.11 b), and a slightly colder inner envelope than in the beginning. It is, however, still significantly hotter than an adiabatic profile and has a rather high $\Delta T \sim 7000$ K across the TBL after 4.56 Gyr.

Fig. 6.12 shows the values of λ along the Uranus model at different times in its evolution. Because λ increases strongly with both temperature and density, it grows roughly by a factor of 10 across the TBL and about by a factor of 25 throughout the inner envelope. However, λ does not change significantly with time, as the TBL essentially preserves the initial conditions in the inner envelope.

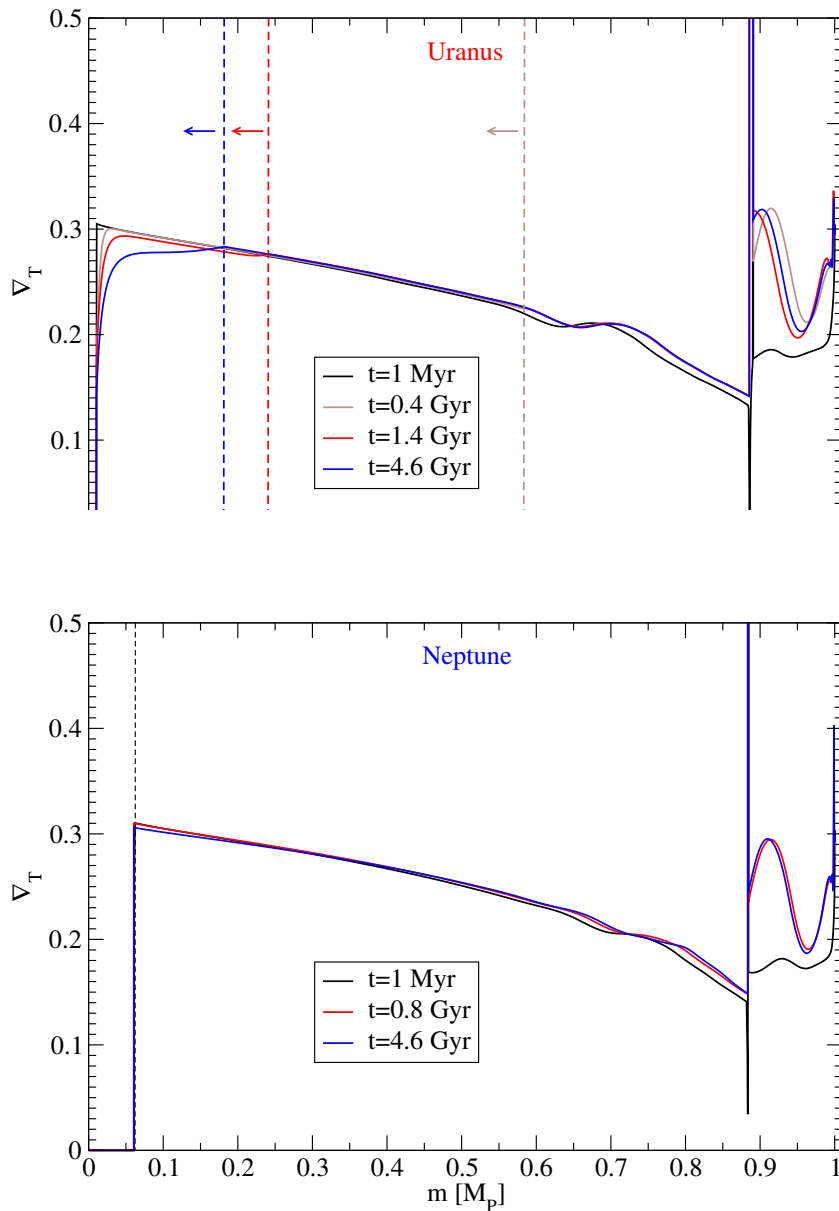


Fig. 6.13.: Temperature gradient over mass for the same Uranus (a) and Neptune (b) models as in Fig. 6.11. The value at the top of the conductive interface is higher than the maximum displayed ∇_T value by several orders of magnitude (cf. Fig. 6.3). The vertical dashed lines in (a) mark the upper end of a conductive zone in the deep interior. Figures taken from Paper II.

In Fig. 6.13, we see the temperature gradient throughout the planet models, again at different points during its evolution. The value at the outside of the TBL is larger than the rest of the displayed values by several orders of magnitude. This makes the very outside part of the TBL unstable to convection under the Ledoux criterion, while the majority of the TBL remains stably stratified throughout the evolution, as was discussed in Sect. 6.2. In the Uranus model, the low $l(m)$ in the inner envelope leads

to low ∇_{cond} (as seen from Eq. (2.39)), and in some parts of the interior, this results in $\nabla_{\text{cond}} < \nabla_{\text{ad}}$, which means these regions become stably stratified according to the Schwarzschild criterion, Eq. (2.54). After about 0.4 Gyr a single deep stable and conductive region is seen, extending from the core to about $0.6 M_{\text{p}}$. This stable area then steadily shrinks from the core as $l(m)$ slowly begins to rise towards the transition to phase III, but is still present at $t = 4.6 \text{ Gyr}$, although only extending to up to $\sim 0.2 M_{\text{p}}$ – corresponding to about $\sim 0.4 R_{\text{p}}$ – at this point. In contrast, the Neptune model, due to its smaller Δm and thus somewhat higher $l(m)$ in the inner envelope, does not develop any stably stratified regions in the deep interior beyond the first few time steps, despite the similarity between the two models seen otherwise.

6.7. Discussion of TBL models

In this chapter, I have presented evolution calculations for Uranus and Neptune models that feature a standard three-layer structure with two extended envelopes and a rock core with a comparatively thin thermally conducting thermal boundary layer between outer and inner envelope. The results show that the inclusion of a thermal barrier of as little as a few km thickness impacts a planet’s thermal evolution dramatically compared to the adiabatic case. This may seem somewhat surprising, as Vazan & Helled (2020) [138] estimate that a conductive layer has to be at least $\sim 100 \text{ km}$ thick to meaningfully affect the planetary evolution of Uranus, while most models considered in this work feature a significantly smaller TBL (cf. Tab. 6.2). Vazan & Helled arrive at their value based on the diffusion time scale for thermal conduction

$$\tau_c = \Delta r^2 \rho c_p / \lambda.$$

and demanding a thermal diffusion time of at least 1 – 5 Gyr in order to meaningfully affect the evolution of the planet. Indeed, if we use the same formula and put in values from our models in this chapter – $\rho = 0.3 \text{ g cm}^{-3}$, $\lambda = 2 \text{ W m}^{-1} \text{ K}^{-1}$, $c_p = 15 \text{ kJ kg}^{-1}$, and radial thicknesses of $\Delta r = 4 – 50 \text{ km}$ (corresponding to $\Delta m = 0.0015 – 0.03 M_{\text{E}}$) – we arrive at significantly shorter time scales of $\tau_{\text{cond}} \sim 1 – 100 \text{ Myr}$. However, this short time scale is consistent with the fact that in my calculations, ΔT increases to several thousand K within just a few million years, which then has a significant influence on the long-term evolution. In essence, a delay in heat transport of a few million to a few hundred million years are seen to be sufficient to strongly change the planet’s cooling

behaviour.

At first, the TBL in these models here leads to a significant drop in outer luminosity and the outer layer cools significantly more quickly compared to an adiabatic case, as effectively only that part can release heat (phase I and II). But when the heat from the interior begins to meaningfully contribute, the cooling of the outer layer is slowed down significantly (phase III), before eventually accelerating again (phase IV). This means that a planet affected by a TBL can either appear brighter or fainter than an adiabatic planet, depending on the stage of the evolution it is in. The latter case is a possibility to bring Uranus models in line with the observed luminosity, while the former provides the same chance for Neptune.

Specifically, these Uranus models are only able to reproduce the measured luminosity if the TBL is sufficiently thick to cut off the deep interior from cooling long enough that the outer envelope hits near-equilibrium with the solar irradiation. This leads to a long time period of the effective temperature evolving in parallel with the equilibrium temperature. In this scenario, the inner envelope remains hot throughout the evolution, with core temperatures of about 2.2×10^4 K and a steep temperature difference of about 8000 K can be found between outer and inner envelope. The high central temperature and hot deep interior is similar to Uranus model No. 2 in [138], that is also characterised by a steep composition gradient between an ice-poor exterior and an ice-rich interior. These central temperatures in this case are also well above those where water would go into the superionic phase as predicted by French *et al.* (2016) [31], which has been put forth as a possible explanation for the ice giants' unusual magnetic field by Redmer *et al.* (2011) [120]. We do observe a deep stably stratified region in these models, as has been a feature in magnetic field simulations by Stanley & Bloxham (2004) [131] and (2006) [132], that reproduce the ice giants' magnetic field. In the example model discussed more closely in Sect. 6.6, it is found below about $0.4 R_p$, which is towards the lower bound for stable layer radii of models favoured by in [132], which fall in the range of $0.4 - 0.55 R_p$.

Neptune models, on the other hand, can reproduce the observed luminosity in two scenarios: first, if the planet is currently in a T_{eff} plateau as part of evolution phase III. Similarly to the Uranus solutions of the previous paragraph, these models feature a hot and only very slowly cooling interior, making the inside conditions of both planets very similar. Second, the Neptune models give another set of solutions for narrow TBLs and a strongly enhanced conductivity, where phase III is already completed and has delayed the cooling just enough to bring its luminosity up to the observations. This second effect is similar to the results by Leconte & Chabrier (2013) [80], who found

that a region of inhibited heat transfer – in that case caused by layered convection – can prolong the evolution of Saturn and provide an explanation for why adiabatic evolution models underestimate that planet’s age. This could suggest that a similar process of semi-convection is or has been a factor in Neptune’s evolution. Models from this range of parameters, due to the efficient energy transport through the TBL, feature central temperatures of about 5400 K, which is in the same range as the adiabatic models presented in Chap. 5, making their present-day interior barely superadiabatic. However, while for the Uranus models we can observe a similar effect of a decreasing T_{eff} compared to $\lambda = 1 \times \lambda_{\text{H}_2\text{O}}$ in that parameter range, those models are still more than 3 K hotter than the observed T_{eff} . Furthermore, solutions in this area are in phase IV of their evolution and therefore hotter than an equivalent adiabatic model, and adiabatic evolution models already overestimate Uranus’ present-day luminosity. Thus, not even a thinner TBL or changes in Uranus’ Bond albedo within the standard uncertainty would help find a viable solution in this range for Uranus. The only way for Uranus to be compatible with this kind of models would be an albedo of greater than 0.4. As briefly discussed in Sect. 5.4, this is not out of the question, but would be a fairly specific case. Additionally, French & Nettelmann (2019) [34] found a somewhat narrow range of parameters for semi-convection without the dynamics in the region turning into either full overturning convection or complete stable stratification.

As has been discussed in Sect. 6.1, the calculations presented here are highly simplified. First, for these models I have neglected the rotational term in the calculation of ∇_T . However, as can be seen in App. E, the effect of this is small enough not to impact the conclusions drawn here. Other assumptions and simplifications in our models that cannot be quantified as easily and should be taken into consideration when evaluating these results, will be briefly discussed below:

The evolution models start from a hot, adiabatic model of $T_{1\text{bar}} = 700$ K. Different initial temperatures mean different initial energy budgets for the planets, which can influence the evolution by changing the position of the T_{eff} -plateau in phase III. Also, while the structure assumed here was clearly differentiated and layered, some formation models predict more gradual composition changes for gas-dominated planets (e.g. Refs. [53, 88]), although for ice giants specifically, Freikh & Murray-Clay (2017) [27] find that formation models require a certain amount of fine-tuning to explain their origin, so it is not easy to find reliable predictions. For both of these issues it is necessary for future work to tie the evolution models more closely to viable planet formation scenarios and to explore how exactly different initial conditions affect the evolution.

78 Ice giant evolution in the presence of a deep internal thermal boundary layer

Furthermore, atmospheric processes were neglected here, such as the condensation of ice species in the deep atmosphere. This is certain to occur in the real planets, because the planetary P - T -curve crosses several phase boundaries, which can significantly influence the surface luminosity [37, 77, 81, 92].

Additionally, the models did not consider the possible erosion of the TBL through the temperature gradient overcoming the stabilising compositional gradient and the subsequent convective mixing, as indeed is the case in the top of the TBL in some of these models.

Ultimately, the existence and exact nature of a deep-lying TBL remains an open question. However, it has been shown that it poses a promising possibility to explain the luminosities of both Uranus and Neptune without necessitating separate assumptions for both planets.

Chapter 7.

Summary and outlook

In this work, I have studied scenarios for the thermal evolution of ice giant planets, in particular Uranus and Neptune. To this end, I have developed a computer code called OTTER, modelling the structure and evolution of giant planets. I have laid out the theoretical foundations and equations the code is based on, as well as the numerical methods employed to solve these equations.

First, I have used these methods to calculate and present a number of homogeneous evolution tracks with adiabatic 3-layer interior models for Uranus and Neptune, using different equations of state and methods of characterising stellar irradiation. The cooling times were notably shorter than previous results. In particular, while Uranus was still found to cool too slowly, Neptune on the other hand was found to cool too quickly, meaning neither planet's present-day luminosity is in line with an adiabatic interior. This further reinforces the previous conclusion that non-adiabatic processes are needed to accurately model these planets [24, 64, 105, 112], which explicitly pertains also to Neptune, according to my results. We have also seen a significant influence of solar irradiation on the cooling time via treatment of the time dependence of the solar luminosity and the value of planetary Bond albedo. This is especially true for Uranus because it is very close to equilibrium with the sun. These uncertainties relating to the influx of energy should be kept in mind while evaluating further evolution calculations.

I have then presented results for ice giant evolution calculations under the assumption of a thermal boundary layer separating the outer and inner envelope, continuing the work of Nettelmann *et al.* (2016) [102], and have investigated the influence of TBL thickness, thermal conductivity and onset time. This has shown that even a thin thermally conducting interface of a few kilometres can influence the cooling in significant ways, making the planet appear either fainter or brighter than an adiabatic model

of equivalent composition, depending on parameters. This means that both Uranus' and Neptune's luminosities are reproducible in this framework, though a certain fine-tuning of the assumptions is still required. Two entirely separate sets of assumptions about the structure and interior dynamics for both planets, as suggested for example by Helled *et al.* (2020) [52], remain a possibility, but are not a necessity. A number of these models compatible with present-day radius and luminosity measurements end up with an interior much hotter than indicated by fully adiabatic models, which is in line with previous non-adiabatic models of Uranus and Neptune [102, 138]. This would make some of the predictions regarding processes in their interior, such as diamond formation [67, 74] and the presence of a superionic water phase [120], at least somewhat doubtful, although not impossible.

At this point, it is important to reiterate that these models are simplifications designed to assess the impact of certain separate factors on the planets' cooling behaviour. The real structure is almost certainly more complex than presented here and is likely to be a result of several influences, such as atmospheric dynamics, deep-interior stratification and demixing processes. The results from this work can now serve as a basis for further investigations into the ice giants. For example, it would be worthwhile to include the possibility of H_2 - H_2O -demixing explicitly in Uranus and Neptune models, continuing the work of Bailey & Stevenson [4], using for example recent new simulations by Bergermann *et al.* [8]. Another promising direction would be to extend the model to allow for a dynamic onset of convection and subsequent mixing, similarly to that used by Vazan & Helled [138], which would provide the opportunity to study the stability and possible erosion of composition gradients. Atmospheric processes such as condensation of volatiles also play an important role and coupled interior-atmosphere evolution models would help assess their impact. Furthermore, evolution scenarios with a deep-lying TBL are not only of interest for Uranus and Neptune. For example, evolution calculations for hot gas giant exoplanets which appear too large for their age, (so-called inflated hot Jupiters), such as WASP-39b [115], display a plateau in their outside luminosity similar to some of the TBL models presented here [115]. Since it is not yet completely understood how these planets have managed to stay that inflated over their evolution, an interior TBL might be a contributor.

The results for Uranus and Neptune models do, however, already indicate that there is a vast wide array of possible structures and dynamics within these planets, and that the existing observables are insufficient to constrain valid evolution models. Smaller observational uncertainties on effective temperature, albedo and atmospheric temperature profile are needed. For example, as we have seen in Chap. 5, raising Uranus'

assumed Bond albedo changes its cooling time dramatically. The most direct way to lessen the uncertainties due to observables will be to conduct another spacecraft mission exploring one or both of the ice giants, which is imperative to further our understanding of this class of planets. On the other hand, improved material data like thermal conductivities of H-C-N-O mixtures, following the simulations for water by e.g. French [29], French & Redmer [35], and Grasselli *et al.* [42], are sure to greatly improve future models. In order to benchmark such simulation data, high-pressure, high-temperature measurements of these material properties are needed, as has been done for example for the thermal conductivity of iron using a laser-heated diamond anvil cell [72].

Ultimately, this work represents a stepping-stone in the endeavour of characterising the processes that presently occur and have occurred inside ice giant planets and as a step towards understanding this unique class of planets in our Solar System and beyond.

Appendix A.

Parameters and Observables

Here, I will give a quick overview about the different quantities that can be observed or directly inferred for the ice giants, insofar as they are relevant for my models.

Mass & Gravity. The planets' gravitational fields are determined by observing the orbits of Uranus' and Neptune's satellites as well as evaluating the trajectory of a passing spacecraft. This yields the planet's total mass M_p – or rather, the product of gravitational constant and mass GM_p – as well as the gravitational moments J_2 and J_4 . These are coefficient in an expansion of the gravitational field into Legendre polynomials and they are affected by the density profile, making it possible to infer the latter from them to a certain degree.

The mass values in Tab. A.1 are taken from Guillot & Gautier (2015) [45], who used the 1987 CODATA value of G to compute M . For Uranus, the mass is based on the

	Uranus	Neptune
Mass $M_p / 10^{26}$ kg [45]	0.86832(1 ± 0.013%)	1.02435(1 ± 0.013%)
Mean radius $R_p / 10^7$ m [45]	2.5364 ± 0.0010	2.4625 ± 0.0020
1-bar-temperature $T_{1\text{bar}} / \text{K}$ [45]	76 ± 2	72 ± 2
Effective temperature $T_{\text{eff}} / \text{K}$ [45]	59.1 ± 0.3	59.3 ± 0.8
Bond albedo A [109, 110]	0.300 ± 0.049	0.290 ± 0.067
Equilibrium temperature T_{eq} / K [109, 110]	58.2 ± 1.0	46.6 ± 1.1
Rotational period $\mathcal{P}_\omega / \text{s}$ [45]	62060 ± 40	58000 ± 200
2nd order grav. moment $J_2 / 10^{-2}$ [105]	0.351099 ± 0.000072	0.35294 ± 0.00045
4th order grav. moment $J_4 / 10^{-4}$ [105]	−0.3361 ± 0.0100	−0.358 ± 0.029
Mean orbital distance a [AU] [145]	19.201	30.048

Tab. A.1.: Observables for Uranus and Neptune. For discussion of the different values, see text.

Solar system age $t_{\odot} / 10^9$ yr [3]	4.56
Solar effective temperature $T_{\odot} /$ K [117]	5772
Solar Radius $R_{\odot} / 10^8$ m [47]	6.9566
Mean earth radius $R_E / 10^6$ m [145]	6,3710
Earth mass $M_E / 10^{24}$ kg [89]	5,9722

Tab. A.2.: Further astronomical quantities used in the models

product GM_p from Anderson *et al.* (1987) [2] that uses Voyager measurements supplemented by previous earth-based observations of the satellites. Neptune’s mass is based on Jacobson (2009) [65], who also uses Voyager and ground-based values, but additionally makes use of observations of Neptune’s second-largest moon Proteus. The reference values of J_2 and J_4 in Tab. A.1 are taken from Nettelmann *et al.* (2013) [105], who scaled existing literature values to the equatorial 1-bar radius. It should be noted that in the interim, updated values of J_2 , J_4 have been calculated for Uranus by Jacobson (2014) [66] and of J_2 for Neptune by Brozović *et al.* (2020) [12], however, as they are compatible with the values given here and the gravitational moments are not the focus of this work, I use the slightly older values.

Rotation period. There is no unique way to define the rotational frequency of a planet that is fluid to a significant degree. Different layers of the planet might rotate with a different speed. This effect, mostly seen in the planets’ atmosphere, could even extent into the planet’s deep interior. The value given in Tab. A.1 from [45] is the value calculated by Warwick *et al.* (1986, Uranus) [143] and Warwick *et al.* (19891, Neptune) [142] to be the rotational period of the planets’ magnetic fields, based on radio measurements during the Voyager 2 flyby. Helled *et al.* (2010) [49] have derived different values by minimising atmospheric wind velocities constrained by the measured atmosphere profile and gravitational moments, deriving about 16.6 h for Uranus and 17.5 h for Neptune.

Energy balance. During its flyby, the infrared and radio spectrometer aboard Voyager 2 measured the radiation given off by the planets. By extrapolating the measured infrared spectrum and calculating the total thermal flux from it, the planet’s effective temperature can be obtained, and evaluation of broad-spectrum reflected radiation from different observation angles can be used to estimate the Bond albedo. These calculations were done by Pearl *et al.* (1990) for Uranus [110] and by Pearl & Conrath (1991) for Neptune [109]. Although more precise and reliable than previous earth-based observations, they still rely on assumptions for atmosphere and seasonal variations, and therefore more direct on-site measurements will help dramatically.

1-bar temperature. During the Voyager flyby, the deviation of radio signals via the atmosphere was measured, which allows inferences about the atmospheric structure, a process called radio occultation. These measurements were evaluated using atmospheric models and composition constraints via infrared emission spectra to give estimates of, among other things, the atmosphere's $P - T$ structure. These calculations, performed by Lindal *et al.* (1987) for Uranus [83] and Lindal (1992) for Neptune [84], give values for $T_{1\text{bar}}$ and also indicate that the atmospheric profile adopts a form close to an adiabat below 1 bar. However, the uncertainties on these values are relatively large due to the sparse measurements.

Radius. The aforementioned analysis of radio occultation measurements also allows the estimation of Uranus' and Neptune's radii. The values used here refer to the 1-bar-level. Because Uranus and Neptune are rotating bodies, they are slightly oblate and their polar radius R_{pol} is smaller than the equatorial one R_{eq} . In order to have a constraint for a spherical model of the planet, the arithmetic mean radius $R_{\text{p}} = (2R_{\text{eq}} + R_{\text{pol}})/3$ is used. The values given in Tab. A.1 are taken from Guillot & Gautier (2015), who calculated them based on R_{eq} and R_{pol} from Lindal (1992) [84].

Appendix B.

Derivations & Proofs

B.1. Approximating the effect of rotation in spherical symmetry

This follows the procedure laid out in [103]. Let us start from the centrifugal force as formulated in Eq. (2.7)

$$d\vec{F}_c = -dm \vec{\omega} \times (\vec{\omega} \times \vec{r}). \quad (\text{B.1})$$

We start by considering cylinder coordinates ρ, φ, z , where \vec{e}_z is parallel to the axis of rotation. Note that ρ here denotes the distance to the rotation axis and not the density. In this description, we have

$$\vec{\omega} = \omega \vec{e}_z, \quad (\text{B.2})$$

$$\vec{r} = \rho \vec{e}_\rho + z \vec{e}_z, \quad (\text{B.3})$$

$$d\vec{F}_c = -dm \vec{\omega} \times (\vec{\omega} \times \vec{r}) = -dm \vec{\omega} \times (\rho \omega \vec{e}_\varphi), \quad (\text{B.4})$$

$$d\vec{F}_c = dm \rho \omega^2 \vec{e}_\rho. \quad (\text{B.5})$$

We can define a centrifugal potential Q by

$$d\vec{F}_c = -dm \text{grad}Q, \quad (\text{B.6})$$

and, using the above expression for F_c and the formulation of the gradient in cylinder coordinates [11]

$$\text{grad}Q = \frac{\partial Q}{\partial \rho} \vec{e}_\rho + \frac{1}{\rho} \frac{\partial Q}{\partial \varphi} \vec{e}_\varphi + \frac{\partial Q}{\partial z} \vec{e}_z, \quad (\text{B.7})$$

the definition (B.6) is satisfied by the potential

$$Q = -\frac{1}{2} \omega^2 \rho^2. \quad (\text{B.8})$$

If we now switch to spherical coordinates r, φ, θ , this becomes

$$Q = -\frac{1}{2} \omega^2 (r \sin \theta)^2, \quad (\text{B.9})$$

$$Q = -\frac{1}{3} \omega^2 r^2 (P_0 - P_2(\cos \theta)). \quad (\text{B.10})$$

In this form, Q is expressed as an expansion in terms of Legendre polynomials P_i , with

$$P_0(x) = 1, \quad (\text{B.11})$$

$$P_2(x) = \frac{3}{2} x^2 - \frac{1}{2}. \quad (\text{B.12})$$

If we now approximate Eq. (B.10) to the zeroth order, i.e. take only the term P_0 , we obtain

$$Q \approx -\frac{1}{3} \omega^2 r^2, \quad (\text{B.13})$$

$$dF_c = |d\vec{F}_c| \approx dm \frac{2}{3} \omega^2 r, \quad (\text{B.14})$$

which is Eq. (2.8).

B.2. Formulating δq in Terms of T and P

This section follows the description laid out by Kippenhahn *et al.* in Sect. 4.1 of [70]. Let us start with Eq. (2.16), the first law of thermodynamics

$$\delta q = du + P dv = du - \frac{P}{\rho^2} d\rho. \quad (\text{B.15})$$

Because, for fixed composition, u depends only on, say, ρ and T , we can write its total differential as

$$du = \left(\frac{\partial u}{\partial \rho} \right)_T d\rho + \left(\frac{\partial u}{\partial T} \right)_\rho dT, \quad (\text{B.16})$$

which, inserted into Eq. (B.15), leads to

$$\delta q = \left[\left(\frac{\partial u}{\partial \rho} \right)_T - \frac{P}{\rho^2} \right] d\rho + \left(\frac{\partial u}{\partial T} \right)_\rho dT. \quad (\text{B.17})$$

Now, let us take a look at the fundamental thermodynamic relation for the entropy [107]

$$ds = \frac{1}{T} du + \frac{P}{T} dv = \frac{1}{T} du - \frac{P}{\rho^2 T} d\rho, \quad (\text{B.18})$$

where s and v are the specific values of entropy and volume, respectively. Using again the relation for du (B.16), this becomes

$$ds = \left[\frac{1}{T} \left(\frac{\partial u}{\partial \rho} \right)_T - \frac{P}{\rho^2 T} \right] d\rho + \frac{1}{T} \left(\frac{\partial u}{\partial T} \right)_\rho dT. \quad (\text{B.19})$$

Since this is a total differential form, the Schwarz integrability condition

$$\frac{\partial}{\partial \rho} \left(\frac{\partial s}{\partial T} \right) = \frac{\partial}{\partial T} \left(\frac{\partial s}{\partial \rho} \right) \quad (\text{B.20})$$

gives us

$$\begin{aligned} \frac{\partial}{\partial \rho} \left[\frac{1}{T} \left(\frac{\partial u}{\partial T} \right)_\rho \right] &= \frac{\partial}{\partial T} \left[\frac{1}{T} \left(\frac{\partial u}{\partial \rho} \right)_T - \frac{P}{\rho^2 T} \right] \\ \Leftrightarrow \frac{1}{T} \frac{\partial^2 u}{\partial \rho \partial T} &= \frac{1}{T} \frac{\partial^2 u}{\partial T \partial \rho} - \frac{1}{T^2} \left(\frac{\partial u}{\partial \rho} \right)_T - \frac{1}{\rho^2 T} \left(\frac{\partial P}{\partial T} \right)_\rho + \frac{P}{\rho^2 T^2} \\ \Leftrightarrow \left(\frac{\partial u}{\partial \rho} \right)_T &= \frac{P}{\rho^2} - \frac{T}{\rho^2} \left(\frac{\partial P}{\partial T} \right)_\rho. \end{aligned} \quad (\text{B.21})$$

If we now insert Eq. (B.21) into (B.17), we get

$$\delta q = \left(\frac{\partial u}{\partial T} \right)_\rho dT - \frac{T}{\rho^2} \left(\frac{\partial P}{\partial T} \right)_\rho d\rho. \quad (\text{B.22})$$

For fixed composition, the density depends on P and T and we can write its total differential as

$$d\rho = \left(\frac{\partial\rho}{\partial P}\right)_T dP + \left(\frac{\partial\rho}{\partial T}\right)_P dT, \quad (\text{B.23})$$

which we can insert into Eq. (B.22), making use of the definition of δ_ρ (2.23), $\left(\frac{\partial\rho}{\partial T}\right)_P = -\frac{\rho}{T}\delta_\rho$, which gives us

$$\begin{aligned} \delta q &= \left(\frac{\partial u}{\partial T}\right)_\rho dT - \frac{T}{\rho^2} \left(\frac{\partial P}{\partial T}\right)_\rho \left[\left(\frac{\partial\rho}{\partial P}\right)_T dP - \frac{\rho\delta_\rho}{T} dT \right] \\ &= \left[\left(\frac{\partial u}{\partial T}\right)_\rho + \frac{\delta_\rho}{\rho} \left(\frac{\partial P}{\partial T}\right)_\rho \right] dT - \frac{T}{\rho^2} \left(\frac{\partial P}{\partial T}\right)_\rho \left(\frac{\partial\rho}{\partial P}\right)_T dP, \end{aligned} \quad (\text{B.24})$$

which, by use of the cyclic chain rule,

$$-1 = \left(\frac{\partial\rho}{\partial P}\right)_T \left(\frac{\partial P}{\partial T}\right)_\rho \left(\frac{\partial T}{\partial\rho}\right)_P, \quad (\text{B.25})$$

$$\left(\frac{\partial\rho}{\partial P}\right)_T = -\left(\frac{\partial T}{\partial P}\right)_\rho \left(\frac{\partial\rho}{\partial T}\right)_P = \frac{\rho\delta_\rho}{T} \left(\frac{\partial T}{\partial P}\right)_\rho, \quad (\text{B.26})$$

then becomes

$$\delta q = \left[\left(\frac{\partial u}{\partial T}\right)_\rho + \frac{\delta_\rho}{\rho} \left(\frac{\partial P}{\partial T}\right)_\rho \right] dT - \frac{\delta_\rho}{\rho} dP. \quad (\text{B.27})$$

To switch over from a description $u(\rho, T)$ to $u(P, T)$, we use the multi-variable chain rule, which in general for two independent variables reads [11]:

$$\frac{\partial w(\beta, \gamma)}{\partial\beta} = \frac{\partial w(y, z)}{\partial y} \frac{\partial y(\beta, \gamma)}{\partial\beta} + \frac{\partial w(y, z)}{\partial z} \frac{\partial z(\beta, \gamma)}{\partial\beta}, \quad (\text{B.28})$$

where we set $w = u$, $\beta = y = T$, $\gamma = P$, and $z = \rho$, which gives us

$$\left(\frac{\partial u}{\partial T}\right)_P = \left(\frac{\partial u}{\partial T}\right)_\rho + \left(\frac{\partial u}{\partial\rho}\right)_T \left(\frac{\partial\rho}{\partial T}\right)_P. \quad (\text{B.29})$$

We can again insert (B.21) and also use the definition of δ_ρ (2.23), leading to

$$\begin{aligned} \left(\frac{\partial u}{\partial T}\right)_P &= \left(\frac{\partial u}{\partial T}\right)_\rho - \left[\frac{P}{\rho^2} - \frac{T}{\rho^2} \left(\frac{\partial P}{\partial T}\right)_\rho\right] \frac{\rho}{T} \delta_\rho \\ &= \left(\frac{\partial u}{\partial T}\right)_\rho - \frac{P\delta_\rho}{\rho T} + \frac{\delta_\rho}{\rho} \left(\frac{\partial P}{\partial T}\right)_\rho \\ \Leftrightarrow \left(\frac{\partial u}{\partial T}\right)_\rho &= \left(\frac{\partial u}{\partial T}\right)_P + \frac{P\delta_\rho}{\rho T} - \frac{\delta_\rho}{\rho} \left(\frac{\partial P}{\partial T}\right)_\rho. \end{aligned} \quad (\text{B.30})$$

Inserting Eq. (B.30) into Eq. (B.27) gives

$$\begin{aligned} dq &= \left[\left(\frac{\partial u}{\partial T}\right)_P + \frac{P\delta_\rho}{\rho T}\right] dT - \frac{\delta_\rho}{\rho} dP, \\ &= \left[\left(\frac{\partial u}{\partial T}\right)_P - \frac{P}{\rho^2} \left(\frac{\partial \rho}{\partial T}\right)_P\right] dT - \frac{\delta_\rho}{\rho} dP \end{aligned} \quad (\text{B.31})$$

which, using the definition of c_p (2.22) finally leads to

$$dq = c_p dT - \frac{\delta_\rho}{\rho} dP. \quad (\text{B.32})$$

B.3. The adiabatic temperature gradient

To derive an expression for the adiabatic temperature gradient ∇_{ad} , we start with the cyclic chain rule $\left(\frac{\partial x}{\partial y}\right)_z \left(\frac{\partial y}{\partial z}\right)_x \left(\frac{\partial z}{\partial x}\right)_y = -1$, specifically

$$\left(\frac{\partial T}{\partial P}\right)_s = -\frac{\left(\frac{\partial s}{\partial P}\right)_T}{\left(\frac{\partial s}{\partial T}\right)_P}. \quad (\text{B.33})$$

Taking the fundamental thermodynamic relation for the enthalpy

$$dh = T ds = v dP, \quad (\text{B.34})$$

where h, s, v are the specific values of enthalpy, entropy and volume, respectively, and rearranging Eq. (B.34), we find

$$ds = \frac{1}{T} dh - v dP, \quad (\text{B.35})$$

and therefore,

$$\left(\frac{\partial s}{\partial T}\right)_P = \frac{1}{T} \left(\frac{\partial h}{\partial T}\right)_P. \quad (\text{B.36})$$

Additionally, let us take the Maxwell relation

$$\left(\frac{\partial s}{\partial P}\right)_T = - \left(\frac{\partial v}{\partial T}\right)_P, \quad (\text{B.37})$$

and Eq. (B.33) becomes (using $h = u + Pv$, as well as the definitions for δ_ρ and c_p):

$$\left(\frac{\partial T}{\partial P}\right)_s = \frac{\left(\frac{\partial v}{\partial T}\right)_P}{\frac{1}{T} \left(\frac{\partial h}{\partial T}\right)_P} \quad (\text{B.38})$$

$$= \frac{T \left(\frac{\partial v}{\partial T}\right)_P}{\left(\frac{\partial u}{\partial T}\right)_P + P \left(\frac{\partial v}{\partial T}\right)_P} \quad (\text{B.39})$$

$$= \frac{\overbrace{-\frac{\delta_\rho/\rho}{\rho^2} \left(\frac{\partial \rho}{\partial T}\right)_P}^{\delta_\rho/\rho}}{\underbrace{\left(\frac{\partial u}{\partial T}\right)_P - \frac{P}{\rho^2} \left(\frac{\partial \rho}{\partial T}\right)_P}_{c_p}} \quad (\text{B.40})$$

$$= \frac{\delta_\rho}{\rho c_p} \quad (\text{B.41})$$

and therefore

$$\nabla_{\text{ad}} = \frac{P}{T} \left(\frac{\partial T}{\partial P}\right)_s = \frac{P \delta_\rho}{T \rho c_p}. \quad (\text{B.42})$$

B.4. Calculating the composition gradient ∇_X

The quantity ∇_X was defined in Eq. (2.45) as

$$\nabla_X = \sum_i \frac{dX_i}{d \ln P} \left(\frac{\partial \ln T}{\partial X_i} \right)_{P, \rho, \{X_{k \neq i}\}} = \frac{P}{T} \sum_i \frac{dX_i}{dP} \left(\frac{\partial T}{\partial X_i} \right)_{P, \rho, \{X_{k \neq i}\}}. \quad (\text{B.43})$$

The first factor is the change in the different abundances along the pressure profile of the planet. It is approximated as the corresponding difference coefficient

$$\frac{dX_i}{d \ln P} \approx \frac{X_i^{j+1} - X_i^{j-1}}{\ln P^{j+1} - \ln P^{j-1}} \quad (\text{B.44})$$

where j refers to the mass point where the quantity is evaluated. For the second term, we use the cyclic chain rule again

$$\left(\frac{\partial T}{\partial X_i} \right)_{P, \rho, \{X_{k \neq i}\}} = - \frac{\left(\frac{\partial \rho}{\partial X_i} \right)_{P, T, \{X_{k \neq i}\}}}{\left(\frac{\partial \rho}{\partial T} \right)_{P, \{X_j\}}}. \quad (\text{B.45})$$

Both of these can be calculated from the equation of state relation $\rho = \rho(P, T, \{X_j\})$. The denominator is analogous to the coefficient of isothermal expansion (2.23), while the numerator represents the change in density for changing abundances. For the latter, there is now the question on how exactly to calculate it.

Case 1: If the material abundances are treated as independent quantities, then $\left(\frac{\partial \rho}{\partial X_i} \right)_{P, T, \{X_{k \neq i}\}}$ can straightforwardly be calculated from the ideal mixing rule, as presented in Eq. (4.2):

$$\frac{1}{\rho(P, T, \{X_j\})} = \sum_k \frac{X_k}{\rho_k(P, T)}, \quad (\text{B.46})$$

$$\left(\frac{\partial 1/\rho}{\partial X_i} \right)_{P, T, \{X_{k \neq i}\}} = \frac{1}{\rho_i}, \quad (\text{B.47})$$

$$\text{Case 1: } \left(\frac{\partial \rho}{\partial X_i} \right)_{P, T, \{X_{k \neq i}\}} = - \frac{\rho^2}{\rho_i}. \quad (\text{B.48})$$

However, this ignores the condition that, because X_i are mass fractions, they have to hold to

$$\sum_i X_i = 1, \quad (\text{B.49})$$

so are not truly independent quantities. This condition is enforced for every point along the planetary profile, so it is automatically accounted for in the calculation of Eq. (B.44). However, it is less clear how exactly Eq. (B.49) has to be considered when calculating the partial derivative $\left(\frac{\partial \rho}{\partial X_i}\right)_{P,T,\{X_{k \neq i}\}}$. An intuitive way to account for this constraint is to pick one of the abundances and have it depend on the others:

Case 2: Let us say, with no loss of generality, that every X_i except for X_H is independent, and that X_H changes so that the sum stays conserved. In this case, the density is calculated as

$$X_H = 1 - \sum_{k \neq H} X_k \quad (\text{B.50})$$

$$\frac{1}{\rho(P, T, \{X_j\})} = \frac{1}{\rho_H(P, T)} \left(1 - \sum_{k \neq H} X_k\right) + \sum_{k \neq H} \frac{X_k}{\rho_k(P, T)} \quad (\text{B.51})$$

$$\text{Case 2: } \left(\frac{\partial \rho}{\partial X_i}\right)_{P,T,\{X_{k \neq i}\}} = -\rho^2 \left(\frac{1}{\rho_i} - \frac{1}{\rho_H}\right) \quad (\text{B.52})$$

To evaluate, how ∇_X would look in these two cases, let us recast Eq. (B.43) with the help of Eq. (B.45) as

$$\nabla_X = -\frac{P}{T} \left(\frac{\partial \rho}{\partial T}\right)^{-1} \underbrace{\sum_i \frac{dX_i}{d \ln P} \left(\frac{\partial \rho}{\partial X_i}\right)_{P,T,\{X_{k \neq i}\}}}_{\sigma}, \quad (\text{B.53})$$

and concentrate on the term designated as σ . In our case 1, this becomes

$$\sigma_1 = \sum_i -\frac{dX_i}{d \ln P} \frac{\rho^2}{\rho_i} \quad (\text{B.54})$$

$$= -\sum_{i \neq H} \frac{dX_i}{d \ln P} \frac{\rho^2}{\rho_i} - \frac{dX_H}{d \ln P} \frac{\rho^2}{\rho_H}, \quad (\text{B.55})$$

where we have simply moved the first addend of the sum out to an extra term. As mentioned before, along the planetary profile the condition of $\sum_i X_i = 1$ is in effect,

which leads to $dX_H = -\sum_{i \neq H} dX_i$, and thus:

$$\sigma_1 = -\sum_{i \neq H} \frac{dX_i}{d \ln P} \frac{\rho^2}{\rho_i} + \frac{\rho^2}{\rho_H} \sum_{i \neq H} \frac{dX_i}{d \ln P} \quad (\text{B.56})$$

$$= -\sum_{i \neq H} \left(\frac{dX_i}{d \ln P} \frac{\rho^2}{\rho_i} - \frac{\rho^2}{\rho_H} \frac{dX_i}{d \ln P} \right) \quad (\text{B.57})$$

$$= \sum_{i \neq H} -\rho^2 \frac{dX_i}{d \ln P} \left(\frac{1}{\rho_i} - \frac{1}{\rho_H} \right) = \sigma_2 \quad (\text{B.58})$$

$$(\text{B.59})$$

which equals the σ -term in case 2. So, both approaches give the same result for the final ∇_X , and the condition (B.49) can be disregarded when calculating $\left(\frac{\partial \rho}{\partial X_i} \right)_{P,T,\{X_{k \neq i}\}}$, as long as it is enforced in the planet profile itself.

Appendix C.

Functions and derivatives for the H -matrix

To calculate the matrix H in equation (3.26), the functions

$$G_i^j := \frac{y_i^{j+1} - y_i^j}{\Delta \xi^{j+1}} - f_i \left(y_0^{j+\frac{1}{2}}, y_1^{j+\frac{1}{2}}, y_2^{j+\frac{1}{2}}, y_3^{j+\frac{1}{2}} \right) = 0, \quad i = 0, \dots, 3, \quad (\text{C.1})$$

as well as their derivatives with respect to y_i^j and y_i^{j+1} have to be formulated. The superscript j refers to the mass point at which the functions are evaluated, with $j = 0$ at the planet's surface and $j = N - 1$ in its centre. First, let us remind ourselves of the definitions

$$\begin{aligned} y_0 &= \ln r, & \frac{\partial r}{\partial y_0} &= r, \\ y_1 &= \ln P, & \frac{\partial P}{\partial y_1} &= P, \\ y_2 &= \ln T, & \frac{\partial T}{\partial y_2} &= T, \\ y_3 &= \ln(l + L_c), & \frac{\partial l}{\partial y_3} &= l + L_c, \\ y_i^{j+\frac{1}{2}} &= \frac{y_i^j + y_i^{j+1}}{2}, \\ \xi &= \ln \left(1 - \frac{m}{(1 + \eta)M_{\text{ges}}} \right) = \ln \left(1 - \frac{m}{M_x} \right), \\ m &= M_x (1 - e^\xi), & \frac{\partial m}{\partial \xi} &= -M_x e^\xi \\ z_0 &= r, \quad z_1 = P, \quad z_2 = T, \quad z_3 = l. \end{aligned}$$

Because the functions f_i in Eq. (C.1) only depend on the variables $y_k^{j+\frac{1}{2}}$, therefore it must hold that

$$\begin{aligned}\frac{\partial f_i}{\partial y_k^j} &= \frac{1}{2} \frac{\partial f_i}{\partial y_k^{j+\frac{1}{2}}} = \frac{\partial f_i}{\partial y_k^{j+1}}, \\ \frac{\partial G_i^j}{\partial y_i^j} &= -\frac{1}{\Delta \xi^{j+1}} - \frac{\partial f_i}{\partial y_i^j} = -\frac{1}{\Delta \xi^{j+1}} - \frac{1}{2} \frac{\partial f_i}{\partial y_i^{j+\frac{1}{2}}} = \frac{1}{\Delta \xi^{j+1}} - \frac{2}{\Delta \xi^{j+1}} - \frac{\partial f_i}{\partial y_k^{j+1}} = \frac{\partial G_i^j}{\partial y_i^{j+1}} - \frac{2}{\Delta \xi^{j+1}}, \\ \frac{\partial G_i^j}{\partial y_k^j} &= -\frac{\partial f_i}{\partial y_k^j} = -\frac{1}{2} \frac{\partial f_i}{\partial y_k^{j+\frac{1}{2}}} = -\frac{\partial f_i}{\partial y_k^{j+1}} = \frac{\partial G_i^j}{\partial y_k^{j+1}}, \quad \text{for } k \neq i,\end{aligned}$$

which means that only four derivatives per function have to be calculated.

To a certain extent, the functions G_i^j were checked against those formulated in Appendix A of Hofmeister *et al.* (1964) [56]. However, since this thesis includes an approximative treatment of rotation, which is not the case for Hofmeister *et al.* or the similar publication by Kippenhahn *et al.* (1967) [69], our functions G_1^j and G_2^j differ somewhat from theirs. To the best of my knowledge, the derivatives $\frac{\partial G_i^j}{\partial y_k^j}$ are not published anywhere and were calculated by myself in all cases.

General functions

Let us start with the radius equation f_0 (cf. Eq. (3.10a)):

$$\begin{aligned}f_0 &= \frac{\partial y_0}{\partial \xi} = -\frac{M_x}{4\pi \rho} \exp[\xi - 3y_0], \\ G_0^j &= \frac{y_0^{j+1} - y_0^j}{\Delta \xi^{j+1}} + \frac{M_x}{4\pi \rho^{j+\frac{1}{2}}} \exp\left[\xi^{j+\frac{1}{2}} - 3y_0^{j+\frac{1}{2}}\right], \\ \frac{\partial G_0^j}{\partial y_0^j} &= -\frac{1}{\Delta \xi^{j+1}} - \frac{3M_x}{8\pi \rho^{j+\frac{1}{2}}} \exp\left[\xi^{j+\frac{1}{2}} - 3y_0^{j+\frac{1}{2}}\right], \\ \frac{\partial G_0^j}{\partial y_1^j} &= -\frac{M_x}{8\pi (\rho^{j+\frac{1}{2}})^2} \exp\left[\xi^{j+\frac{1}{2}} - 3y_0^{j+\frac{1}{2}} + y_1^{j+\frac{1}{2}}\right] \frac{\partial \rho^{j+\frac{1}{2}}}{\partial P^{j+\frac{1}{2}}}, \\ \frac{\partial G_0^j}{\partial y_2^j} &= -\frac{M_x}{8\pi (\rho^{j+\frac{1}{2}})^2} \exp\left[\xi^{j+\frac{1}{2}} - 3y_0^{j+\frac{1}{2}} + y_2^{j+\frac{1}{2}}\right] \frac{\partial \rho^{j+\frac{1}{2}}}{\partial T^{j+\frac{1}{2}}}, \\ \frac{\partial G_0^j}{\partial y_3^j} &= 0.\end{aligned}\tag{C.2}$$

Next, we move on to the pressure equation f_1 (cf. Eq. (3.10b)):

$$\begin{aligned}
 f_1 &= \frac{\partial y_1}{\partial \xi} = \frac{G M_x^2}{4\pi} (1 - e^\xi) \exp[\xi - 4y_0 - y_1] - \frac{\omega^2 M_x}{6\pi} \exp[\xi - y_0 - y_1], \\
 G_1^j &= \frac{y_1^{j+1} - y_1^j}{\Delta \xi^{j+1}} - \frac{G M_x^2}{4\pi} (1 - e^{\xi^{j+\frac{1}{2}}}) \exp\left[\xi^{j+\frac{1}{2}} - 4y_0^{j+\frac{1}{2}} - y_1^{j+\frac{1}{2}}\right] \\
 &\quad + \frac{\omega^2 M_x}{6\pi} \exp\left[\xi^{j+\frac{1}{2}} - y_0^{j+\frac{1}{2}} - y_1^{j+\frac{1}{2}}\right], \\
 \frac{\partial G_1^j}{\partial y_0^j} &= \frac{G M_x^2}{2\pi} (1 - e^{\xi^{j+\frac{1}{2}}}) \exp\left[\xi^{j+\frac{1}{2}} - 4y_0^{j+\frac{1}{2}} - y_1^{j+\frac{1}{2}}\right] \\
 &\quad - \frac{\omega^2 M_x}{12\pi} \exp\left[\xi^{j+\frac{1}{2}} - y_0^{j+\frac{1}{2}} - y_1^{j+\frac{1}{2}}\right], \\
 \frac{\partial G_1^j}{\partial y_1^j} &= -\frac{1}{\Delta \xi^{j+1}} + \frac{G M_x^2}{8\pi} (1 - e^{\xi^{j+\frac{1}{2}}}) \exp\left[\xi^{j+\frac{1}{2}} - 4y_0^{j+\frac{1}{2}} - y_1^{j+\frac{1}{2}}\right] \\
 &\quad - \frac{\omega^2 M_x}{12\pi} \exp\left[\xi^{j+\frac{1}{2}} - y_0^{j+\frac{1}{2}} - y_1^{j+\frac{1}{2}}\right], \\
 \frac{\partial G_1^j}{\partial y_2^j} &= 0, \\
 \frac{\partial G_1^j}{\partial y_3^j} &= 0.
 \end{aligned} \tag{C.3}$$

Moving on to the temperature equation f_2 (cf. Eq. (3.10c)):

$$\begin{aligned}
 f_2 &= \frac{\partial y_2}{\partial \xi} = \frac{M_x}{2\pi} \exp[\xi - y_0 - y_1] \left(\frac{G M_x}{2} (1 - e^\xi) e^{-3y_0} - \frac{\omega^2}{3} \right) \nabla_T, \\
 G_2^j &= \frac{y_2^{j+1} - y_2^j}{\Delta \xi^{j+1}} - \frac{M_x}{2\pi} \exp\left[\xi^{j+\frac{1}{2}} - y_0^{j+\frac{1}{2}} - y_1^{j+\frac{1}{2}}\right] \times \\
 &\quad \times \left(\frac{G M_x}{2} (1 - e^{\xi^{j+\frac{1}{2}}}) e^{-3y_0^{j+\frac{1}{2}}} - \frac{\omega^2}{3} \right) \nabla_T^{j+\frac{1}{2}}, \\
 \frac{\partial G_2^j}{\partial y_0^j} &= \frac{M_x}{2\pi} \exp\left[\xi^{j+\frac{1}{2}} - y_0^{j+\frac{1}{2}} - y_1^{j+\frac{1}{2}}\right] \left(G M_x (1 - e^{\xi^{j+\frac{1}{2}}}) e^{-3y_0^{j+\frac{1}{2}}} - \frac{\omega^2}{6} \right) \nabla_T^{j+\frac{1}{2}}, \\
 \frac{\partial G_2^j}{\partial y_1^j} &= -\frac{M_x e^{\xi^{j+\frac{1}{2}}}}{4\pi} \left(\frac{\partial \nabla_T^{j+\frac{1}{2}}}{\partial P^{j+\frac{1}{2}}} - e^{-y_1^{j+\frac{1}{2}}} \nabla_T^{j+\frac{1}{2}} \right) \left(\frac{G M_x}{2} (1 - e^{\xi^{j+\frac{1}{2}}}) e^{-4y_0^{j+\frac{1}{2}}} - \frac{\omega^2}{3} e^{-y_0^{j+\frac{1}{2}}} \right), \\
 \frac{\partial G_2^j}{\partial y_2^j} &= -\frac{1}{\Delta \xi^{j+1}} - \frac{M_x}{4\pi} \exp\left[\xi^{j+\frac{1}{2}} - y_0^{j+\frac{1}{2}} - y_1^{j+\frac{1}{2}} + y_2^{j+\frac{1}{2}}\right] \times \\
 &\quad \times \left(\frac{G M_x}{2} (1 - e^{\xi^{j+\frac{1}{2}}}) e^{-3y_0^{j+\frac{1}{2}}} - \frac{\omega^2}{3} \right) \frac{\partial \nabla_T^{j+\frac{1}{2}}}{\partial T^{j+\frac{1}{2}}},
 \end{aligned} \tag{C.4}$$

$$\frac{\partial G_2^j}{\partial y_3^j} = -\frac{M_x}{4\pi} \exp \left[\xi^{j+\frac{1}{2}} - y_0^{j+\frac{1}{2}} - y_1^{j+\frac{1}{2}} + y_3^{j+\frac{1}{2}} \right] \times \\ \times \left(\frac{GM_x}{2} \left(1 - e^{\xi^{j+\frac{1}{2}}} \right) e^{-3y_0^{j+\frac{1}{2}}} - \frac{\omega^2}{3} \right) \frac{\partial \nabla_T^{j+\frac{1}{2}}}{\partial l^{j+\frac{1}{2}}}.$$

This presumes the simplified version of ∇_{cond} , Eq. (2.39). If, instead, the full ∇_{cond} of Eq. (2.38) is adopted, ∇ can depend on r , and the first derivative becomes:

$$\frac{\partial G_2^j}{\partial y_0^j} = -\frac{M_x e^{\xi^{j+\frac{1}{2}}}}{4\pi} \left\{ \frac{GM_x}{2} \left(1 - e^{\xi^{j+\frac{1}{2}}} \right) \exp \left[-3y_0^{j+\frac{1}{2}} - y_1^{j+\frac{1}{2}} \right] \left(\frac{\partial \nabla_T^{j+\frac{1}{2}}}{\partial r^{j+\frac{1}{2}}} - 4\nabla_T^{j+\frac{1}{2}} e^{-y_0^{j+\frac{1}{2}}} \right) \right. \\ \left. - \frac{\omega^2}{3} e^{-y_1^{j+\frac{1}{2}}} \left(\frac{\partial \nabla_T^{j+\frac{1}{2}}}{\partial r^{j+\frac{1}{2}}} - \nabla_T^{j+\frac{1}{2}} e^{-y_0^{j+\frac{1}{2}}} \right) \right\}$$

And, finally, we take the luminosity equation f_3 (cf. Eq. (3.10d)):

$$f_3 = \frac{\partial y_3}{\partial \xi} = -M_x \left(-c_p \frac{\partial T}{\partial t} + \frac{\delta_\rho}{\rho} \frac{\partial P}{\partial t} \right) \exp [\xi - y_3].$$

Similar to the mass derivative, the time derivative is approximated as the corresponding difference quotient:

$$\frac{\partial z}{\partial t} \approx \frac{z - z^*}{\Delta t},$$

where Δt is the difference between the previous time step and the current one, and z^* is the value of z from the previous time step. Thus, we arrive at:

$$G_3^j = \frac{y_3^{j+1} - y_3^j}{\Delta \xi^{j+1}} + \left(-c_p^{j+\frac{1}{2}} \underbrace{\frac{e^{y_2^{j+\frac{1}{2}}} - e^{y_2^{*j+\frac{1}{2}}}}{\Delta t}}_{\dot{T}^{j+\frac{1}{2}}} + \frac{\delta_\rho^{j+\frac{1}{2}}}{\rho^{j+\frac{1}{2}}} \underbrace{\frac{e^{y_1^{j+\frac{1}{2}}} - e^{y_1^{*j+\frac{1}{2}}}}{\Delta t}}_{\dot{P}^{j+\frac{1}{2}}} \right) \times \quad (\text{C.5}) \\ \times M_x \exp \left[\xi^{j+\frac{1}{2}} - y_3^{j+\frac{1}{2}} \right]$$

$$\frac{\partial G_3^j}{\partial y_0^j} = 0,$$

$$\frac{\partial G_3^j}{\partial y_1^j} = \left(-\frac{\partial c_p^{j+\frac{1}{2}}}{\partial P^{j+\frac{1}{2}}} \dot{T}^{j+\frac{1}{2}} + \frac{1}{\rho^{j+\frac{1}{2}}} \dot{P}^{j+\frac{1}{2}} \left(\frac{\partial \delta_\rho^{j+\frac{1}{2}}}{\partial P^{j+\frac{1}{2}}} - \frac{\delta_\rho^{j+\frac{1}{2}}}{\rho^{j+\frac{1}{2}}} \frac{\partial \rho^{j+\frac{1}{2}}}{\partial P^{j+\frac{1}{2}}} \right) + \frac{\delta_\rho^{j+\frac{1}{2}}}{\rho^{j+\frac{1}{2}} \Delta t} \right) \times \\ \times \frac{M_x}{2} \exp \left[\xi^{j+\frac{1}{2}} - y_3^{j+\frac{1}{2}} + y_1^{j+\frac{1}{2}} \right],$$

$$\begin{aligned} \frac{\partial G_3^j}{\partial y_2^j} &= \left\{ -\frac{\partial c_p^{j+\frac{1}{2}}}{\partial T^{j+\frac{1}{2}}} \dot{T}^{j+\frac{1}{2}} - \frac{c_p^{j+\frac{1}{2}}}{\Delta t} + \frac{1}{\rho^{j+\frac{1}{2}}} \dot{P}^{j+\frac{1}{2}} \left(\frac{\partial \delta_\rho^{j+\frac{1}{2}}}{\partial T^{j+\frac{1}{2}}} - \frac{\delta_\rho^{j+\frac{1}{2}}}{\rho^{j+\frac{1}{2}}} \frac{\partial \rho^{j+\frac{1}{2}}}{\partial T^{j+\frac{1}{2}}} \right) \right\} \times \\ &\quad \times \frac{M_x}{2} \exp \left[\xi^{j+\frac{1}{2}} - y_3^{j+\frac{1}{2}} + y_2^{j+\frac{1}{2}} \right], \\ \frac{\partial G_3^j}{\partial y_3^j} &= -\frac{1}{\Delta \xi^{j+1}} - \frac{M_x}{2} \left(-c_p^{j+\frac{1}{2}} \dot{T}^{j+\frac{1}{2}} + \frac{\delta_\rho^{j+\frac{1}{2}}}{\rho^{j+\frac{1}{2}}} \dot{P}^{j+\frac{1}{2}} \right) \exp \left[\xi^{j+\frac{1}{2}} - y_3^{j+\frac{1}{2}} \right] \end{aligned}$$

Outer boundary conditions

The first outer boundary condition is Eq. (3.3)

$$\begin{aligned} P(M_p) &= 1 \text{ bar} := P_0, \\ B_0 &= \exp [y_1^0] - P_0 = 0, \\ \frac{\partial B_0}{\partial y_0^0} &= 0, \\ \frac{\partial B_0}{\partial y_1^0} &= \exp [y_1^0], \\ \frac{\partial B_0}{\partial y_2^0} &= 0, \\ \frac{\partial B_0}{\partial y_3^0} &= 0. \end{aligned} \tag{C.6}$$

The second outer boundary condition is a little more involved. Eq. (3.7) says

$$l(M_p) = 4\pi R^2 \sigma_B T_{\text{eff}}^4 - L_{\text{sol}}, \tag{C.7}$$

with (see Eqs. (3.9) and (3.6))

$$\begin{aligned} L_{\text{sol}} &= 4\pi R^2 \sigma_B T_{\text{eq}}^4, \\ T_{1\text{bar}} &= K g^{-1/6} T_{\text{eff}}^{3.73/3}, \\ T_{\text{eff}}^4 &= K^{-12/3.73} g^{2/3.73} T_{1\text{bar}}^{12/3.73} = K^{-12/3.73} T_{1\text{bar}}^{12/3.73} \left(\frac{GM_p}{R^2} \right)^{2/3.73}. \end{aligned}$$

Note, that as per Eq. (3.8) T_{eq} is a function of the star's properties, the planet's orbital distance, and its albedo, and it is thus constant with respect to our four primary

variables. With this, Eq. (C.7) can be rewritten as

$$\begin{aligned}
L_{\text{int}} = l(M_{\text{P}}) &= 4\pi R^2 \sigma_{\text{B}} (T_{\text{eff}}^4 - T_{\text{eq}}^4) = 4\pi R^2 \sigma_{\text{B}} T_{\text{eff}}^4 \left(1 - \frac{T_{\text{eq}}^4}{T_{\text{eff}}^4}\right), \\
\ln l(M_{\text{P}}) &= \ln(e^{y_3^0} - L_{\text{c}}) = \ln(4\pi\sigma_{\text{B}}) + 2y_0^0 + 4 \ln T_{\text{eff}} + \ln\left(1 - \frac{T_{\text{eq}}^4}{T_{\text{eff}}^4}\right) \\
0 &= -\ln(e^{y_3^0} - L_{\text{c}}) + \ln(4\pi\sigma_{\text{B}}) + \frac{2}{3.73} \ln(GMK^{-6}) + \ln\left(1 - \frac{T_{\text{eq}}^4}{T_{\text{eff}}^4}\right) \\
&\quad + 2y_0^0 - \frac{4}{3.73}y_0^0 + \frac{12}{3.73}y_2^0
\end{aligned}$$

And therefore, the second outer boundary condition is

$$B_1 = \ln(4\pi\sigma_{\text{B}}) + \frac{2}{3.73} \ln(GMK^{-6}) + \frac{3.46}{3.73}y_0^0 + \frac{12}{3.73}y_2^0 - \ln(e^{y_3^0} - L_{\text{c}}) + \ln\left(1 - \frac{T_{\text{eq}}^4}{T_{\text{eff}}^4}\right) \tag{C.8}$$

$$\frac{\partial B_1}{\partial y_0^0} = \frac{3.46}{3.73} - \frac{4}{3.73} \frac{1}{\frac{T_{\text{eff}}^4}{T_{\text{eq}}^4} - 1}$$

$$\frac{\partial B_1}{\partial y_1^0} = 0$$

$$\frac{\partial B_1}{\partial y_2^0} = \frac{12}{3.73} + \frac{12}{3.73} \frac{1}{\frac{T_{\text{eff}}^4}{T_{\text{eq}}^4} - 1}$$

$$\frac{\partial B_1}{\partial y_3^0} = -\frac{e^{y_3^0}}{e^{y_3^0} - L_{\text{c}}}$$

Central equations

As discussed in Sect. 3.2, the functions between the last and second-to-last mass point differ from the general equations, so different derivatives have to be calculated for those as well. As a reminder, since the values of y_0^{N-1} and y_3^{N-1} are fixed by the inner boundary condition, they are not considered unknown variables in this description and the derivatives with respect to them do not have to be calculated (see Sect. 3.2).

We start with the first central equation, given by (3.15), with the central density $\rho_c =$

$\rho(P^{N-1}, T^{N-1})$:

$$\begin{aligned}
 C_0 &= 3y_0^{N-2} - \ln\left(\frac{3}{4\pi}\right) + \ln(\rho_c) - \ln\left(M_x(1 - e^{\xi^{N-2}})\right) & (C.9) \\
 \frac{\partial C_0}{\partial y_0^{N-2}} &= 3 \\
 \frac{\partial C_0}{\partial y_1^{N-2}} &= 0 \\
 \frac{\partial C_0}{\partial y_2^{N-2}} &= 0 \\
 \frac{\partial C_0}{\partial y_3^{N-2}} &= 0 \\
 \frac{\partial C_0}{\partial y_1^{N-1}} &= \frac{1}{\rho_c} e^{y_1^{N-1}} \frac{\partial \rho_c}{\partial P^{N-1}} \\
 \frac{\partial C_0}{\partial y_2^{N-1}} &= \frac{1}{\rho_c} e^{y_2^{N-1}} \frac{\partial \rho_c}{\partial T^{N-1}}.
 \end{aligned}$$

Next, we turn to C_1 , given by Eq. (3.17):

$$\begin{aligned}
 C_1 &= \frac{y_1^{N-1} - y_1^{N-2}}{\xi^{N-1} - \xi^{N-2}} - \frac{1}{6\pi} \left(\frac{4\pi}{3}\right)^{\frac{1}{3}} M_x^{\frac{2}{3}} (1 - e^{\xi^{N-2}})^{-\frac{1}{3}} \times & (C.10) \\
 &\quad \times \exp[\xi^{N-2} - y_1^{N-2}] \left(2\pi G \rho_c^{\frac{4}{3}} - \omega^2 \rho_c^{\frac{1}{3}}\right) \\
 \frac{\partial C_0}{\partial y_0^{N-2}} &= 0 \\
 \frac{\partial C_0}{\partial y_1^{N-2}} &= -\frac{1}{\Delta \xi^{N-1}} + \frac{1}{6\pi} \left(\frac{4\pi}{3} \rho_c\right)^{\frac{1}{3}} M_x^{\frac{2}{3}} (1 - e^{\xi^{N-2}})^{-\frac{1}{3}} \times \\
 &\quad \times \exp[\xi^{N-2} - y_1^{N-2}] (2\pi G \rho_c - \omega^2) \\
 \frac{\partial C_0}{\partial y_2^{N-2}} &= 0 \\
 \frac{\partial C_0}{\partial y_3^{N-2}} &= 0 \\
 \frac{\partial C_1}{\partial y_1^{N-1}} &= \frac{1}{\Delta \xi^{N-1}} - \frac{1}{18\pi} \left(\frac{4\pi}{3} \rho_c\right)^{\frac{1}{3}} M_x^{\frac{2}{3}} (1 - e^{\xi^{N-2}})^{-\frac{1}{3}} \times \\
 &\quad \times \exp[\xi^{N-2} - y_1^{N-2}] P^{N-1} \left(8\pi G - \frac{\omega^2}{\rho_c}\right) \frac{\partial \rho_c}{\partial P^{N-1}} \\
 \frac{\partial C_1}{\partial y_2^{N-1}} &= \frac{1}{\Delta \xi^{N-1}} - \frac{1}{18\pi} \left(\frac{4\pi}{3} \rho_c\right)^{\frac{1}{3}} M_x^{\frac{2}{3}} (1 - e^{\xi^{N-2}})^{-\frac{1}{3}} \times \\
 &\quad \times \exp[\xi^{N-2} - y_1^{N-2}] T^{N-1} \left(8\pi G - \frac{\omega^2}{\rho_c}\right) \frac{\partial \rho_c}{\partial T^{N-1}}.
 \end{aligned}$$

Third, we take a look at C_2 , given by Eq. (3.18):

$$\begin{aligned}
C_2 &= \frac{y_2^{N-1} - y_2^{N-2}}{y_1^{N-1} - y_1^{N-2}} - \nabla_T^{N-\frac{3}{2}} & (C.11) \\
\frac{\partial C_2}{\partial y_0^{N-2}} &= -\frac{1}{2} r^{N-\frac{3}{2}} \frac{\partial \nabla_T^{N-\frac{3}{2}}}{\partial r^{N-\frac{3}{2}}} \\
\frac{\partial C_2}{\partial y_1^{N-2}} &= \frac{y_2^{N-1} - y_2^{N-2}}{(y_1^{N-1} - y_1^{N-2})^2} - \frac{1}{2} P^{N-\frac{3}{2}} \frac{\partial \nabla_T^{N-\frac{3}{2}}}{\partial P^{N-\frac{3}{2}}} \\
\frac{\partial C_2}{\partial y_2^{N-2}} &= -\frac{1}{y_1^{N-1} - y_1^{N-2}} - \frac{1}{2} T^{N-\frac{3}{2}} \frac{\partial \nabla_T^{N-\frac{3}{2}}}{\partial T^{N-\frac{3}{2}}} \\
\frac{\partial C_2}{\partial y_3^{N-2}} &= -\frac{1}{2} e^{y_3^{N-\frac{3}{2}}} \frac{\partial \nabla_T^{N-\frac{3}{2}}}{\partial t^{N-\frac{3}{2}}} \\
\frac{\partial C_2}{\partial y_1^{N-1}} &= -\frac{y_2^{N-1} - y_2^{N-2}}{(y_1^{N-1} - y_1^{N-2})^2} - \frac{1}{2} P^{N-\frac{3}{2}} \frac{\partial \nabla_T^{N-\frac{3}{2}}}{\partial P^{N-\frac{3}{2}}} \\
\frac{\partial C_2}{\partial y_2^{N-1}} &= \frac{1}{y_1^{N-1} - y_1^{N-2}} - \frac{1}{2} T^{N-\frac{3}{2}} \frac{\partial \nabla_T^{N-\frac{3}{2}}}{\partial T^{N-\frac{3}{2}}}.
\end{aligned}$$

Finally, since function C_3 is equal to the general function G_3^j with $j = N - 2$, for C_3 I simply refer to Eq. (C.5) and the derivatives calculated there.

Appendix D.

Effect of radioactive decay on the thermal evolution

My models do not include contributions from nuclear reactions to the planetary luminosity. In order to assess their potential influence I have performed test calculations with a modified luminosity equation. Different from Eq. (2.25), these expanded models use the equation

$$\frac{\partial l}{\partial m} = c_p \frac{\partial T}{\partial t} + \frac{\delta_\rho}{\rho} \frac{\partial P}{\partial t} + \underbrace{\frac{\partial l_{\text{radio}}}{\partial m}}_{\varepsilon}. \quad (\text{D.1})$$

The additional term ε represents the additional heating from nuclear reactions, following the practice of Ref. [70]. I use the approximation of Guillot *et al.* (1995) [44], who estimate the total luminosity from radioactive decay L_{radio} from a rock core, based on the concentration of radioactive elements in the Earth, to be

$$L_{\text{radio}} = 2 \times 10^{13} \text{ W} \frac{m_{\text{core}}}{M_{\text{E}}}, \quad (\text{D.2})$$

with m_{core} the core mass in the planet. Because the models in Ref. [44] contain no rocks outside the core, while some of my models have rock mixed into the inner envelope, I generalise this approximation to use the total mass of rocks in the model m_{rocks} instead of m_{core} . Assuming for ease of use that this value stays roughly the same over time, and that generation of this radiogenic luminosity is just dependent on available rock mass and not the thermodynamic conditions, we arrive at an approximation for ε :

$$\varepsilon = \frac{\partial l_{\text{radio}}}{\partial m} = Z_{\text{rocks}} \times 2 \times 10^{13} \text{ W} \frac{1}{M_{\text{E}}} = Z_{\text{rocks}} \times 3.35 \times 10^{-12} \text{ W kg}^{-1}, \quad (\text{D.3})$$

where Z_{rocks} is the local mass fraction of rocks in the respective mass shell.

I have performed these calculations for two Uranus models; the first is the one designated “Uranus 2” in Chap. 5, which is an adiabatic 3-layer-model with a core mass of $m_{\text{core}} = 0.79 M_{\text{E}}$ and no other rocky material in the mantle. The other is the model covered in Sect. 6.6, which is a model with a thermal boundary layer between outer and inner envelope. It features a rock core of $m_{\text{core}} = 0.15 M_{\text{E}}$ and a rock mass fraction of $Z_{\text{rocks}} = 0.18$, bringing its total amount of rock to $m_{\text{rocks}} = 2.5 M_{\text{E}}$. The evolution tracks for both models with and without nuclear reactions are shown in Fig. D.1. For both models, both considering and neglecting nuclear reactions produce evolution curves that are indistinguishable from one another. Specifically, the evolution curves with and without ε for the TBL model differ by less than 5×10^{-3} K after 5 Gyr. This is likely because the TBL acts as a strong barrier on the heat released from the inner envelope, where the rocks and therefore the radiogenic heat sources are located, making it very difficult for their contribution to affect the visible evolution. In case of the adiabatic models, their the T_{eff} values with and without ε differ by about 0.01 K after 5 Gyr, which results in a cooling time difference of under 70 Myr.

However, when interpreting these results we must consider that the adiabatic models of this work have a very low rock content. As discussed in Sect. 4.1, the use of water as a proxy for all heavy elements in the planet’s envelope is a simplification in these models, and a higher amount of rock material than assumed here would also be realistic. Nettelmann *et al.* (2016) [102] have found that raising the rock content of Uranus models leads to longer substantially longer cooling times because of the extra heating due to nuclear reactions in the rocks, while for their Neptune models with their higher overall luminosity, the cooling time is affected little by the addition of rocks.

So while the models presented here are not majorly affected by radiogenic heating, it is an important thing to consider for more rock-rich planets and to keep in mind when evaluating the uncertainties in terms of composition of the adiabatic models presented in Chap. 5.

In any case, the influence of ε in these test cases is very low compared to the other factors considered in this work and we can be reassured that neglecting them does not impact the conclusions of this work.

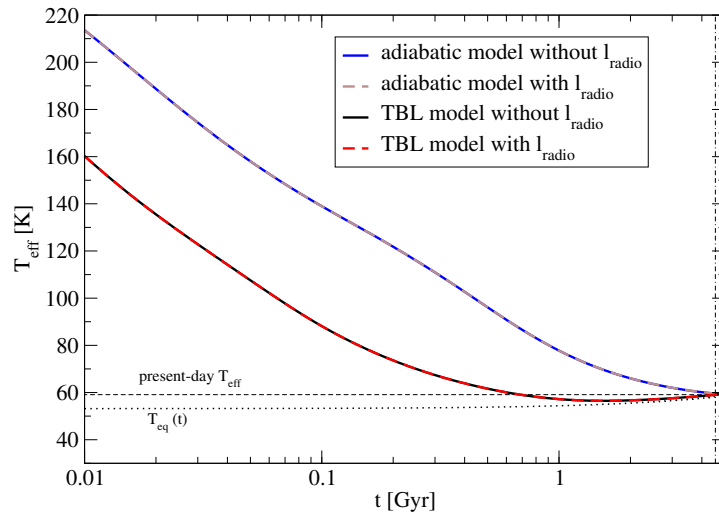


Fig. D.1.: Comparison of evolution tracks for two Uranus models each with and without considering the effect of nuclear reactions on the luminosity. The adiabatic model is the one designated “Uranus 2” in Sect. 5.1, the TBL model is a rock-rich model covered in Sect. 6.6 and marked in Fig. 6.10 b). In both cases, the T_{eff} with and without considering l_{radio} differ by less than 0.03 K after 5 Gyr.

Appendix E.

Effect of rotational term on the conductive gradient

As established in Sect. 2.2.2, the conductive temperature gradient is

$$\nabla_{\text{cond}} = \frac{lP}{4\pi G m \lambda \rho T} \left(1 - \frac{2\omega^2 r^3}{3G m}\right)^{-1}, \quad (\text{E.1})$$

while the models featuring a thermal boundary layer in Chap. 6 were calculated using the simplified version

$$\nabla_{\text{cond}} = \frac{lP}{4\pi G m \lambda \rho T}. \quad (\text{E.2})$$

The additional term in parenthesis in (E.1) represents the relative influence of rotation on this quantity. This term is plotted over the mass coordinate in Fig. E.1 for two different Neptune models at very young times. Since it is proportional to r^3 and inversely proportional to m , it is largest at the planet's outer edge, and shrinks monotonically towards the centre. The effect is larger for the model with an inner envelope metallicity of $Z_2 = 92\%$ than for the other models because it has a smaller density and therefore a larger radius. Since the outer envelope is always assumed to be adiabatic, the point where the deviation has the highest value and while being relevant is the outer edge of the TBL.

Consequently, Fig. E.2 shows the evolution of the rotation term in ∇_{cond} at the top of the TBL with time, again for different Neptune models. The term is largest at the start of the evolution, while the planet is still extended and r large, and shrinks with time. At all times it is below 1.5% for all models considered.

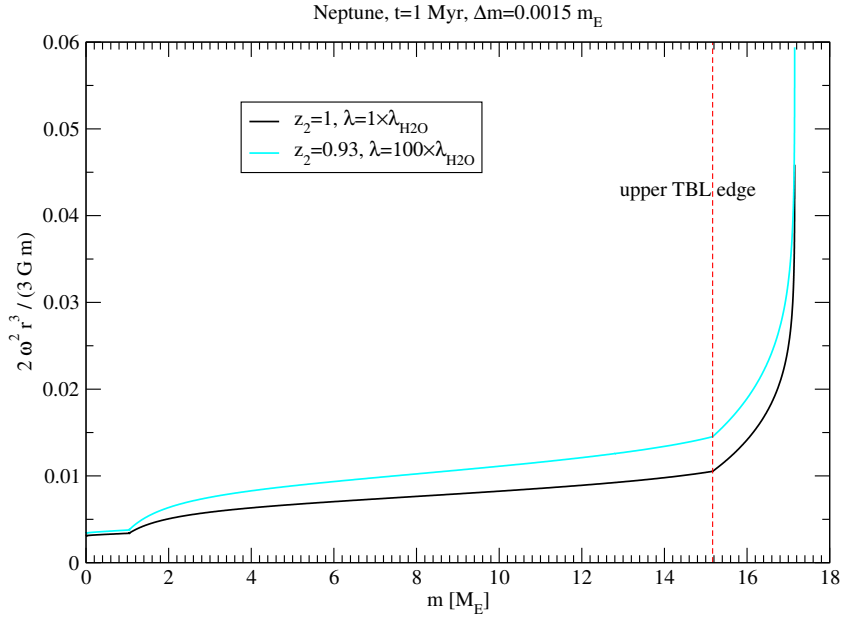


Fig. E.1.: Magnitude of the second addend in ∇_{cond} Eq. (2.38) over mass for two example Neptune TBL models from Chap. 6 with $\Delta m = 0.0015 M_E$, one with $Z_2 = 1$ and $\lambda = \lambda_{\text{H}_2\text{O}}$ and one with $Z_2 = 0.93$ and $\lambda = 100 \times \lambda_{\text{H}_2\text{O}}$. The term is largest on the planet's surface and gets successively smaller deeper in the planet.

Finally, to see an example of the effect this has on the evolution curve, Fig. E.3 shows the evolution of T_{eff} for the Neptune model considered in Sect. 6.6, chosen because it fulfills both the observed T_{eff} and R_p at $t = 4.6 \text{ Gyr}$, both with and without the rotation term in ∇_{cond} . Neglecting it introduces a deviation of less than 0.1 K in T_{eff} after 5 Gyr in this test case.

Thus, while the effect is noticeable under close inspection, we can be reasonable certain that it does not impact the conclusions for ice giant models with thermal barriers presented in this work.

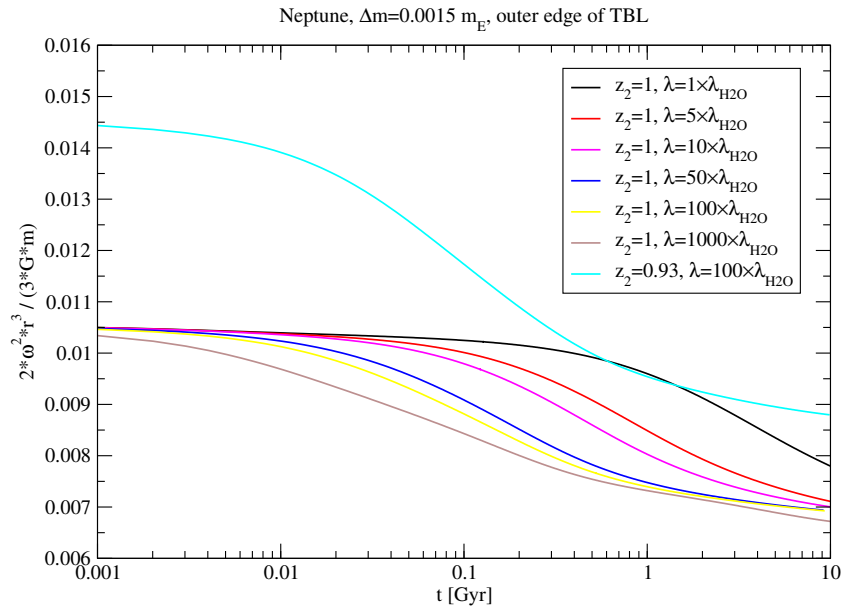


Fig. E.2.: Magnitude of the second addend in ∇_{cond} Eq. (2.38) at the outer edge of the TBL over time for all Neptune TBL models from Chap. 6 with $\Delta m = 0.0015 M_E$. It is smaller than 1.5 % at all times even for the model with the highest influence.

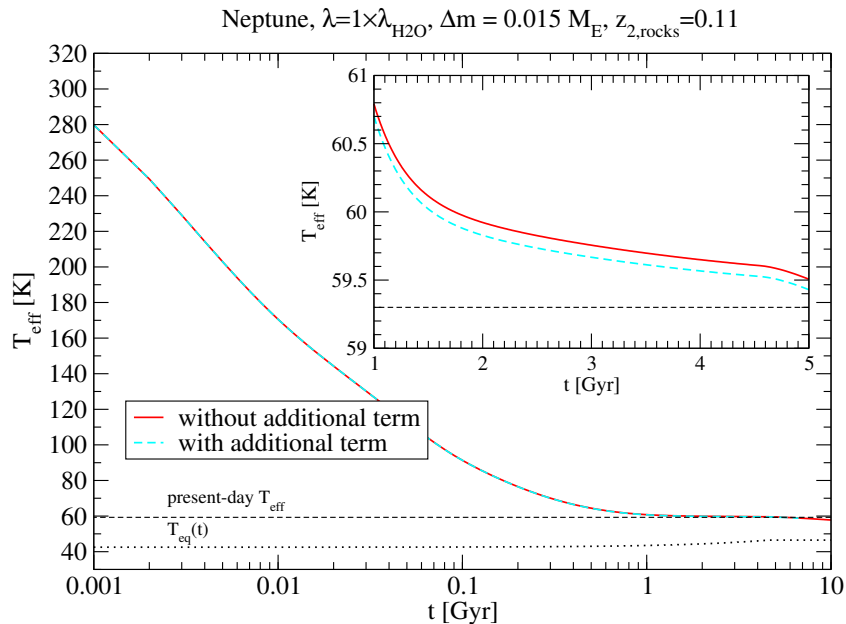


Fig. E.3.: Comparison of evolution tracks with and without the additional addend in ∇_{cond} , which is Eqs. (2.38) and (2.39) for an example model from Chap. 6. The calculations differ by less than 0.1 K even after 5 Gyr.

Bibliography

- [1] B. J. Alder and T. E. Wainwright. “Studies in Molecular Dynamics. I. General Method”. In: *The Journal of Chemical Physics* 31 (1959), pp. 459–466.
- [2] J. D. Anderson, J. K. Campbell, R. A. Jacobson, D. N. Sweetnam, and A. H. Taylor. “Radio Science With Voyager 2 at Uranus: Results on Masses and Densities of the Planet and Five Principal Satellite”. In: *Journal of Geophysical Research* 92 (1987), pp. 14877–14883.
- [3] J. N. Bahcall and M. H. Pinsonneault. “Solar models with helium and heavy-element diffusion”. In: *Reviews of Modern Physics* 67 (1995), pp. 781–808.
- [4] E. Bailey and D. J. Stevenson. “Thermodynamically Governed Interior Models of Uranus and Neptune”. In: *The Planetary Science Journal* 2 (2021), p. 64.
- [5] J. F. Barnes and S. P. Lyon. *SESAME Equation of State Number 7530, Basalt*. Tech. rep. LA-U253-M. Los Alamos, New Mexico 87545: Los Alamos National Laboratory, 1988.
- [6] K. Batygin and D. J. Stevenson. “Inflating hot Jupiters with Ohmic dissipation”. In: *The Astrophysical Journal Letters* 714 (2010), pp. L238–L243.
- [7] A. Becker, W. Lorenzen, J. J. Fortney, N. Nettelmann, M. Schöttler, and R. Redmer. “Ab initio equations of state for Hydrogen (H-REOS.3) and Helium (He-REOS.3) and their implications for the interior of brown dwarfs”. In: *The Astrophysical Journal Supplement Series* 215 (2014), pp. 21–35.
- [8] A. Bergermann, M. French, and R. Redmer. “Gibbs-ensemble Monte Carlo simulation of H₂-H₂O mixtures”. In: *Physical Chemistry Chemical Physics* 23 (2021), pp. 12637–12643.
- [9] M. Bethkenhagen, E. R. Meyer, S. Hamel, N. Nettelmann, M. French, L. Scheibe, C. Ticknor, L. A. Collins, et al. “Planetary Ices and the Linear Mixing Approximation”. In: *The Astrophysical Journal* 848 (2017), p. 67.

- [10] M. Born and R. Oppenheimer. “Zur Quantentheorie der Molekeln”. In: *Annalen der Physik* 389 (1927), pp. 457–484.
- [11] I. N. Bronstein, K. A. Semandjajew, G. Musiol, and H. Mühlig. *Taschenbuch der Mathematik*. 10. Auflage. Haan-Gruiten: Verlag Europa-Lehrmittel, 2016.
- [12] M. Brozović, M. R. Showalter, R. A. Jacobson, R. S. French, J. J. Lissauer, and I. de Pater. “Orbits and resonances of the regular moons of Neptune”. In: *Icarus* 338 (2020), p. 113462.
- [13] D. Cebulla and R. Redmer. “Ab initio simulations of MgO under extreme conditions”. In: *Physical Review B* 89 (2014), p. 134107.
- [14] G. Chabrier, S. Mazevet, and F. Soubiran. “A New Equation of State for Dense Hydrogen-Helium Mixtures”. In: *The Astrophysical Journal* 872 (2019), p. 51.
- [15] G. Chabrier and A. Y. Potekhin. “Equation of state of fully ionized electron-ion plasmas”. In: *Physical Review E* 58 (1998), p. 4941.
- [16] R. Chau, S. Hamel, and W. J. Nellis. “Chemical processes in the deep interior of Uranus”. In: *Nature Communications* 2 (2011), p. 203.
- [17] R. C. Clay, J. Mcminis, J. M. McMahon, C. Pierleoni, D. M. Ceperley, and M. A. Morales. “Benchmarking exchange-correlation functionals for hydrogen at high pressures using quantum Monte Carlo”. In: *Physical Review B* 89 (2014), p. 184106.
- [18] J. E. P. Connerney. “Magnetic fields of the outer planets”. In: *Journal of Geophysical Research* 98 (1993), pp. 18659–18679.
- [19] W. C. DeMarcus. “The constitution of Jupiter and Saturn”. In: *The Astronomical Journal* 63 (1958), p. 2.
- [20] W. Demtröder. *Experimentalphysik 1 - Mechanik und Wärme*. 4. Auflage. Berlin Heidelberg: Springer-Verlag, 2006.
- [21] J. F. Encke. “Schreiben des Herrn Professors Encke an den Herausgeber”. In: *Astronomische Nachrichten* 25 (1846), p. 49.
- [22] G. G. Fazio, W. A. Traub, E. L. Wright, F. J. Low, and L. Trafton. “The effective temperature of Uranus”. In: *The Astrophysical Journal* 209 (1976), pp. 633–637.

- [23] L. N. Fletcher, A. A. Simon, M. D. Hofstadter, C. S. Arridge, I. J. Cohen, A. Masters, K. Mandt, and A. Coustenis. “Ice giant system exploration in the 2020s: an introduction”. In: *Philosophical Transactions of the Royal Society A: Mathematical, Physical and Engineering Sciences* 378 (2020), p. 20190473.
- [24] J. J. Fortney, M. Ikoma, N. Nettelmann, T. Guillot, and M. S. Marley. “Self-consistent model atmospheres and the cooling of the solar system’s giant planets”. In: *The Astrophysical Journal* 729 (2011), p. 32.
- [25] J. J. Fortney, R. I. Dawson, and T. D. Komacek. “Hot Jupiters: Origins, Structure, Atmospheres”. In: *Journal of Geophysical Research: Planets* 126 (2021), e2020JE006629.
- [26] W. M. C. Foulkes, L. Mitas, R. J. Needs, and G. Rajagopal. “Quantum Monte Carlo simulations of solids”. In: *Reviews of Modern Physics* 73 (2001), p. 33.
- [27] R. Freikh and R. A. Murray-Clay. “The Formation of Uranus and Neptune: Fine-tuning in Core Accretion”. In: *The Astrophysical Journal* 154 (2017), p. 98.
- [28] M. French. “Ab-initio-Berechnung von Transporteigenschaften von warmer dichter Materie”. Habilitation thesis (submitted). Universität Rostock, 2021.
- [29] M. French. “Thermal conductivity of dissociating water – an ab initio study”. In: *New Journal of Physics* 21 (2019), p. 023007.
- [30] M. French, A. Becker, W. Lorenzen, N. Nettelmann, M. Bethkenhagen, J. Wicht, and R. Redmer. “Ab initio simulations for material properties along the Jupiter adiabat”. In: *The Astrophysical Journal Supplement Series* 202 (2012), p. 5.
- [31] M. French, M. P. Desjarlais, and R. Redmer. “Ab initio calculation of thermodynamic potentials and entropies for superionic water”. In: *Physical Review E* 93 (2016), p. 022140.
- [32] M. French, T. R. Mattsson, N. Nettelmann, and R. Redmer. “Equation of state and phase diagram of water at ultrahigh pressures as in planetary interiors”. In: *Physical Review B* 79 (2009), p. 054107.
- [33] M. French, T. R. Mattsson, and R. Redmer. “Diffusion and electrical conductivity in water at ultrahigh pressures”. In: *Physical Review B* 82 (2010), p. 174108.
- [34] M. French and N. Nettelmann. “Viscosity and Prandtl Number of Warm Dense Water as in Ice Giant Planets”. In: *The Astrophysical Journal* 881 (2019), p. 81.
- [35] M. French and R. Redmer. “Electronic transport in partially ionized water plasmas”. In: *Physics of Plasmas* 24 (2017), p. 092306.

- [36] M. French and R. Redmer. “Estimating the quantum effects from molecular vibrations of water under high pressures and temperatures”. In: *Journal of Physics: Condensed Matter* 21 (2009), p. 375101.
- [37] A. J. Friedson and E. Gonzales. “Inhibition of ordinary and diffusive convection in the water condensation zone of the ice giants and implications for their thermal evolution”. In: *Icarus* 297 (2017), p. 160.
- [38] B. J. Fulton, E. A. Petigura, A. W. Howard, H. Isaacson, G. W. Marcy, P. A. Cargile, L. Hebb, L. M. Weiss, et al. “The California-KeplerSurvey. III. A Gap in the Radius Distribution of Small Planets”. In: *The Astronomical Journal* 154 (2017), p. 109.
- [39] P. Garaud. “Double-Diffusive Convection at Low Prandtl Number”. In: *Annual Review of Fluid Mechanics* 50 (2018), pp. 275–298.
- [40] P. Goldreich, N. Murray, P. Y. Longaretti, and D. Banfield. “Neptune’s Story”. In: *Science* 245 (1989), pp. 500–504.
- [41] H. C. Graboske, J. B. Pollack, A. S. Grossman, and R. J. Olness. “The structure and evolution of Jupiter: the fluid contraction stage”. In: *The Astrophysical Journal* 199 (1975), p. 265.
- [42] F. Grasselli, L. Stixrude, and S. Baroni. “Heat and charge transport in H₂O at ice-giant conditions from ab initio molecular dynamics simulations”. In: *Nature Communications* 11 (2020), p. 3605.
- [43] G. Guennebaud, B. Jacob, et al. *Eigen v. 3.3.2*. <http://eigen.tuxfamily.org>. 2010.
- [44] T. Guillot, G. Chabrier, D. Gautier, and P. Morel. “Effect of Radiative Transport on the Evolution of Jupiter and Saturn”. In: *The Astrophysical Journal* 450 (1995), pp. 463–472.
- [45] T. Guillot and D. Gautier. “10.16 - Giant Planets”. In: *Treatise on Geophysics (Second Edition)*. Ed. by G. Schubert. Second Edition. Oxford: Elsevier, 2015, pp. 529–557. ISBN: 978-0-444-53803-1.
- [46] T. Guillot, D. J. Stevenson, W. B. Hubbard, and D. Saumon. “The interior of Jupiter”. In: *Jupiter: The Planet, Satellites and Magnetosphere*. Ed. by F. Baganal, T. E. Dowling, and W. B. McKinnon. Cambridge University Press, 2004. Chap. 3.

- [47] M. Haberreiter, W. Schmutz, and A. G. Kosovichev. “Solving the Discrepancy between the Seismic and Photospheric Solar Radius”. In: *The Astrophysical Journal Letters* 675 (2008), p. L53.
- [48] R. Helled, J. D. Anderson, M. Podolak, and G. Schubert. “Interior Models of Uranus and Neptune”. In: *The Astrophysical Journal* 726 (2011), p. 15.
- [49] R. Helled, J. D. Anderson, and G. Schubert. “Uranus and Neptune: Shape and rotation”. In: *Icarus* 210 (2010), pp. 446–454.
- [50] R. Helled and J. J. Fortney. “The interiors of Uranus and Neptune: current understanding and open questions”. In: *Philosophical Transactions of the Royal Society A* 378 (2020), p. 20190474.
- [51] R. Helled, G. Mazzola, and R. Redmer. “Understanding dense hydrogen at planetary conditions”. In: *Nature Reviews Physics* 2 (2020), pp. 562–574.
- [52] R. Helled, N. Nettelmann, and T. Guillot. “Uranus and Neptune: Origin, Evolution and Internal Structure”. In: *Space Science Reviews* 216 (2020), p. 38.
- [53] R. Helled and D. Stevenson. “The Fuzziness of Giant Planet’s Cores”. In: *The Astrophysical Journal* 840 (2017), p. L4.
- [54] L. G. Henyey, J. E. Forbes, and N. L. Gould. “A new method of automatic computation of stellar evolution”. In: *Astrophysical Journal* 139 (1964), p. 306.
- [55] W. Herschel. “XXXII. Account of a comet”. In: *Philosophical Transactions of the Royal Society* 71 (1781), pp. 491–501.
- [56] E. Hofmeister, R. Kippenhahn, and A. Weigert. “Sternentwicklung I - Ein Programm zur Lösung der zeitabhängigen Aufbaugleichungen”. In: *Zeitschrift für Astrophysik* 59 (1964), pp. 215–241.
- [57] M. Hofstadter, A. Simon, S. Atreya, D. Banfield, J. J. Fortney, A. Hayes, M. Hedman, G. Hospodarsky, et al. “Uranus and Neptune missions: A study in advance of the next Planetary Science Decadal Survey”. In: *Planetary and Space Science* 177 (2019), p. 104680.
- [58] P. Hohenberg and W. Kohn. “Inhomogeneous Electron Gas”. In: *Physical Review* 136 (1964), B864–B871.
- [59] B. Holst, M. French, and R. Redmer. “Electronic transport coefficients from ab initio simulations and application to dense liquid hydrogen”. In: *Physical Review B: Condensed Matter and Materials Physics* 83 (2011), p. 235120.

- [60] B. Holst, N. Nettelmann, and R. Redmer. “Equation of State for Dense Hydrogen and Plasma Phase Transition”. In: *Contributions to Plasma Physics* 47 (2007), pp. 368–374.
- [61] D. C. Hsu, E. B. Ford, D. Ragozzine, and K. Ashby. “Occurrence Rates of Planets Orbiting FGK Stars: Combining Kepler DR25, Gaia DR2, and Bayesian Inference”. In: *The Astronomical Journal* 158 (2019), p. 109.
- [62] W. B. Hubbard and J. J. MacFarlane. “Structure and Evolution of Uranus and Neptune”. In: *Journal of Geophysical Research* 85 (1980), pp. 225–234.
- [63] W. B. Hubbard. “The Jovian Surface Condition and Cooling Rate”. In: *Icarus* 30 (1977), p. 305.
- [64] W. B. Hubbard, M. Podolak, and D. J. Stevenson. “The interior of Neptune”. In: *Neptune and Triton*. Ed. by D. P. Cruikshank. Tucson: The University of Arizona Press, 1995. Chap. 4, pp. 109–135.
- [65] R. A. Jacobson. “The orbits of the Neptunian satellites and the orientation of the pole of Neptune”. In: *The Astronomical Journal* 137 (2009), pp. 4322–4329.
- [66] R. A. Jacobson. “The orbits of the Uranian satellites and rings, the gravity field of the Uranian system, and the orientation of the pole of Uranus”. In: *The Astronomical Journal* 148 (2014), p. 76.
- [67] H. Kadobayashi, S. Ohnishi, H. Ohfuji, Y. Yamamoto, M. Muraoka, S. Yoshida, N. Hirao, S. Kawaguchi-Imada, and H. Hirai. “Diamond formation from methane hydrate under the internal conditions of giant icy planets”. In: *Scientific Reports* 11 (2021), p. 8165.
- [68] T. Kim, S. Chariton, V. Prakapenka, A. Pakhomova, H.-P. Liermann, Z. Liu, S. Speziale, S.-H. Shim, and Y. Lee. “Atomic-scale mixing between MgO and H₂O in the deep interiors of water-rich planets”. In: *Nature Astronomy* 5 (2021), pp. 815–821.
- [69] R. Kippenhahn, A. Weigert, and E. Hofmeister. “Methods for Calculating Stellar Evolution”. In: *Methods in Computational Physics* 7 (1967), pp. 129–190.
- [70] R. Kippenhahn, A. Weigert, and A. Weiss. *Stellar Structure and Evolution*. 2nd Ed. Springer-Verlag, 2012.
- [71] W. Kohn and L. J. Sham. “Self-Consistent Equations Including Exchange and Correlation Effects”. In: *Physical Review* 140 (1965), A1133.

- [72] Z. Konôpková, S. McWilliams, N. Gómez-Pérez, and A. F. Goncharov. “Direct measurement of thermal conductivity in solid iron at planetary core conditions”. In: *Nature* 534 (2016), pp. 99–101.
- [73] W. D. Kraeft, D. Kremp, W. Ebeling, and G. Röpke. *Quantum Statistics of Charged Particle Systems*. Berlin: Plenum Press, 1986.
- [74] D. Kraus, J. Vorberger, A. Pak, N. J. Hartley, L. B. Fletcher, S. Frydrych, E. Galtier, E. J. Gamboa, et al. “Formation of diamonds in laser-compressed hydrocarbons at planetary interior conditions”. In: *Nature Astronomy* 1 (2017), pp. 606–611.
- [75] D. Kremp, M. Schlanges, and W. D. Kraeft. *Quantum Statistics of Nonideal Plasmas*. Berlin Heidelberg: Springer-Verlag, 2005.
- [76] S. Kumar, A. J. Poser, M. Schöttler, U. Kleinschmidt, W. Dietrich, J. Wicht, M. French, and R. Redmer. “Ionization and transport in partially ionized multicomponent plasmas: Application to atmospheres of hot Jupiters”. In: *Physical Review E* 103 (2021), p. 063203.
- [77] K. Kurosaki and M. Ikoma. “Acceleration of Cooling of Ice Giants by Condensation in Early Atmospheres”. In: *Astronomical J.* 163 (2017), p. 260.
- [78] U. Le Verrier. “Sur la planète qui produit les anomalies observées dans les mouvement d’Uranus - Détermination de sa masse, de son orbite et de sa position actuelle”. In: *Comptes rendus hebdomadaires des séances de l’Académie des sciences XXIII* (1846), p. 428. URL: <https://gallica.bnf.fr/ark:/12148/bpt6k2980r/f432.item>.
- [79] J. Leconte and G. Chabrier. “A new vision of giant planet interiors: Impact of double diffusive convection”. In: *Astronomy & Astrophysics* 540 (2012), A20.
- [80] J. Leconte and G. Chabrier. “Layered convection as the origin of Saturn’s luminosity anomaly”. In: *Nature Geoscience* 6 (2013), p. 347.
- [81] J. Leconte, F. Selsis, F. Hersant, and T. Guillot. “Condensation-inhibited convection in hydrogen-rich atmospheres”. In: *Astronomy & Astrophysics* 598 (2017), A98.
- [82] L. Li, X. Jiang, R. A. West, P. J. Gierasch, S. Perez-Hoyos, A. Sanchez-Lavega, L. N. Fletcher, J. J. Fortney, et al. “Less absorbed solar energy and more internal heat for Jupiter”. In: *Nature Communications* 9 (2018), p. 3709.

- [83] G. F. Lindal, J. R. Lyons, D. N. Sweetnam, V. R. Eshleman, D. P. Hinson, and G. L. Tyler. “The atmosphere of Uranus: Results of radio occultation measurements with Voyager 2”. In: *Journal of Geophysical Research: Space Physics* 92 (1987), pp. 14987–15001.
- [84] G. F. Lindal. “The atmosphere of Neptune: An analysis of radio occultation data acquired with Voyager 2”. In: *The Astronomical Journal* 103 (1992), pp. 967–982.
- [85] E. F. Linder, C. Mordassini, P. Mollière, G.-D. Marleau, M. Malik, S. P. Quanz, and M. R. Meyer. “Evolution models of cold and low-mass planets: cooling curves, magnitudes, and detectability”. In: *Astronomy & Astrophysics* 623 (2019), A85.
- [86] R. F. Loewenstein, D. A. Harper, and H. Moseley. “The effective temperature of Neptune”. In: *The Astrophysical Journal* 218 (1977), pp. L145–L146.
- [87] L. Lorenz. “Bestimmung der Wärmegrade in absolutem Maasse”. In: *Annalen der Physik* 223 (1872), pp. 429–452.
- [88] M. Lozovsky, R. Helled, E. D. Rosenberg, and P. Bodenheimer. “Jupiter’s Formation and Its Primordial Internal Structure”. In: *The Astrophysical Journal* 836 (2017), p. 227.
- [89] B. Luzum, N. Capitaine, A. Fienga, W. Folkner, T. Fukushima, J. Hilton, C. Hohenkerk, G. Krasinsky, et al. “The IAU 2009 system of astronomical constants: the report of the IAU working group on numerical standards for Fundamental Astronomy”. In: *Celestial Mechanics and Dynamical Astronomy* 110 (2011), p. 293.
- [90] S. P. Lyon and J. D. Johnson. *SESAME: The Los Alamos National Laboratory equation of state database (LA-UR-92-3407)*. Los Alamos National Laboratory. Los Alamos, 1992.
- [91] C. R. Mankovich and J. J. Fortney. “Evidence for a Dichotomy in the Interior Structures of Jupiter and Saturn from Helium Phase Separation”. In: *The Astrophysical Journal* 889 (2020), p. 51.
- [92] S. Markham and D. Stevenson. “Constraining the Effect of Convective Inhibition on the Thermal Evolution of Uranus and Neptune”. In: *The Planetary Science Journal* 2 (2021), p. 146.

- [93] M. S. Marley, P. Gómez, and M. Podolak. “Monte Carlo interior models for Uranus and Neptune”. In: *Journal of Geophysical Research* 100 (1995), pp. 23349–23353.
- [94] S. Mazevet, A. Licari, G. Chabrier, and A. Y. Petkhin. “Ab initio based equation of state of dense water for planetary and exoplanetary modeling”. In: *Astronomy & Astrophysics* 621 (2019), A128.
- [95] J. M. McMahan, M. A. Morales, C. Pierleoni, and D. M. Ceperley. “The properties of hydrogen and helium under extreme conditions”. In: *Review of Modern Physics* 84 (2012), pp. 1607–1653.
- [96] N. D. Mermin. “Thermal Properties of the Inhomogeneous Electron Gas”. In: *Physical Review* 137 (1965), A1441–A1443.
- [97] B. Militzer and W. B. Hubbard. “Comparison of Jupiter interior models derived from first-principles simulations”. In: *Astrophysics and Space Science* 322 (2009), pp. 129–133.
- [98] N. Miller, J. J. Fortney, and B. Jackson. “Inflating and deflating hot Jupiters: coupled tidal and thermal evolution of known transiting planets”. In: *The Astrophysical Journal* 702 (2009), pp. 1413–1427.
- [99] S. Millholland. “Tidally Induced Radius Inflation of Sub-Neptunes”. In: *The Astrophysical Journal* 886 (2019), p. 72.
- [100] C. Mordasini, G.-D. Marleau, and P. Mollière. “Characterization of exoplanets from their formation. III. The statistics of planetary luminosities”. In: *Astronomy & Astrophysics* 608 (2017), A72.
- [101] N. Nettelmann, J. J. Fortney, K. Moore, and C. Mankovich. “An exploration of double diffusive convection in Jupiter as a result of hydrogen-helium phase separation”. In: *Monthly Notices of the Royal Astronomical Society* 447 (2015), pp. 3422–3441.
- [102] N. Nettelmann, K. Wang, J. J. Fortney, S. Hamel, S. Yellamilli, M. Bethkenhagen, and R. Redmer. “Uranus evolution models with simple thermal boundary layers”. In: *Icarus* 275 (2016), pp. 107–116.
- [103] N. Nettelmann. “Matter under extreme conditions: modelling giant planets”. PhD thesis. Universität Rostock, 2009. URL: <http://purl.uni-rostock.de/rosdok/id00000925>.

- [104] N. Nettelmann, A. Becker, B. Holst, and R. Redmer. “Jupiter models with improved ab initio hydrogen equation of state (H-REOS.2)”. In: *The Astrophysical Journal* 750 (2012), p. 52.
- [105] N. Nettelmann, R. Helled, J. J. Fortney, and R. Redmer. “New indication for a dichotomy in the interior structure of Uranus and Neptune from the application of modified shape and rotation data”. In: *Planetary and Space Science* 77 (2013), pp. 143–151.
- [106] N. Nettelmann, B. Holst, A. Kietzmann, M. French, R. Redmer, and D. Blaschke. “Ab initio equation of state data for hydrogen, helium, and water and the internal structure of Jupiter”. In: *The Astrophysical Journal* 683 (2008), pp. 1217–1228.
- [107] W. Nolting. *Grundkurs Theoretische Physik 4 - Spezielle Relativitätstheorie, Thermodynamik*. 8. Auflage. Berlin Heidelberg: Springer-Verlag, 2012.
- [108] J. Oertel Herbert, ed. *Prandtl - Führer durch die Strömungslehre - Grundlagen und Phänomene*. 14th ed. Springer Vieweg, 2017.
- [109] J. C. Pearl and B. J. Conrath. “The albedo, effective temperature, and energy balance of Neptune, as determined from Voyager data”. In: *JGR Space Science* 96 (1991), p. 18921.
- [110] J. C. Pearl, B. J. Conrath, R. A. Hanel, J. A. Pirraglia, and A. Coustenis. “The albedo, effective temperature, and energy balance of Uranus, as determined from Voyager IRIS data”. In: *Icarus* 84 (1990), pp. 12–28.
- [111] P. J. E. Peebles. “The Structure and Composition of Jupiter and Saturn”. In: *The Astrophysical Journal* 140 (1964), p. 328.
- [112] M. Podolak, W. B. Hubbard, and D. J. Stevenson. “Models of Uranus’ interior and magnetic field”. In: *Uranus*. Ed. by J. T. Bergstralh, E. D. Miner, and M. Shapley Matthews. Tucson: The University of Arizona Press, 1991, pp. 29–61.
- [113] M. Podolak, A. Weizman, and M. Marley. “Comparative models of Uranus and Neptune”. In: *Planetary and Space Science* 43 (1995), pp. 1517–1522.
- [114] M. Podolak, R. Helled, and G. Schubert. “Effect of non-adiabatic thermal profiles on the inferred compositions of Uranus and Neptune”. In: *Monthly Notices of the Royal Astronomical Society* 487 (2019), pp. 2653–2664.
- [115] A. J. Poser, N. Nettelmann, and R. Redmer. “The Effect of Clouds as an Additional Opacity Source on the Inferred Metallicity of Giant Exoplanets”. In: *Atmosphere* 10 (2019), p. 664.

- [116] M. Preising and R. Redmer. “Metallization of dense fluid helium from ab initio simulations”. In: *Physical Review B* 102 (2020), p. 224107.
- [117] A. Prša, P. Harmanec, G. Torres, E. Mamajek, M. Asplund, N. Capitaine, J. Christensen-Dalsgaard, É. Depagne, et al. “Nominal Values for Selected Solar and Planetary Quantities: IAU 2015 Resolution B3”. In: *The Astronomical Journal* 152 (2016), p. 41.
- [118] R. Püstow, N. Nettelmann, W. Lorenzen, and R. Redmer. “Saturn layered structure and homogeneous evolution models with different EOSs”. In: *Icarus* 267 (2016), pp. 323–333.
- [119] A. Ravasio, M. Bethkenhagen, J.-A. Hernandez, A. Benuzzi-Mounaix, F. Datchi, M. French, M. Guarguaglini, F. Lefevre, et al. “Metallization of Shock-Compressed Liquid Ammonia”. In: *Physical Review Letters* 126 (2021), p. 025003.
- [120] R. Redmer, T. R. Mattsson, N. Nettelmann, and M. French. “The phase diagram of water and the magnetic fields of Uranus and Neptune”. In: *Icarus* 211 (2011), pp. 798–803.
- [121] F. H. Ree. *Equation of state of water UCRL-52190*. Lawrence Livermore Laboratory. Livermore, 1976.
- [122] C. Reinhardt, A. Chau, J. Stadel, and R. Helled. “Bifurcation in the history of Uranus and Neptune: the role of giant impacts”. In: *Monthly Notices of the Royal Astronomical Society* 492 (2020), pp. 5336–5353.
- [123] A. M. Rymer, K. D. Runyon, B. Clyde, J. I. Núñez, R. Nikoukar, K. M. Soderlund, K. Sayanagi, M. Hofstadter, et al. “Neptune Odyssey: A Flagship Concept for the Exploration of the Neptune–Triton System”. In: *The Planetary Science Journal* 2 (2021).
- [124] I.-J. Sackmann, A. I. Boothroyd, and K. E. Kraemer. “Our Sun. III. Present and Future”. In: *The Astrophysical Journal* 418 (1993), pp. 457–468.
- [125] P. Sarkis, C. Mordasini, T. Henning, G.-D. Marleau, and P. Mollière. “Evidence of three mechanisms explaining the radius anomaly of hot Jupiters”. In: *Astronomy & Astrophysics* 645 (2020), A79.
- [126] D. Saumon, G. Chabrier, and H. M. van Horn. “An equation of state for low-mass stars and giant planets”. In: *The Astrophysical Journal Supplement Series* 99 (1995), p. 713.
- [127] L. Scheibe, N. Nettelmann, and R. Redmer. “Thermal evolution of Uranus and Neptune I. Adiabatic models”. In: *Astronomy & Astrophysics* 632 (2019), A70.

- [128] L. Scheibe, N. Nettelmann, and R. Redmer. “Thermal evolution of Uranus and Neptune. II. Deep thermal boundary layer”. In: *Astronomy & Astrophysics* 650 (2021), A200.
- [129] H. Schilling. *Wärme und Energie*. 1. Auflage. Leipzig: VEB Fachbuchverlag Leipzig, 1984.
- [130] K. M. Soderlund, M. H. Heimpel, E. M. King, and J. M. Aurnou. “Turbulent models of ice giant internal dynamics: Dynamos, heat transfer, and zonal flows”. In: *Icarus* 224 (2013), pp. 97–113.
- [131] S. Stanley and J. Bloxham. “Convective-region geometry as the cause of Uranus’ and Neptune’s unusual magnetic fields”. In: *Nature* 428 (2004), pp. 151–153.
- [132] S. Stanley and J. Bloxham. “Numerical dynamo models of Uranus’ and Neptune’s magnetic fields”. In: *Icarus* 184 (2006), pp. 556–572.
- [133] D. J. Stevenson. “The Uranus-Neptune Dichotomy: the Role of Giant Impacts”. In: *Lunar and Planetary Science XVII* (1986), pp. 1011–1012. URL: https://ui.adsabs.harvard.edu/link_gateway/1986LPI...17.1011S/ADS_PDF.
- [134] D. J. Stevenson and E. E. Salpeter. “The dynamics and helium distribution in hydrogen-helium fluid planets”. In: *Astrophysical Journal Supplement Series* 35 (1977), pp. 239–261.
- [135] J. S. Turner. *Buoyancy Effects in Fluids*. Cambridge Monographs on Mechanics. Cambridge: Cambridge University Press, 1973.
- [136] J. S. Turner. “Double-Diffusive Phenomena”. In: *Annual Review of Fluid Mechanics* 6 (1974), pp. 37–54.
- [137] A. Vazan, R. Helled, A. Kovetz, and M. Podolak. “Convection and mixing in giant planet evolution”. In: *The Astrophysical Journal* 803 (2015), p. 32.
- [138] A. Vazan and R. Helled. “Explaining the low luminosity of Uranus: a self-consistent thermal and structural evolution”. In: *Astronomy & Astrophysics* 633 (2020), A50.
- [139] W. Wagner and A. Pruß. “The IAPWS Formulation 1995 for the Thermodynamic Properties of Ordinary Water Substance for General and Scientific Use”. In: *Journal of Physical and Chemical Reference Data* 31 (2002), p. 387.

- [140] H. R. Wakeford and P. A. Dalba. “The exoplanet perspective on future ice giant exploration”. In: *Philosophical Transactions of the Royal Society A: Mathematical, Physical and Engineering Sciences* 378 (2020), p. 20200054.
- [141] C. Wang, X.-T. He, and P. Zhang. “Thermophysical properties of hydrogen-helium mixtures: Re-examination of the mixing rules via quantum molecular dynamics simulations”. In: *Physical Review E* 88 (2013), p. 033106.
- [142] J. W. Warwick, D. R. Evans, G. R. Peltzer, R. G. Peltzer, J. H. Romig, C. B. Sawyer, A. C. Riddle, A. E. Schweitzer, et al. “Voyager Planetary Radio Astronomy at Neptune”. In: *Science* 246 (1989), pp. 1498–1501.
- [143] J. W. Warwick, D. R. Evans, J. H. Romig, C. B. Sawyer, M. D. Desch, M. L. Kaiser, J. K. Alexander, T. D. Carr, et al. “Voyager 2 Radio Observations of Uranus”. In: *Science* 233 (1986), pp. 102–106.
- [144] G. Wiedemann and R. Franz. “Ueber die Wärme-Leitungsfähigkeit der Metalle”. In: *Annalen der Physik* 165 (1853), pp. 497–531.
- [145] D. R. Williams. *NASA Planetary Fact Sheets*. Last Accessed 2021-09-13. National Aeronautics and Space Administration U.S.A. URL: <https://nssdc.gsfc.nasa.gov/planetary/planetfact.html>.

Danksagung

Mein tief empfundener Dank gilt meiner Betreuerin und Mentorin Nadine Nettelmann. Ohne ihr außerordentliches Maß an Geduld, Hilfsbereitschaft und Anleitung, sowie ihr Vertrauen und Zuversicht in mich, wäre die vorliegende Dissertation wohl unmöglich gewesen. Gleiches ist auch von meinem Doktorvater Ronald Redmer zu sagen, in dessen Arbeitsgruppe ich diese Dissertation anfertigen durfte und von dem ich stets mit Rat und Hilfe rechnen konnte. Meine besondere Dankbarkeit gilt darüber hinaus meiner Kollegin und guten Freundin Anna Julia Poser, die nicht nur Gelegenheit zu ergiebiger wissenschaftlicher Diskussion über diese Arbeit und unsere gemeinsame Leidenschaft für die Planetenphysik bot, sondern auch unschätzbare emotionale und mentale Unterstützung bereit gestellt hat.

Die gesamte AG „Statistische Physik“ verdient Anerkennung für das erfreuliche kollegiale Klima und unzählige Mensa-, Kaffee- und Kuchenrunden mit Diskussion über Physik, Wissenschaft, und die Welt als Ganzes, wodurch der Arbeitsalltag stets bereichert wurde. Insbesondere hervorgehoben sei das unermüdliche Adminteam, das bei Problemen stets zur Stelle war. Die DFG-Forschungsgruppe 2440, „Matter Under Planetary Interior Conditions“ ermöglichte nicht nur finanziell die Bearbeitung dieses Projektes, sondern machte im Rahmen der regelmäßigen Treffen auch einen regen wissenschaftlichen Austausch möglich, wofür ich mich bei allen Mitgliedern bedanke. Ebenso bedanke ich mich beim ISSI-Team „Ice Giants: Formation, Internal Structure, and the Link to Exoplanets“, im Zuge dessen ein erfrischender und angenehmer Austausch über die Erforschung des Uranus und des Neptun möglich war.

Mein Dank gilt darüber hinaus meinen Eltern, Großeltern, meiner Schwester und der erweiterten Familie. Stets wurde mir ein Gefühl von Unterstützung und Geborgenheit gegeben, insbesondere in den schweren ersten Wochen der Corona-Pandemie. Nicht unerwähnt bleiben dürfen natürlich auch die Schauvorlesung der Physik, meine Rollenspielgruppe „Die Verrückten“, die Improgruppe „Spontane Emission“ und eine unzählige Reihe an Individuen, die mir in den Jahren meiner Promotion so manche erfreuliche Stunde geschenkt und meine Tage erhellt haben.

All diesen Leuten sage ich: Danke!

Curriculum Vitae

- Name: Ludwig Scheibe
- Geboren am 04. 08. 1992 in Magdeburg

Akademische Ausbildung

- Seit 11/2016 Promotionsstudium im Fachbereich Physik, Universität Rostock.
- 10/2014 – 09/2016 Master of Science im Fachbereich Physik, Universität Rostock. *Abschlussnote 1,3*, Thema der Abschlussarbeit: „Numerische Modellierung des inneren Aufbaus und der thermischen Entwicklung von Neptun“
- 10/2011 – 09/2014 Bachelor of Science im Fachbereich Physik, Universität Rostock. *Abschlussnote 2,0*, Thema der Abschlussarbeit: „Berechnung einer Zustandsgleichung für Ammoniak im chemischen Bild“
- 10/2011 Abitur am Werner-von-Siemens Gymnasium, Magdeburg. *Abschlussnote 1,1*

Berufserfahrung

- 11/2016 – 09/2021 Wissenschaftlicher Mitarbeiter, Universität Rostock, AG Statistische Physik, numerische Modelle der thermischen, Entwicklung Neptun-artiger Planeten
- 02/2015 – 09/2015 Wissenschaftliche Hilfskraft Universität Rostock, AG Statistische Physik, Weiterentwicklung einer Zustandsgleichung für Ammoniak im chemischen Bild

Lehre (Universität Rostock)

SS 2017, SS 2018, Betreuung im *Grundpraktikum I*, Institut für Physik
SS 2019, SS 2020

WS 2018/19, WS 2019/20, Betreuung im *Grundpraktikum II*, Institut für Physik
WS 2020/21

SS 2020 Co-Betreuung einer Bachelorarbeit
zum Thema „Aufbau von M-Sternen mit MESA“

Liste der Veröffentlichungen

- M. Bethkenhagen, E. R. Meyer, S. Hamel, N. Nettelmann, M. French, L. Scheibe, C. Ticknor, L. A. Collins, J. D. Kress, J. J. Fortney, R. Redmer. „Planetary Ices and the Linear Mixing Approximation“. In: *The Astrophysical Journal*, 848 (2017), p. 67
- L. Scheibe, N. Nettelmann, R. Redmer. „Thermal evolution of Uranus and Neptune I. Adiabatic models“. In: *Astronomy & Astrophysics*, 632 (2019), p. A70
- L. Scheibe, N. Nettelmann, R. Redmer. „Thermal evolution of Uranus and Neptune II. Deep thermal boundary layer“. In: *Astronomy & Astrophysics*, 650 (2021), p. A200

Liste der Konferenzbeiträge

Fachvorträge

- 08/2018: L. Scheibe, N. Nettelmann, R. Redmer. „Modeling planets with Henyey method“. FOR2440 Workshop on low-mass planets, Universität Rostock
- 09/2018: L. Scheibe, N. Nettelmann, R. Redmer. „Towards a new tool for modeling non-adiabatic giant planets“. European Planetary Science Congress (EPSC) 2018, Berlin
- 02/2019: L. Scheibe, N. Nettelmann, R. Redmer. „Adiabatic evolution calculations for Uranus and Neptune and the influence of solar irradiation“. Team-Meeting „Ice Giants: Formation, Internal Structure, and the Link to Exoplanets“, ISSI Bern
- 09/2019: L. Scheibe, N. Nettelmann, R. Redmer. „Thermal evolution of Uranus and Neptune“. Northern Astrophysical Colloquium, Universität Rostock
- 10/2019: L. Scheibe, N. Nettelmann, R. Redmer. „Thermal evolution of Uranus and Neptune“. 8th Workshop on High Pressure, Planetary and Plasma Physics (HP4), Dresden
- 03/2020: „Ice giant evolution with a conducting thermal boundary layer“. Team-Meeting „Ice Giants: Formation, Internal Structure, and the Link to Exoplanets“, ISSI Bern

Posterpräsentationen

- 02/2017: L. Scheibe, N. Nettelmann, R. Redmer. „Thermal evolution models for Uranus and Neptune under the assumption of a thermal boundary layer“. Matter in Extreme Conditions: from MATERIAL science to Plasmas for Laboratory Astrophysics (MECMATPLA) Winter School, Montgenevre
- 10/2017: L. Scheibe, N. Nettelmann, R. Redmer. „Towards a new tool for modeling giant planets“. 6th Workshop on High Pressure, Planetary and Plasma Physics (HP4), MPS Göttingen

- 10/2018: L. Scheibe, N. Nettelmann, R. Redmer. „Towards a new tool for modelling non-adiabatic giant planets“. 7th Workshop on High Pressure, Planetary and Plasma Physics (HP4), DLR Berlin
- 03/2019: L. Scheibe, N. Nettelmann, R. Redmer. „Thermal evolution of adiabatic Uranus and Neptune and beyond“. Planet Formation and Evolution, Rostock
- 04/2019: L. Scheibe, N. Nettelmann, R. Redmer. „Uranus and Neptune thermal evolution“. European Geosciences Union (EGU) General Assembly 2019, Wien
- 09/2019: L. Scheibe, N. Nettelmann, R. Redmer. „Thermal evolution of Uranus and Neptune“. European Planetary Science Congress (EPSC) 2019, Genf
- 01/2020: L. Scheibe, N. Nettelmann, R. Redmer. „Thermal evolution of Uranus and Neptune“. Ice Giants Systems Workshop, Royal Society London
- 09/2020: L. Scheibe, N. Nettelmann, R. Redmer. „Influence of a thermal boundary layer on the thermal evolution of Uranus and Neptune“. Virtuelles Poster, European Planetary Science Congress (EPSC) 2020 (Online)
- 10/2020: L. Scheibe, N. Nettelmann, R. Redmer. „Influence of a thermal boundary layer on the thermal evolution of Uranus and Neptune“. Virtuelles Poster, WE-Heraeus-Seminar „Matter under Extreme Conditions (Online)
- 12/2020: L. Scheibe, N. Nettelmann, R. Redmer. „Influence of a thermal boundary layer on the thermal evolution of Uranus and Neptune“. Virtuelles Poster, American Geophysical Union (AGU) Fall Meeting 2020 (Online)

Selbstständigkeitserklärung

Ich versichere hiermit an Eides statt, dass ich die vorliegende Arbeit selbstständig angefertigt und ohne fremde Hilfe verfasst habe, keine außer den von mir angegebenen Hilfsmitteln und Quellen dazu verwendet habe und die den benutzten Werken inhaltlich und wörtlich entnommenen Stellen als solche kenntlich gemacht habe.

Rostock, 04. 10. 2021